ROYAUME DU MAROC
Université Mohammed V - RABAT -
جامعة محمد الخامس – الرباط –
Faculté des sciences
كلية العلوم
CENTRE D'ETUDES DOCTORALES - SCIENCES ET TECHNOLOGIES

N° d'ordre : 3703

THESE

En vue de l'obtention du: ***DOCTORAT***

Structure de Recherche : *Laboratoire* de Matière Condensée et Sciences interdisciplinaires: Unité de Recherche Labellisée CNSR

Discipline : *Physique*

Spécialité : *Physique des particules*

Présentée et soutenue le 29/10/2022 par :

Mohamed ZAAZOUA

Search for invisible decays of the Higgs Boson, with interpretation for dark matter, using the ATLAS Detector at the LHC

Devant le Jury

Abdeslam HOUMMADA	PES, Université HASSAN II, Académie Hassan II des Sciences et Techniques, Casablanca	Président
Hamid EZ-ZAHRAOUY	PES, Université Mohammed V, Faculté des Sciences, Rabat	Rapporteur/ Examinateur
Mohamed CHABAB	PES, Université Cadi Ayyad, Faculté des Sciences Semlalia, Marrakech	Rapporteur/ Examinateur
Morad EL BAZ	PES, Université Mohammed V, Faculté des Sciences, Rabat	Rapporteur/ Examinateur
Abdesslam ARHRIB	PES, Université Abdelmalek Essaadi, Faculté des Sciences et Techniques, Tanger	Examinateur
Farida FASSI	PH, Université Mohammed V, Faculté des Sciences, Rabat	Directeur

Année Universitaire : 2022/2023

Dedication

" This endeavor is in honor of my mother, father, siblings, and the rest of my loved ones"

Mohamed Zaazoua

Acknowledgement

My profound gratitude to **Mr. Hamid EZ-ZAHRAOUY**, professor at the Faculty of sciences in Rabat and director of the research structure "Laboratory of Condensed Matter and Interdisciplinary Sciences: Unit of Research Labeled CNSRT". His door's office was always open whenever I asked for help. I admire the positive mood and the inspiration he gives to the team.

I would like to thank my primary supervisor, **Mme. Farida FASSI**, professor at the Faculty of sciences in Rabat, for believing in me and understanding my curiosity. She inspired me to be a winner, showed me the value of patience and captured my imagination through our conversations about physics and its impact on the future. For many helpful discussions, motivation and for reading my thesis, I will be forever grateful. Without her great assistance, inspiration, and encouragement, this thesis would not have been feasible.

My sincere gratitude also goes to **Mr. Abdeslam HOUMMADA**, professor at the Hassan II Academy of Sciences and Technology, who accepted the presidency of the jury. I appreciate his comments and discussions about this thesis work.

It has been a privilege to work under the guidance of my thesis defense committee members.

I thank **Mr. Hamid EZ-ZAHRAOUY**, professor at the Faculty of Sciences Rabat, who accepted to be reporter and examiner of this thesis, for his guidance, support and comments.

I thank **Mr. Mohamed CHABAB**, professor at the Faculty of Sciences Semlalia, who is reporter and examiner of this dissertation work, for his assistance, time and effort regarding the defence process.

I thank **Mr. Morad EL BAZ**, professor at the Faculty of Sciences Rabat, for accepting to be reporter and examiner of my thesis. I sincerely appreciate his encouragement, comments and discussions.

I thank **Mr. Abdesslam ARHRIB**, professor at the Faculty of Science and Technology Tangier, for examining this thesis work. I appreciate the information and advice he has shared.

I would like to thank **Dr. Ketevi Adikle ASSAMAGAN**, who advised me on the analyses projects I worked on throughout my research. I am fortunate to have his valuable technical and moral support.

Résumé

Cette thèse présente une recherche de bosons de Higgs à désintégration invisible à l'aide des données de collision proton-proton de 13 TeV enregistrées par le détecteur ATLAS au Grand collisionneur des hadrons. La recherche est effectuée à l'aide de l'ensemble de données collectées pendant la phase Run2, ce qui correspond à une luminosité totale de 139 fb^{-1}. L'analyse visée est le boson de Higgs invisible produit par la fusion de bosons vectoriels, où la sensitivité est améliorée. L'estimation du bruit de fond, la sélection des événements et la fixation des limites ainsi que l'interprétation des résultats sont décrits en détail. Aucune déviation par rapport au modèle standard n'a été observée. Interprété en termes de recherche de matière noire à l'aide des modèles de bosons de Higgs, ce résultat peut être utilisé pour fixer des limites à la section efficace WIMP-nucléon diffusion. Cette thèse présente également une combinaison des études axées sur la recherche de bosons de Higgs invisibles, où le boson est produit, soit en mode VBF, soit en association avec une paire de quarks top. Ces résultats sont également interprétés dans le contexte de modèles où le boson de Higgs de 125 GeV agit comme un portail vers la matière noire. Enfin, une discussion de l'interprétation de la section efficace des nucléons et de WIMPs dans le cas du vecteur Higgs portail de la matière noire, est mis en œuvre, où la largeur de désintégration du Higgs invisible mesurée au LHC est utilisée.

Mots clés: matière noir, WIMPs, Higgs, désintégration invisible, Higgs-portal, Modèle Standard

Abstract

In this dissertation, a search for invisibly decaying Higgs bosons using 13 TeV proton-proton collision data recorded by the ATLAS detector at the LHC is presented. The search is performed using datasets collected during the Run2 phase of operation, corresponding to an integrated luminosity of 139 fb^{-1}. The targeted analysis is the invisible Higgs boson produced via the Vector Boson Fusion, where the sensitivity is enhanced by allowing for new phase spaces. Background estimation, consideration of pileup tagging in the forward region, events selection categorisation, and limit setting as well as the interpretation are described in details. No deviations from the Standard Model have been observed, and the final result is reported in the form of a 95% Confidence Level upper limit on the branching fraction. The overall result of the measurement using full Run2 data yields an observed limit of 0.145. When interpreted in terms of Dark Matter searches using Higgs portal models, this result can be used to set upper limits on spin-independent WIMP-nucleon cross section. A combination of studies focusing on searches for invisible Higgs bosons, where the SM Higgs is produced, either, through VBF mode or in association with a pair of top quarks is presented in this thesis as well. Last but not least, a review and discussion of the Higgs portal-vector Dark Matter interpretation of the spin- independent Dark Matter nucleon elastic scattering cross section is implemented, where the invisible Higgs decay width measured at the LHC is used.

Key words: Dark Matter, WIMPs, Higgs, invisible decay, Higgs-portal, Standard Model

Résumé détaillé

Le modèle standard (SM) de la physique des particules offre un formalisme mathématique capable d'encapsuler notre compréhension actuelle de ce que sont les éléments constitutifs de la matière et la manière dont ils interagissent. Les deux expériences du Grand collisionneur de hadrons (LHC), CMS et ATLAS, ont déclaré en juillet 2012 avoir observé le boson de Higgs, le seul composant restant du modèle standard qui n'avait pas encore été découvert. Cette découverte a culminé le succès du programme de physique du collisionneur de hadrons le plus grand et le plus énergétique du monde. Malgré tous ses succès, le modèle standard ne donne pas une vue entièrement détaillée et complète de la connaissance actuelle des interactions fondamentales. Plusieurs aspects théoriques et expérimentaux restent non résolus. Le modèle standard ne fournit pas d'explication à l'existence de la matière noire, indiquée par diverses mesures de l'astrophysique, à travers ses effets de gravité. Les extensions théoriques du modèle standard appelées théories au-delà du modèle standard introduisent de nouvelles interactions, symétries ou dimensions supplémentaires pour répondre à ces questions.

Depuis que son existence a été déduite en 1933, la nature de la matière noire est restée un grand mystère qui est considéré par beaucoup comme la prochaine énigme à résoudre dans la physique des particules aux collisionneurs après la découverte du boson de Higgs. Le secteur noir (matière noire et énergie noire) représente 95% de l'énergie dans l'univers. alors que la composante visible n'y contribue qu'à hauteur de 5 %. Le LHC peut contribuer à la recherche de matière noire de diverses manières grâce aux différentes expériences qu'il abrite. La matière noire peut se manifester sous forme d'énergie manquante dans l'état final, provenant soit des désintégrations invisibles des bosons de Higgs, soit de nouvelles particules, comme le postulent plusieurs théories au-delà du modèle standard. La production directe de matière noire peut être réalisée dans des scénarios de portail de Higgs, où les bosons de Higgs agissent comme médiateurs entre la matière noire et les particules du modèle standard, ce qui implique que les candidats de matière noire, c'est-à-dire les particules massives à faible interaction (WIMP), pourraient se coupler au boson de Higgs. Dans ce contexte, l'état final apparaît comme "invisible" pour le détecteur ATLAS, et la présence d'objets visibles, tels que des jets, est nécessaire pour étiqueter un événement de matière noire. La désintégration du boson de Higgs en matière noire ou en particules qui n'appartiennent pas au modèle standard est produite dans le mode de fusion du boson vectoriel (VBF), qui est le canal de production le plus sensible, car il permet un rejet efficace du bruit de fond. Par conséquent, la recherche de désintégrations invisibles du boson de Higgs est une méthode puissante pour sonder la matière noire au LHC.

Cette thèse présente une recherche de bosons de Higgs à désintégration invisible à l'aide des données de collision proton-proton à l'énergie du centre de masse de 13 TeV collectées par le détecteur ATLAS au Grand collisionneur des hadrons (LHC). La recherche est effectuée à l'aide de l'ensemble complet de données collectées pendant la phase d'exploitation Run2, ce qui correspond à une luminosité totale de 139 fb^{-1}.

L'analyse visée est le boson de Higgs invisible produit par la fusion des vecteurs bosons

(VBF), où la sensitivité est améliorée en permettant de nouveaux espaces de phase auparavant inaccessibles. L'estimation du bruit de fond, prendre en considération du marquage des pileup dans la région frontal du détecteur, la catégorisation de la sélection des événements et la fixation des limites ainsi que l'interprétation des résultats sont décrits en détail. Aucune déviation par rapport au modèle standard n'a été observée et le résultat final est rapporté sous la forme d'une limite supérieure sur le rapport de branchement $\mathcal{B}_{H\to\text{inv}}$ à 95% du niveau de confiance (CL). Le résultat de la mesure utilisant les données complètes du run–2 donne un $\mathcal{B}_{H\to\text{inv}}$ observé (attendu) de 0.145 (0.103), ce qui constitue la meilleure limite jamais établie pour la recherche d'un boson de Higgs invisible dans une seule voie de désintégration. Interprété en termes de recherche de matière noire à l'aide des modèles de bosons de Higgs, ce résultat peut être utilisé pour assigner des limites supérieures à la section efficace de diffusion WIMP-nucléon. En outre, les résultats sont interprétés comme recherche de désintégrations invisibles d'un boson de Higgs scalaire supplémentaire avec des masses de 50 GeV à 2 TeV.

Cette thèse présente également une combinaison des études axées sur la recherche de bosons de Higgs invisibles, où le boson est produit, soit en mode VBF, soit en association avec une paire de quarks top se désintégrant en zéro ou deux leptons dans les états finaux. Aucune déviation du Modèle Standard n'a été observée, et le résultat final est rapporté sous la forme d'une limite supérieure observée (attendue) de 0.11 (0.11$\pm$0.04) observée (attendue) sur le $\mathcal{B}_{H\to\text{inv}}$ à 95% CL. Ces résultats sont également interprétés dans le contexte de modèles où le boson de Higgs de 125 GeV agit comme un portail vers la matière noire, et des limites sont fixées sur la section efficace de la diffusion WIMP-nucléon.

Enfin, une discussion de l'interprétation de la section efficace de la diffusion élastique des nucléons et de WIMPs dans le cas du vecteur Higgs portail de la matière noire, sont mis en œuvre, où la largeur de l'invisible désintégration du Higgs $\Gamma_{H\to inv}$ mesurée au LHC est utilisée. La théorie des champs effective (FET) et les modèles complets ultraviolets (UV) sont présentés. Les interprétations du LHC ne montrent que les scénarios de scalaire et Majorana pour le Higgs portail, une proposition visant à inclure l'interprétation pour le vecteur dans le cadre théorique de l'EFT et des modèles UV complets est présentée. En outre, du point de vue des études qui en découlent, une extension des interprétations de la matière noire du LHC au régime sub-GeV est suggérée.

List of publications

My work has been included in the following publications:

- Mohamed Zaazoua, Loan Truong, Kétévi Adikle Assamagan, Farida Fassi. "Higgs portal vector dark matter interpretation: review of Effective Field Theory approach and ultraviolet complete models", LHEP.2022.270, 2022 [1].
- ATLAS Collaboration. "Search for invisible Higgs boson decays in events with vector-boson fusion signatures using 139 fb^{-1} of proton-proton data recorded by the ATLAS experiment", JHEP 08 (2022) 104, (2022). [2].
- ATLAS Collaboration. "Combination of searches for invisible Higgs boson decays with the ATLAS experiment: H(125) $\rightarrow$ invisible combination" ATLAS-CONF-2020-052, 2020 [3].
- ATLAS Collaboration. "Search for invisible Higgs boson decays with vector boson fusion signatures with the ATLAS detector using an integrated luminosity of 139 fb^{-1}", ATLAS-CONF-2020-008, 2020 [4].
- ATLAS Collaboration. "High Luminosity LHC (HL-LHC) projection studies for VBF+MET analysis: Prospects for H $\rightarrow$ Invisible with VBF+MET". PUB-EXOT-2021-18, in progress.
- ATLAS Collaboration. " run–1 and run–2 invisible Higgs combination: CDM HComb H$\rightarrow$inv comb. 2015-2018 " ANA-HIGG-2021-05, in progress.
- Mohamed Zaazoua, Farida Fassi, Kétévi Adikle Assamagan, Loan Truong. "Search for Invisible Higgs Bosons Produced via Vector Boson Fusion at the LHC Using ATLAS Detector", BSM-2021 Conference proceeding, 2021.
- Mohamed Zaazoua, Farida Fassi, Kétévi Adikle Assamagan, Diallo Boye "Search for invisible Higgs bosons produced via vector boson fusion at the LHC using the ATLAS detector" ACP-2021 Conference proceeding, 2022.

• Scopus author ID: 57211848338 • INSPIRE ID:INSPIRE-00699611
• ORCID:0000-0002-4105-2988

List of contributions

During my thesis, I was involved in the following tasks:

- ATLAS Qualification Task: muon-jet overlap removal and missing transverse energy performance:
  - Update the METPerfAnalysis code to study the muon-jet overlap removal and performance of track selections.
- Evaluation of the gluon-gluon Fusion (ggF) uncertainties for the VBF+MET analysis:
  - Implementation of the code to evaluate the ggF uncertainties using the Steward-Tackmann (ST) method.
- Evaluation of the V+jets theoretical uncertainties for the VBF+MET analysis:
  - Update code for the evaluation of the resummation 'qsf', and CKKW matching scales.
- Interpretation of the result as searches for dark matter for the VBF+MET analysis and for the invisible Higgs combination analysis, separately:
  - Update the code with implementation of results from new direct detection experiments and new result from VBF+MET analysis.
- Interpretation of the result as searches for dark matter for the VBF+MET analysis and for the invisible Higgs combination, separately:
  - Re-introduction of the vector Higgs portal model using the EFT approach.
  - Implementation of code for the Higgs portal interpretation using three UV complete models.
- Implementation of the VBF+MET inputs for the invisible Higgs combination analysis.
- Evaluation of the experimental uncertainties for the "Prospects for H $\rightarrow$ Invisible with VBF+MET".
  - Implementation of code for uncertainties evaluation following the High-Lumi-LHC Systematics strategy.
- Limit setting on the invisible Higgs branching fraction for the "Prospects for H $\rightarrow$ Invisible with VBF+MET" using HistFitter.
- Contribution to Snowmass 2022 and LOI for ASFAP strategy "Higgs portal vector dark matter interpretation: review of Effective Field Theory approach and ultraviolet complete models."

List of abbreviations

Symbol	Full name
SM	Standard Model
BSM	Beyond Standard Model
DM	Dark Matter
MET	Missing Transverse Momentum
VBF	Vector Boson Fusion
ggF	gluon-gluon Fusion
QCD	Quantum Chromodynamics
VDM	Vector Dark Matter
EFT	Effective Field Theory
vev	vacuum expectation values
UV	Ultraviolet
WIMPS	Weakly Interactive Massive Particles
ECAL	Electromagnetic Calorimeter
HadCAL	Hadronic Calorimeters
ATLAS	A Toroidal LHC Apparatus
CMS	Compact Muon Spectrometer
LHC	Large Hadron Collider
LINAC	Linear Accelerator
SSB	Spontaneous Symmetry Breaking
MS	Muon Spectrometer
ID	Inner Detector

List of Tables

List of Figures

Contents

Introduction

The Standard Model (SM) of particle physics offers a mathematical formalism able to encapsulate our current understanding of what the building blocks of matter are and how they interact. The two Large Hadron Collider (LHC) experiments, CMS and ATLAS, declared in July 2012 that they have observed the Higgs Boson, the only remaining component of the Standard Model that had yet to be discovered. This discovery culminated the success of the physics program of the largest and most energetic collider of hadrons in the world. Despite all its successes, The Standard Model does not give a fully detailed view of the current knowledge of fundamental interactions, and several theoretical and experimental aspects remain unresolved. It does not provide an explanation to the existence of the dark matter, indicated by various measurements of astrophysics, through its gravity effects. Theoretical extensions of the Standard Model named Beyond-Standard-Model theories are introducing new interactions, symmetries, or extra-dimensions to address this SM questions. Since its existence was inferred in 1933, the nature of dark matter remained a great mystery that is considered by many as the next puzzle to solve within particle physics at colliders after the Higgs boson discovery. The dark sector (dark matter and dark energy) accounts for 95 % of the energy in the universe. whereas the visible component contributes only with 5%. The LHC can contribute to the search for dark matter in various ways using different experiments it houses. Dark matter can manifest itself as missing energy in the final state, stemming from either the invisible decays of the Higgs bosons or of new particles, as postulated in several BSM theories. The direct production of dark matter may be realised in Higgs-portal scenarios, where the Higgs bosons act as mediators between dark matter and the Standard Model particles, implying that dark matter candidates i.e., the weakly interacting massive particles (WIMPs) could couple to the Higgs boson. In this context, the final state appears as 'invisible' for the ATLAS detector, and the presence of visible objects, such as jets, is necessary to tag a dark matter event. The decay of the Higgs boson to dark matter or non-SM particles is produced in the vector boson fusion (VBF) mode, which is the most sensitive production channel since it allows for effective rejection of background. Therefore, searching for invisible decays of the Higgs boson is a powerful method to probe for dark matter at the LHC.

The analysis presented in this dissertation reports on the big improvements in comparison to the analysis published in [5], including optimisation of the control region definitions, improvement of the background estimation, reduction of statistical uncertainties, better handling of the systematic uncertainties as well as optimisation of the event selection categorisation to enhance the signal sensitivity. Furthermore, a special focus of this thesis is the combination of searches for Higgs decaying into invisible, where the SM Higgs boson is produced in the VBF mode or in association with a pair of top quarks with zero or two leptons in the final states. This manuscript also presents the interpretation of the obtained search results as constraints on Higgs-portal dark matter models, i.e, limits on the invisible Higgs branching fraction are transformed into an upper limit on the spin-independent WIMP-Nucleon scattering cross section, as well as search for heavy Higgs scalar bosons, acting as a mediator between SM and dark sectors.

The chapters of this dissertation are organised as follows: After an overall introduction, the first chapter describes the fundamental constituents of matter and their interactions. Gauge theories and symmetries are introduced, and the generalisation to the electroweak theory and the Higgs mechanism is discussed. This chapter also motivates the search for an invisibly decaying Higgs boson, and characteristics of the production and decay modes are highlighted. Chapter 2 describes the LHC at CERN, with focus on the ATLAS experiment, with which the data used in this thesis was collected. The detector and its sub-systems are described, with the focus on detailing their characteristics and usage with respect to the search for invisible Higgs boson decays. Chapter 3 presents the event reconstruction and objects used in the invisible Higgs analyses. The performance of the missing transverse energy as well as the muon-jet overlap removal study is discussed in chapter 4. The search for invisibly decaying Higgs bosons produced in the VBF mode using proton-proton collision data of the LHC run–2, collected by ATLAS during the periods from 2015 to 2018 is detailed in chapter 5. In order to improve the sensitivity to invisible Higgs boson decays, a statistical combination is conducted and presented in chapter 6. The limits are also reinterpreted under non-SM production assumptions using Higgs-portal models, with focus on the Higgs portal-vector DM interpretation, where the review of the Effective Field Theory approach and ultraviolet complete models is discussed in chapter 7.

Chapter 1:

Theoretical framework

The Standard Model (SM) of particle physics is the name associated in the 1970s to the theory that describes the building blocks of the matter in the universe and the interactions governing them, based on Quantum Field Theory (QFT). As far as we know, all interactions acting around us can be whittled down to just four fundamental forces: the electromagnetic force acts between charged particles, the weak nuclear force is responsible for particle decay, the strong nuclear force binding quarks together inside the proton, and gravity that preserves planets in their orbits around the sun. Only three are described by the SM, the gravity still an open question for the QFT.

1.1 Standard Model Particles

The SM names seventeen particles (30 particles in total if antiparticles are taken into account) that can be divided according to their spin quantum number into two categories:

Particles with half-integer spin are named fermions, following Fermi-Dirac statistics, and can be arranged in two classes: leptons and quarks, each one consists of six particles paired in three generations. The first generation is made of the lightest and most stable particles, whereas the second and third generations contain the heavier and less stable ones. Leptons can be electrically charged like the electron (e) and its heavier cousins muons (μ) and taus (τ); for each one it exits an electrically neutral associate called neutrino: an electron neutrino (ν_e) for the electron, a muon neutrino (ν_μ) and a tau neutrino (ν_τ). The up (u) and down (d) quarks of the first generations can combine to form hadrons with effectively infinite life spans, like neutron and protons. While charm (c) and strange (s) of generation II quarks always form unstable hadrons. The bottom (b) and top (t) quarks of generation III are the heaviest among all SM particles. The top quark and its antiparticle are so heavy and short-lived that they don't exist long enough to do anything. They are known only from their decay products. Properties of these fermions particles, like charge, mass and spin, are summarized in Figure 1.

Particles with integer spin are called bosons, they follow Bose-Einstein statistics. Also known as force-carrier particles or mediators, because they control the interaction of physical forces, such as electromagnetism. The basic gauge bosons that mediate the fundamental forces of nature and the Higgs boson fall into this category. Bosons are listed in Figure 1 with their corresponding charge, spin and mass. They have all been experimentally observed in different detectors, with the manifestation of the same behaviour as anticipated by the SM theory. The photon (γ) mediates the electromagnetic interactions, W^-, W^+ and Z bosons mediate the weak nuclear force, and gluons (g) mediate the interactions of the strong nuclear force. The Higgs boson (H) is a 0 spin particle with no electric charge. Its existence is essential to give mass for the Z and W bosons through Brout-Englert-Higgs mechanism. This is of great importance for the consistency of the SM theory.

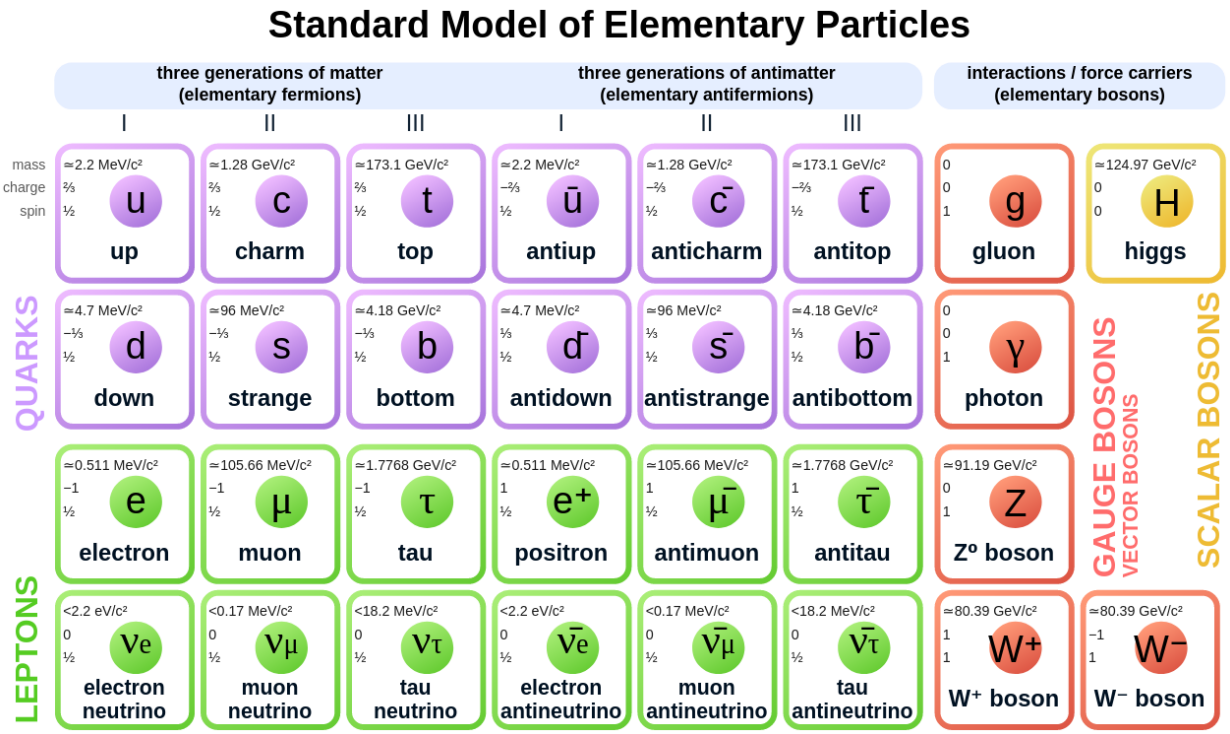

Figure 1: Figure with all Standard Model particles. Fermions arranged in two categories, quarks in violet, leptons in green and bosons in yellow and orange with their corresponding mass, charge and spin (Figure from Wikimedia Commons).

The SM predicts the existence of antiparticles, which are related to ordinary particles by having exactly the same properties but opposite electric charge. Thus, positron ($\overline{e}$), anti-muon ($\overline{\mu}$) and anti-tau ($\overline{\tau}$) are the antiparticles for e, μ and τ. Quarks also have their own antiparticles: $\overline{u}$, $\overline{d}$, $\overline{c}$, $\overline{s}$, $\overline{b}$ and $\overline{t}$. Each particle can interact with its antiparticle, causing the annihilation of both of them and emergence of new particles. By accelerating and colliding electrons with positrons, The Large Electron-Positron (LEP) collider make use of this to create different types of particles.

With the CMS (Compact Muon Solenoid) and the ATLAS (A Toroidal LHC ApparatuS) collaborations announcement of the Higgs boson discovery on July 4, 2012, the existence of the last missing component of the Standard Model has been established.

1.2 Standard Model Forces

The Standard Model is an unprecedented precise and consistent theory that describes nature's interactions through the electromagnetic, weak and strong forces.

1.2.1 Electromagnetic interactions

Quantum Electrodynamics (QED), which is based on QFT, describes electromagnetic interaction between charged particles through the exchange of quantum fields known as photons. The QED Lagrangian is invariant under the U(1) transformation. The Dirac Lagranian of a given fermion with mass m and a fermion field ψ is [6]:

$$\mathcal{L}_{Dirac} = \bar{\psi}(i\gamma^{\mu}\partial_{\mu} - m)\psi \tag{1}$$

$\bar{\psi}$ is the Dirac adjoint of ψ, and γ^{μ} is the Dirac matrices. This $\mathcal{L}_{Dirac}$ is not only Lorentz invariant but also invariant under global transformation of $U(1)$ group:

$$\psi \rightarrow \exp{(ie\Lambda)}\psi$$
$$\bar{\psi} \rightarrow \exp{(-ie\Lambda)}\bar{\psi}$$

Note that upgrading U(1) to be a local transformation($\Lambda \rightarrow \Lambda(x)$), the Lagrangian becomes not invariant:

$$\mathcal{L}_{Dirac} \rightarrow \mathcal{L}_{Dirac} - e\bar{\psi}\gamma^{\mu}\partial_{\mu}\Lambda(x)\psi$$

The simplest way to change the action to make it locally $U(1)$ invariant is to introduce a four vector field that transforms under this gauge symmetry in a manner to cancel the term destroying the invariance under local $U(1)$ transformation, and replace the partial derivative by a gauge covariant derivative:

$$\partial_{\mu} \rightarrow D_{\mu} = \partial_{\mu} - ieA_{\mu} \tag{2}$$

Where e is the electric charge and A_{μ} is the new four-vector field that transforms under $U(1)$ gauge transformation as follows:

$$A_{\mu} \rightarrow A\mu - \partial_{\mu}\Lambda(x) \tag{3}$$

The covariant derivative transforms in the following manner to establish the invariance for Dirac Lagrangian under local U(1) transformation:

$$D_\mu\psi \to \exp(ie\Lambda(x))D_\mu\psi$$
$$\bar{\psi}\gamma^\mu D_\mu\psi \to \bar{\psi}\gamma^\mu D_\mu\psi$$

With the above modifications, the Lagrangian still missing the kinematic energy term of the electromagnetic field. The needed term is derived from Maxwell equations of electromagnetism and has the following form [7]:

$$\mathcal{L}_{Maxwell} = -\frac{1}{4\mu}F^{\mu\nu}F_{\mu\nu} - A_\mu J^\mu \tag{4}$$

where $F^{\mu\nu} = \partial_\mu A_\nu - \partial_\nu A_\mu$, is the field strength tensor, called also Faraday tensor or Maxwell bivector. Its components are the magnetic and electric fields. J_μ is the current four density vector. The resulting Lagrangian density, is invariant under the local $U(1)$ transformation:

$$\mathcal{L}_{QED} = i\bar{\psi}\gamma^\mu D_\mu\psi - m\bar{\psi}\psi - \frac{1}{4\mu}F_{\mu\nu}F^{\mu\nu} \tag{5}$$

The absence of the term with the mediator's mass is noteworthy. The QED Lagrangian is invariant only if the mass of the mediator of the EM force is null, which is consistent with the mass of the photon.

1.3 Strong Nuclear Force

The Quantum chromodynamics (QCD) is the theory that describes the strong interaction in the SM, The QCD Lagrangian is invariant under the $SU(3)$ transformation. Similarly to what was done above, considering Dirac Lagrangian for a fermion field of six quarks of mass m_f, that can be written as follows [6]:

$$\mathcal{L}_{Dirac} = \sum_f \bar{\psi}^f(i\gamma^\mu\partial_\mu - m^f)\psi^f \tag{6}$$

The goal is to try to enlarge the gauge group of free-space electrodynamics, from $U(1)$ to $SU(3)$. The generators of the fundamental representation of $SU(3)$ satisfy the following lie algebra [8]:

$$[\tau^a, \tau^b] = if^{abc}\tau^c \tag{7}$$

$\tau^a = \frac{\lambda^a}{2}$, where λ^a are the Gell-Mann matrices in the case of SU(N), and f^{abc} is called the structure constant of the group and completely antisymmetric with respect to the exchange of any two indices. The isospine multiplet in the fundamental representation can be defined as follows:

$$\psi_i \to \Omega^i_j\psi_j$$
$$\bar{\psi}_i \to \bar{\psi}_j{\Omega^j_i}^{-1}$$

Where Ω is a unitary matrix:

$$\Omega_i^j = [\exp(-i\theta^a \tau_a)]_i^j$$

If this isospin multiplet is taken to be multiplet of Dirac spinor, the Lagrangian can be written as in Equation 6. The main difference between this Lagrangian and the Dirac one used for QED, is the global SU(3) symmetry, with the Dirac field transforming in the fundamental representation. The symmetry is then upgraded to a local symmetry using covariant derivatives and gauge fields, defined as follows [8]:

$$\begin{aligned} D_\mu^{ij} &= (\delta^{ij}\partial_\mu - ig\tau_a^{ij}A_\mu^a)\psi_j \\ \Omega_i^j(x) &= [\exp(-i\theta^a(x)\tau_a)]_i^j \end{aligned} \tag{8}$$

where:

$$(\tau_a^{ij}A_\mu^a) = A_\mu(x) \to A_\mu(x)' = -\frac{i}{g}[\partial_\mu\Omega(x)]\Omega^{-1}(x) + \Omega(x)A_\mu(x)\Omega^{-1}(x) \tag{9}$$

$$A_\mu^a \to A_\mu^{a'} = 2Tr[-\tau^a\frac{i}{g}[\partial_\mu\Omega(x)]\Omega^{-1}(x)] + 2Tr[\tau^a\Omega(x)\tau_b(x)\Omega^{-1}(x)]A_\mu^b \tag{10}$$

The covariant derivative transforms covariantly as follows:

$$D_\mu\psi \to (D_\mu\psi)' = \partial_\mu\psi' - igA_\mu'\psi' = \Omega(x)D_\mu\psi$$

The Commutation of the covariant derivatives are used to get the field strength tensor:

$$[D_\mu, D_\nu]^{ij}\psi_j = D_{k\mu}^i D_\nu^{kj}\psi_j - D_{k\nu}^i D_\mu^{kj}\psi_j = -igG_{\mu\nu}^{ij}\psi_j \tag{11}$$

where:

$$\begin{aligned} G_{\mu\nu}^{ij} &= \tau_a^{ij}G_{\mu\nu}^a \\ G_{\mu\nu}^a &= \partial_\mu A_\mu^a + gf^{abc}A_\mu^b A_\nu^c \\ G_{\mu\nu}^{ij} &\to \Omega_k^i(x)G_{\mu\nu}^{kl}\Omega^{-1}{}_l^j(x) \end{aligned}$$

The gauge field dynamical Lagrangian density is deduced by squaring the field strength tensor. It's known as the Yang-Mills Lagrangian and is written as follows:

$$\mathcal{L}_{Yang-Mills} = -\frac{1}{2}Tr[G_{\mu\nu}G^{\mu\nu}] = -\frac{1}{4}G_{\mu\nu}^a G_a^{\mu\nu} \tag{12}$$

This Lagrangian is gauge invariant :

$$Tr[G_{\mu\nu}G^{\mu\nu}] \to Tr[\Omega(x)G_{\mu\nu}\Omega^{-1}(x)\Omega G^{\mu\nu}\Omega^{-1}(x)] = Tr[G_{\mu\nu}G^{\mu\nu}]$$

By adding this Yang-Mills Lagrangian to the locally SU(3) invariant Dirac Lagrangian, the QCD Lagrangian density can be deduced:

$$\mathcal{L}_{QCD} = \bar{\psi}(i\gamma^\mu D_\mu^{ij} - m\delta^{ij})\psi_j - \frac{1}{4}G_{\mu\nu}^a G_a^{\mu\nu} \tag{13}$$

1.4 EWK interaction

At low energy, the weak and electromagnetic forces appear to be very different and well distinguishable from each other. But at high energies, they merge into a single and more fundamental force dubbed 'electroweak' force (EWK). This unified force is also known as the Glashow-Salam-Weinberg (GSW) theory [9]. The EW Lagrangian is invariant under the following transformation:

$$G \equiv SU(2)_L \otimes U(1)_Y \tag{14}$$

$SU(2)$ is the simplest group with doublet, and the $U(1)$ group is needed to count for the electromagnetic interaction. In Equation 14, L stand for the left hand fields and Y is the hypercharge.
The following fields notation for the first family of quarks are considered:

$$\psi_1(x) = \begin{pmatrix} u \\ d \end{pmatrix}_L, \qquad \psi_2(x) = u_R, \qquad \psi_3(x) = d_R \tag{15}$$

Or also for leptons:

$$\psi_1(x) = \begin{pmatrix} \nu_e \\ e^- \end{pmatrix}_L, \qquad \psi_2(x) = \nu_{eR}, \qquad \psi_3(x) = e_R^- \tag{16}$$

The Dirac Lagrangian without the mass term can be written in the following way [6]:

$$\mathcal{L}_{Dirac} = \sum_f i\bar{\psi}_j(x)\gamma^\mu \partial_\mu \psi_j(x) \tag{17}$$

This Lagrangian is invariant under the global G transformations:

$$\begin{aligned} \psi_1(x) \to \psi_1^{'} &= e^{(iy_1\beta)} U_L \psi_1(x) \\ \psi_2(x) \to \psi_2^{'} &= e^{iy_2\beta} \psi_2(x) \\ \psi_3(x) \to \psi_3^{'} &= e^{iy_3\beta} \psi_3(x) \end{aligned} \tag{18}$$

Where U_L is $SU(2)_L$ transformation, acts only on the doublet ψ_1, and parameters y_i are called hypercharges:

$$U_L \equiv e^{i\frac{\sigma_i}{2}\alpha^i} \qquad (i = 1, 2, 3) \tag{19}$$

The mass term is not included to avoid its mixing with left and right-handed fields which spoil the symmetry.
G needs to be updated to a local transformation with $\alpha^i = \alpha^i(x)$ and $\beta = \beta(x)$. But requiring the Lagrangian to stay invariant under this transformation, which leads to change the fermions derivatives by the covariance and introduce four different gauge bosons [10]:

$$\begin{aligned} D_\mu\psi_1(x) &\equiv [\partial_\mu - ig\tilde{W}_\mu(x) - ig^{'} y_1 B_\mu(x)]\psi_1(x), \\ D_\mu\psi_2(x) &\equiv [\partial_\mu - ig^{'} y_2 B_\mu(x)]\psi_2(x), \\ D_\mu\psi_3(x) &\equiv [\partial_\mu - ig^{'} y_3 B_\mu(x)]\psi_3(x), \end{aligned} \tag{20}$$

Where $\tilde{W}_\mu(x)$ is an $SU(2)_L$ matrix field:

$$\tilde{W}_\mu(x) \equiv \frac{\sigma_i}{2} W^i_\mu(x) \tag{21}$$

Gauge fields are fixed in a way that $D_\mu\psi$ transform in the same way as ψ_j:

$$B_\mu(x) \to B'_\mu(x) \equiv B_\mu(x) + \frac{1}{g'}\partial_\mu\beta(x), \tag{22}$$

$$\tilde{W}_\mu \to \tilde{W}'_\mu \equiv U_L(x)\tilde{W}_\mu U_L^\dagger(x) - \frac{i}{g}\partial_\mu U_L(x) U_L^\dagger(x), \tag{23}$$

Where $U_L(x)$ is defined as follows [10]:

$$U_L(x) \equiv e^{i\frac{\sigma_i}{2}\alpha^i(x)}$$

The B_μ transformation and the one obtained in QED for the photon are identical, but W^i_μ transform in a way similar to the QCD gluon fields. The free Lagrangian is now invariant under the local $U_L(x) \equiv \exp\left(i\frac{\sigma_i}{2}\alpha^i(x)\right)$ transformation:

$$\mathcal{L} = \sum_f i\bar{\psi}_j(x)\gamma^\mu D_\mu \psi_j(x) \tag{24}$$

Identical to the definition of the field strength for the QED, one can define:

$$B_{\mu\nu} \equiv \partial_\mu B_\nu - \partial_\nu B_\mu \tag{25}$$

Analogically to the definition of the field strength of the gluon fields in QCD, one can define:

$$\tilde{W}_{\mu\nu} \equiv \frac{i}{g}[(\partial_\mu - ig\tilde{W}_\mu), (\partial_\nu - ig\tilde{W}_\nu)] = \partial_\mu\tilde{W}_\nu - \partial_\nu\tilde{W}_\mu - ig[W_\mu, W_\nu], \tag{26}$$

While:

$$\tilde{W}_{\mu\nu} = \frac{\sigma_i}{2} W^i_{\mu\nu}, \qquad W^i_{\mu\nu} = \partial_\mu W^i_\nu - \partial_\nu W^i_\mu + g\epsilon^{ijk} W^j_\mu S^k_\nu \tag{27}$$

Under G transformation, the two field strengths vary as follows:

$$B_{\mu\nu} \to B_{\mu\nu}, \qquad \tilde{W}_{\mu\nu} \to U_L \tilde{W}_{\mu\nu} U_L^\dagger \tag{28}$$

The first one is invariant, while the second transforms covariantly. Therefore, the gauge fields dynamical Lagrangian density is:

$$\mathcal{L}_{dyn} = -\frac{1}{4}B_{\mu\nu}B^{\mu\nu} - \frac{1}{2}Tr[\tilde{W}_{\mu\nu}\tilde{W}^{\mu\nu}] = -\frac{1}{4}B_{\mu\nu}B^{\mu\nu} - \frac{1}{4}W^i_{\mu\nu}W_i^{\mu\nu} \tag{29}$$

The final Lagrangian for the electroweak interactions can be written as follows:

$$\mathcal{L}_{EWK} = \sum_f i\bar{\psi}_j(x)\gamma^\mu D_\mu\psi_j(x) - \frac{1}{4}B_{\mu\nu}B^{\mu\nu} - \frac{1}{4}W^i_{\mu\nu}W_i^{\mu\nu} \tag{30}$$

The mass terms for the gauge bosons and fermions are not added into the Lagrangian, to not spoil the symmetry. Only massless fields are considered here.

1.5 Brout-Englert-Higgs mechanism

So far, only massless fields were used in the unified EW theory. Bosons are supposed to be massless in order to preserve the local gauge symmetry. However, although this is acceptable for the photon field, experimental observations show the Z and $W^{\pm}$ bosons peaks of mass far from zero, which indicates that they are very heavy particles. The masses of charged leptons and quarks are measured with extreme precision. To generate masses for these particles, the gauge symmetry needs to be broken in some way. However, in order to preserve renormalizability, a fully symmetric Lagrangian is needed. The answer could be found in the fact that a non-symmetric result can be obtained from an invariant Lagrangian. This is accomplished using the Spontaneous Symmetry Breaking (SSB) mechanism, also called Higgs Mechanism [11].

Consider a Lagrangian that is invariant under a group G of transformations and has a degenerate set of minimal energy states that transform as members of a specified multiplet under G. If one of those states is arbitrarily chosen as the system's ground state, It is said that the symmetry is spontaneously broken. The vacuum is the ground state in Quantum Field Theory.

As a result, the SSB mechanism will appear when there is a symmetric Lagrangian but a non-symmetric vacuum. Although the Lagrangian remains invariant under the transformation in general with SSB, the vacuum ground state is dependent on the gauge used. One can consider ϕ an SU(2) complex doublet:

$$\phi = \begin{pmatrix} \phi^{+} \\ \phi^{0} \end{pmatrix}, \tag{31}$$

The plus signs in ϕ^{+} stands for positive electric charge and ϕ^{0} is an electric neutral field. The corresponding Lagrangian is [12]:

$$\mathcal{L} = (D_{\mu}\phi)^{\dagger}(D_{\mu}\phi) - V(\phi), \tag{32}$$

Where D_{μ} is the covariant derivative of the EW theory, and $V(\phi)$ is a potential with the form:

$$D_{\mu}\phi = [\partial^{\mu} - ig\tilde{W}^{\mu} - ig^{'}y_{\phi}B^{\mu}]\phi, \qquad V(\phi) = \mu^{2}\phi^{\dagger}\phi + \lambda(\phi^{\dagger}\phi)^{2}, \tag{33}$$

$V(\phi)$ is called the Higgs potential and ϕ the Higgs field. λ is chosen to be > 0 , because the potential need to be bounded from below in order to have a ground state. Two more possible cases for the quadratic piece: if $\mu^{2} > 0$, the potential minimum is at $\phi = 0$ as shown in the left of Figure 2, and the case describes a massive scalar particle with mass μ and quartic coupling λ. If $\mu^{2} < 0$ (right of Figure 2), the minimum of the potential is reached for the following values of the field:

$$|\phi_{0}| = \sqrt{\frac{-\mu^{2}}{2\lambda}} \equiv \frac{v}{\sqrt{2}} > 0, \qquad V(\phi_{0}) = -\frac{h}{4}v^{4} \tag{34}$$

There are infinite set of degenerate states with minimum energy and satisfying the equation above as in Figure 3. When a particular ground state is chosen, the $SU(2)_{L} \otimes U(1)_{Y}$ symmetry

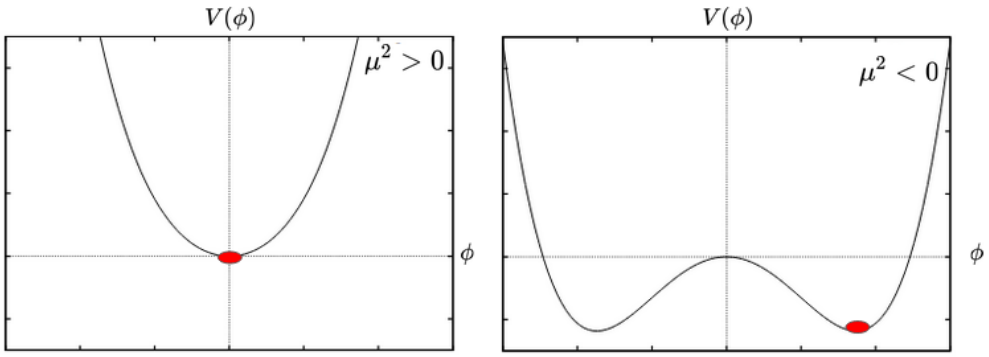

Figure 2: 2D view of the shape of the scalar potential for $\lambda > 0$ and $\mu^2 > 0$ (left) corresponding to a minimum at $\phi = 0$ and $\mu^2 < 0$ (right) with a minimum at non-null values of the fields.

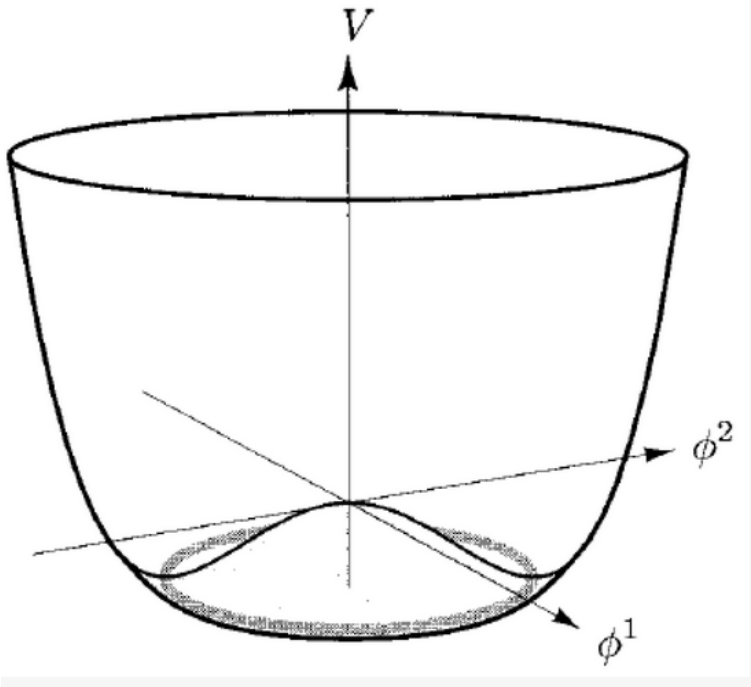

Figure 3: 3D view of the shape of the scalar potential for $\lambda > 0$ and $\mu^2 < 0$ where there is a continuous set of degenerate vacua, corresponding to different phases [13].

gets spontaneously broken to the electromagnetic subgroup $U(1)$. The scalar doublet can be parametrized as follows [10]:

$$\phi(x) = \exp\left(i\frac{\sigma_i}{2}\theta^i(x)\right)\frac{1}{\sqrt{2}}\begin{pmatrix}0\\ v+H(x)\end{pmatrix}, \tag{35}$$

For simplicity, the minimum is chosen to be :

$$\phi = \frac{1}{\sqrt{2}}\begin{pmatrix}0\\ v+H\end{pmatrix} \tag{36}$$

The Higgs field's Lagrangian becomes:

$$\mathcal{L}_{Higgs} = (D_\mu\phi)^\dagger(D_\mu\phi) - \frac{1}{2}(-2\mu^2)H^2 - \lambda v H^3 - \frac{1}{4}\lambda H^4, \tag{37}$$

Where the second term contains the mass of the Higgs field:

$$m_H = \sqrt{-2\mu^2} = v\sqrt{2\lambda} \tag{38}$$

Substituting the first term by the EW covariant derivative expression, the mass of the electroweak bosons have the following form:

$$\begin{aligned}|(-ig\frac{\sigma_i}{2}W_\mu^i - ig'\frac{Y}{2}B_\mu)\phi|^2 &= \frac{1}{8}\left|\begin{pmatrix}gW_\mu^3 + g'B_\mu & g(W_\mu^1 - iW_\mu^2)\\ g(W_\mu^1 + iW_\mu^2) & -gW_\mu^3 + g'B_\mu\end{pmatrix}\begin{pmatrix}0\\ v\end{pmatrix}\right|^2 \\ &= (\frac{vg}{2})^2 W_\mu^+ W_\mu^- + \frac{1}{2}(\frac{v\sqrt{g^2+g'^2}}{2})^2 Z_\mu^2 + \frac{1}{2}.0.A_\mu^2\end{aligned} \tag{39}$$

The masses of the bosons can be extracted as follows:

$$m_{W^+} = m_{W^-} = \frac{vg}{2}, \tag{40}$$

$$m_Z = \frac{v\sqrt{g^2+g'^2}}{2}, \tag{41}$$

$$m_\gamma = 0. \tag{42}$$

Fermions as well appears in many experimental observations to have masses and sometimes as heavy objects, i.e.: the top quark. Their masses are produced via the Yukawa coupling between the fermions fields and the Higgs field [10]:

$$\mathcal{L}_{Yukawa} = \sum_f -g_Y^f(\bar{\psi}_L^f\phi\psi_R^f + \bar{\psi}_R^f\phi\psi_L^f) \tag{43}$$

where the Yukawa coupling constant for the fermion f is noted g_Y^f, and is defined as:

$$m_f = \frac{vg_Y^f}{\sqrt{2}}. \tag{44}$$

1.6 Higgs discovery

The ATLAS and CMS joint announcement of 2012 [14, 15], was a turning point in the life of the Standard Model. The two experiments conducted further studies to confirm if the finding is exactly the Higgs boson and if it interacts with both bosons and fermions. The Higgs boson has been observed decaying to tau particles, bottom quarks, and being produced together with top quarks. In other words, it has been proven beyond a doubt that the Higgs boson interacts with fermions.

Figure 4 compares Higgs interaction strength to the mass of Standard Model particles shows that the interaction strength depends on the particle mass, confirming one of the main predictions of the BEH mechanism.

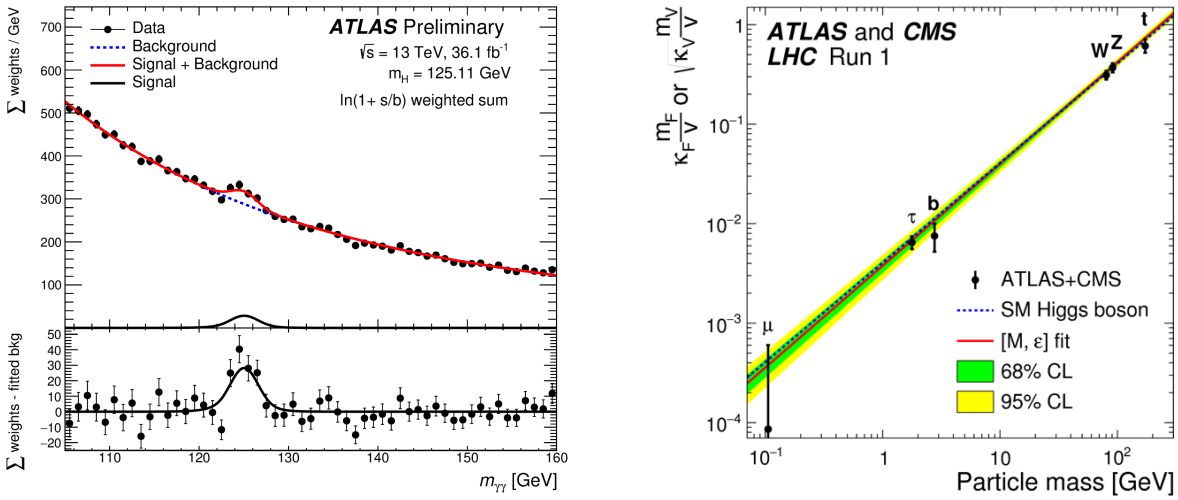

Figure 4: The left panel shows the reconstructed mass (125 GeV) from Higgs candidate events in two-photon decays(H$\rightarrow \gamma\gamma$). The right panel shows the Higgs interaction strength function of the mass of Standard Model particles: the heavier the particle, the stronger its interaction with the Higgs field. This is one of the principal predictions of the BEH mechanism in the Standard Model [16].

1.7 Standard Model limitations

The discovery of the Higgs bosons at the LHC in 2012 confirmed the existence of the final missing piece of the Standard Model. In spite of being largely successful in the prediction of the particles properties and their interactions, the SM can't answer many open questions and phenomena that escape our understanding and still unaddressed:

The SM predicts that the three neutrinos should have no mass like the photon. This is in contradiction with the fact that neutrinos can oscillate as they move through space, and this is possible only if neutrinos have some mass, even a quite small one.

Particles and their anti-particles are thought to be generated in equal parts, assuming that the Big Bang produced exactly equal amounts of matter and anti-matter when the universe

formed. However, following the annihilation of particles by their anti-particles, an excess of matter remained to form the universe as we know. The fact that the laws of nature have favored the existence of matter is still a mystery. Many different experiments are looking into this matter-antimatter asymmetry to find out what tipped the scales.

The force of gravity appears to have no effect on the processes of subatomic particles, and the Standard Model is not intended to explain gravity. This fourth force, like the other SM forces, is thought to have a force carrier boson known as graviton. The Standard Model does not predict its existence and provides no information about its properties.

According to Hubble Space Telescope (HST) observations of very distant supernovae, the universe was actually expanding more slowly than it is now a long time ago. The expansion of the universe has not slowed due to gravity, as everyone assumed; rather, it has accelerated. We know how much dark energy exists because we understand how it affects the expansion of the universe. It turns out that dark energy accounts for roughly 68% of the universe. The standard model can't explain its existence or why the universe is expanding.

Studying the gravitational pull of the visible matter of galaxies, physicists discovered that the galaxies were spinning much faster than expected, threatening to tear themselves apart. So the existence of unknown matter, dubbed Dark Matter (DM), is proposed and estimated to account for about 27% of the content of the universe. In spite of the fact that it constitutes the vast majority of matter in the universe, the Standard Model can't explain its existence or predict any of its properties. Many attempts to define the nature of the dark matter or to prove the existence of its particles candidates are proposed in beyond standard model frameworks.

1.8 Dark Matter

The Standard Model particles seem to fulfill all our need about understanding the matter around us and building all kind of objects in our daily life. However, staring at large scale structures as clusters of galaxies shows that a hidden large amount of matter is spreading through space and it cannot be made of any of the usual Standard Model particles. The difference in total matter density $\Omega_m \simeq 0.2 \sim 0.3$ (in units of the critical density $\rho_c = 3H_0^2/8\pi G$, where H_0 is the Hubble parameter), and the $\Omega_b \simeq 0.05$ baryon density needed for the observed light elements abundances to agree with those predicted by Big Bang nucleosynthesis [17], provided evidence that much of this matter is nonbaryonic. We discuss in the following section the evidence for dark matter existence.

1.8.1 Rotation curve

Observations of the motion of galaxies, mainly their rotation curves and the circular velocity as function of the distance from the center of the galaxy, provide direct evidence to the existence of dark matter. In a typical spiral galaxy, i.e: the Milky Way, we can refer the mass enclosed within the radius of the galaxy by the evaluation of the rotational velocity $v_c(r)$ of stars and gas as a function of the radius r of the galaxy. According to Kepler relation:

$$v_c^2(r) = \frac{GM_{obs}}{r}, \tag{45}$$

One can expect that the rotation curve should decline as the radius approaches the distance from center to the galaxy's outskirts, showed in gray dashed line in Figure 5. Instead, one notices that the curve of velocity remains constant as the radius keep getting larger as shown in Figure 5, implying that the galaxy contains much larger amount of matter than the mass contribution from stars and gas. The total mass of the galaxy within radius r can be estimated

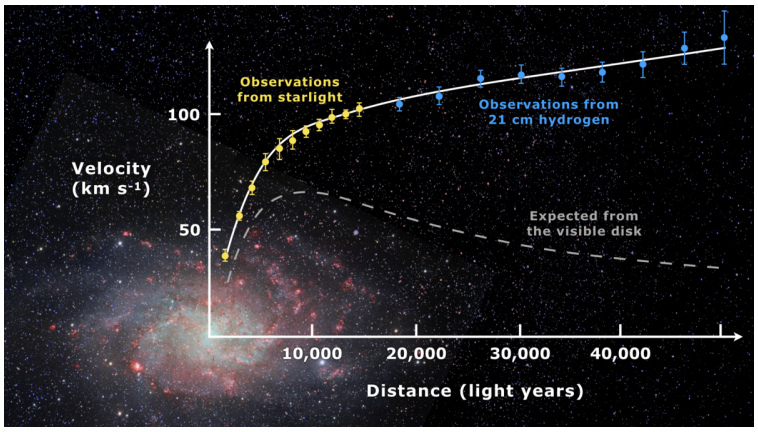

Figure 5: Rotation curve of the Messier 33 spiral galaxy showed in yellow and blue points with error bars, and the corresponding prediction from distribution of the visible matter showed with gray line [18].

using:

$$M(r_0) = 4\pi \int_0^{r_0} r^2 \rho(r) dr, \tag{46}$$

The measurement in Figure 5, illustrates that the velocity $v(r)$ becomes approximately constant. Then the mass and distribution needs to fulfill the following criteria to match the profile of the rotation velocity:

$$M(r) \propto r, \tag{47}$$

$$\rho(r) \propto \frac{1}{r^2} \tag{48}$$

Which can lead to a parametrized density in the following way:

$$\rho(r) = \frac{v(r)^2}{4\pi G r^2}(1 + 2\frac{d\log v(r)}{d\log r}) \tag{49}$$

With $v(r)$ becomes constant at large distance, which much the hypothesis of the invisible dark matter contribution in the galaxy mass.

Calculation in Ref.[19] shows that in the case of the Milky Way, the study of rotation curve yield to a local dark matter density (average over a volume of a few hundred parsecs in the Solar neighbourhood) of $\rho = 0.36 \pm 0.02$ GeV.cm^{-3}.

1.8.2 Gravitational Lensing

Using optical and x-ray telescopes and Sunyaev–Zeldovich effect [20], to observe galaxy clusters, defined as a concentration of thousands of galaxies gravitationally bound, and

embedded in hot x-ray–emitting gas, confirmed evidence that the overall mass required to explain observations is significantly bigger than the measured baryonic content of galaxies and gas. According to the general theory of relativity, massive objects like galaxy clusters bend or lense light. Because the strong gravitational field of the cluster curves the space around them. On their route to our telescopes, light beams emanating from objects behind the cluster travel along curved pathways rather than straight ones. Moreover, the pictures of strongly lensed sources are warped into arcs because light from various sides of the same galaxy travels along somewhat different routes, as shown in Figure 6. The deflection angle of a given lensing cluster of mass M and impact parameter d is [21]:

$$\hat{\alpha} \approx \frac{4GM}{dc^2}, \tag{50}$$

The overall mass M of a cluster can be inferred from measurements of the deflection angle

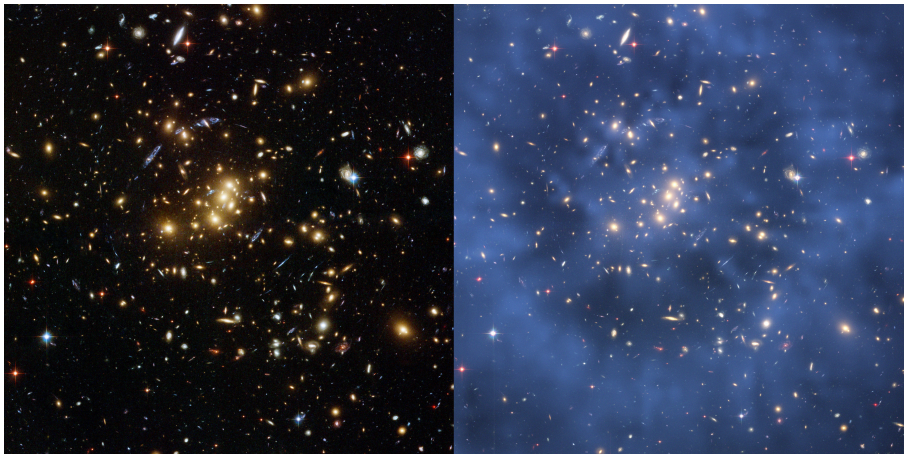

Figure 6: Hublle image of the galaxy cluster Cl 0024+17 is shown. In the left, galaxies are shown in yellow and the blue arcs are the magnified and distorted images of galaxies located far behind the cluster. The process is called gravitational lensing where the light is distorted and amplified by the immense gravity of the cluster. The missing dark matter that account for this process is added in blue in the image on the right. Credit: NASA, ESA, M. J. Jee and H. Ford (Johns Hopkins University).

and impact parameter, which implies existence of dark matter mass contributing to the total mass M of the cluster [22].

1.8.3 Dark matter properties

After establishing firmly the existence of dark matter, its particle candidates should satisfy several requirements to not present the case of baryonic matter.

Dark matter particles must have no electrical charge and no interactions with electromagnetic photons or at least assuming that these particles have extremely small charge fe, with e is the electric charge and $f << 1$. Observations of dark matter density perturbations require that f the ratio of the dark matter to electronic charge, is less than 10^{-6} for $m_X = 1$ GeV, rising to $< 10^{-4}$ for $m_X = 10$ TeV [23].

Dark matter self-interactions are investigated to explain small scale structure observations that contradict the collisionless cold dark matter predictions like the core-cusp problem and the missing satellites problem, over a wide variety of mass scales, including dwarf galaxies, low and high surface brightness spiral galaxies, and galaxy clusters [24]. In the bullet cluster collision, the lack of deceleration of dark matter constrains its self-interaction cross-section to $\sigma_{DM-DM}/m < 1.25\ cm^2/g$ at 68% CL [25]. Also combining measurements from 72 collisions observed using the Chandra and Hubble Space Telescopes, the existence of dark mass is confirmed at 7.6 σ significance, and the dark mass's position has maintained its alignment implying a cross-section for dark matter self-interaction of $\sigma_{DM-DM} < 0.47 cm^2/g$ at 95% CL [25]. Thus, the level of Dark matter self-interaction is constrained and need to be small.

Dark matter particles mass provides a useful criterion for distinguishing between its different candidates: i.e, axions with the mass $\sim 10^{-6}$ eV, sterile neutrinos with mass of some keV, and supersymmetric (SUSY) particles with mass ranging from eV to hundreds of GeV [26–28]. Quantum effects, such as Pauli's exclusion principle for fermionic DM particles, constrain the lower limits for tiny dark matter masses, i.e: the Tremaine-Gunn limit is a lower limit on fermionic DM masses based on studies of velocity dispersion, which is equivalent to the measure of the enclosed mass and physical density in dwarf galaxies. It concludes that the dark matter mass in clusters can't be explained as steaming from leptons of mass less than 1 MeV (e.g, muon or electron neutrinos) [29]. Evaluating the density profile for dwarf galaxy cores of size larger than 130 pc [30], shows a conservative lower bound for fermionic dark matter mass at 70 eV.

To be able to play its role in structure development of the universe and to fulfill the astronomical observations, dark matter must be stable and its lifetime to be at least comparable to that of the universe. Which results in the case of cold dark matter in a lower bound on the lifetime given by 160 Gyr to 200 Gyr at 95% confidence level [31].

1.8.4 Dark matter models

To better understand dark matter from a particle physics perspective, many models for its candidate particles have been developed in frameworks that address solutions to other open issues in particle physics, such as Weakly Interacting Massive Particles (WIMP) for electroweak-scale new physics, which consider the hierarchy problem, axions for the strong CP problem, and sterile neutrinos for the problem of neutrinos mixing and masses.

1.8.4.1 Axions particles

Axions are hypothetical particles originally introduced to address the Standard Model's two failures, the cosmic matter-antimatter imbalance and the strong force's CP symmetry. Later, they become one of the leading particles candidates for dark matter. The Strong CP Problem is solved if the term with field strengths in the Standard Model action density Lagrangian is replaced by [32]:

$$\mathcal{L}_{axion} = -\frac{1}{2}\partial_\mu\varphi\partial^\mu\varphi + \frac{g^2}{32\pi^2}\frac{\varphi(x)}{f}G^a_{\mu\nu}G^{\mu\nu}_a \tag{51}$$

where $\varphi(x)$ is the new scalar field called axion field, and f is a constant with energy dimension, called also the axion decay constant. Based on the mode of production in the early universe,

two types of axions can be distinguished, thermal produced via thermal processes, and cold axions which are the quanta of oscillation of the axion field that result from the turn on of the axion mass [32].

Since their emergence, many searches looking for axions like particles fail to find any, but help in narrowing the windows mass for these particles. The study of the red giant ruled out the region fron 0.5 eV to 200 keV if axion has negligible coupling to the electron, and even lower to 10^{-2} eV if the electon and the axion have an important coupling [33]. The range from 3 10^{-3} to 2 eV is eliminated by observations of the duration of the neutrino pulse from supernova 1987a [34], which lead finally to an open window of $m < 10^{-3}$ eV for axions mass.

1.8.4.2 Sterile neutrino particles

Right-handed neutrinos are motivated in beyond Standard Model extensions to explain the issue with neutrino mass. They don't interact with any Standard Model particles due to their property of being uncharged under the $(SU(3) \times SU(2) \times SU(1))$ Standard Model gauge group, which is why they are called "sterile". The lack of interactions with ordinary matter makes them a viable dark matter candidate for all possibilities of hot, warm, and cold dark matter. The mixing in $SU(2)_L$ interactions is constrained in order that the lifetime exceeds the age of the universe. Sterile neutrino dark matter is required to be relatively light (keV-GeV).

1.8.4.3 WIMP DM particles

Weakly interacting massive particle, abbreviated to WIMP, were the first sort of particles suggested for dark matter in many beyond Standard Model extensions. They are predicted to be stable, neutral, weakly interacting, with mass up to 10 TeV. As example, in supersymmetry, WIMP are considered to be neutral spin-1/2 Majorana fermions called neutralino. Other non supersymmetry model includes extensions with a Higgs, Z, $Z^{'}$ portals or universal extra dimensions [35].

The WIMPs are motivated to satisfy the needs of cosmology and considered to be produced naturally as thermal relics of the Big Bang with densities required for dark matter. WIMPs abundance becomes Boltzmann suppressed when the temperature goes below the WIMPs mass, and WIMPs can no longer find each other to annihilate. The remaining WIMP particles form a prehistoric relic population that remains today. The relic density deduced from the Boltzmann equation for the WIMP density is given by [36]:

$$\Omega_X \propto \frac{1}{<\sigma v>} \sim \frac{m_X^2}{g_X^4} \tag{52}$$

Where $<\sigma v>$ is the thermal average of the dark matter pair annihilation cross section times the relative velocity and m_X and g_X are the dark matter particle mass and the coupling entering this cross section. Assuming a relic density value of ~ 0.2, leads to a dark matter particle of mass around 100 GeV.

Chapter 2:

Experimental Setup

The Large Hadron Collider (LHC) has the most energetic beams ever achieved, which makes of it the most powerful accelerator of particles ever built. It is situated at CERN (the European Organization for Nuclear Research) near Geneva, in the Switzerland-France borders. The LHC lies around 100 m below the surface in a circular tunnel of 27 km long. It was anticipated that the LHC will accelerate protons and heavy ions to energy of up to 14 TeV at center of mass in proton-proton collisions. The LHC is a machine extremely sophisticated and meticulously optimized to study particles-properties in the Standard Model, test its predictions and to search for new physics at high energies. It consists mainly of three essential parts, the collider, the detectors and the computing grid. Detectors are giant experiments able to reconstruct what happened during the collisions. While the computing grid provides global computing resources to store, distribute and analyse the data collected from the LHC operation.

2.1 The Large Hadron Collider

Protons have to be made from hydrogen gas and then go through a variety of pre-accelerators as shown in Figure 7, before reaching the LHC two rings to attend the maximal energy sought. The journey begins with the injection of hydrogen gas into a metal cylinder bathed in an electrical field, which causes the gas to break down into protons and electrons. The particles are propelled to 1.4% of light speed at the Duoplasmatron exit, where they are sent to a radio frequency quadrupole. They get accelerated and concentrated before being sent into the linear accelerator (LINAC). The linac tank consists of a multi-chamber resonant cavity, tuned to a specific frequency. Which generates potential differences in the cavities that accelerate hydrogen ions H^- in several stages. After inauguration of LINAC4 (86 m long) in 2017, particle are able to reach 160 MeV instead of 50 MeV for LINAC2 (36 m long). During injection from Linac4 into the Proton Synchrotron Booster (PSB), ions are stripped of their two electrons when passing through a thin Carbon foil. Only bare protons reach the PSB, which consists of four superimposed rings, that accelerate protons from 50 MeV to 1.4 GeV and up to 2 CeV when the beam is injected from LINAC4. The protons are then transferred to the Proton Synchrotron (PS), which is a 628 m circumference circular accelerator. PS can also accelerate heavy ions from the Low Energy Ion Ring (LEIR). The PS is in charge of providing 81 bunch packets with a 25 ns spacing that are accelerated to up to 25 GeV. Then packets are gathered in a triplet and injected into the Super Proton Synchrotron (SPS), which is a 7 km circumference circular accelerator where particles are accelerated to energies of 450 GeV and sent to the LHC rings where they gain energies up to 7 TeV for each beam.

At this stage, in two independent vacuum chambers, two beams of ions or protons flow in opposite directions. The two rings are made up of eight arcs; where the superconducting dipole magnets that deflect particles are mounted; and of eight Long Straight Sections (LSS);

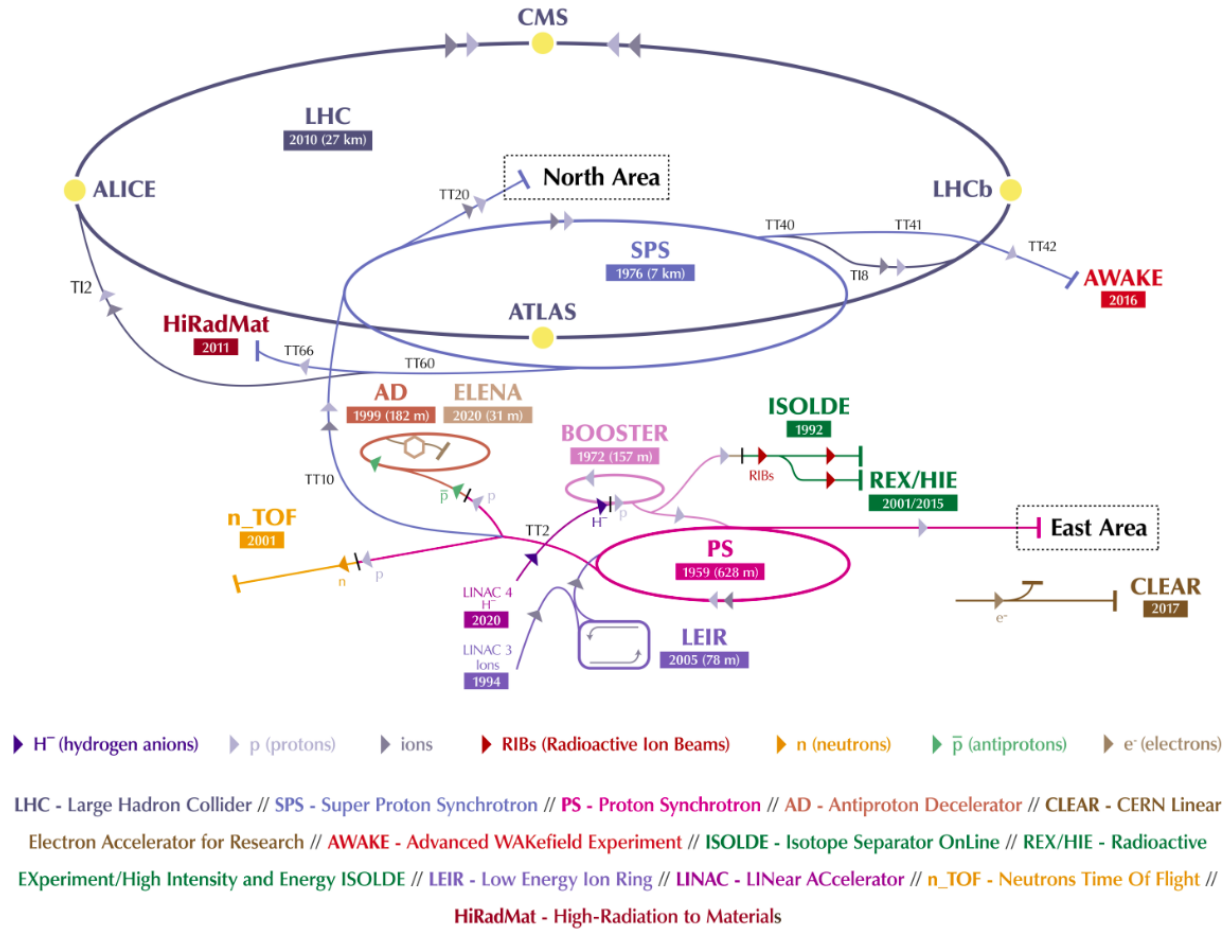

Figure 7: CERN accelerators complex, with the proton path from LINAC to the LHC ring [37].

which house the collimation system for beam cleaning, as shown in Figure 8.

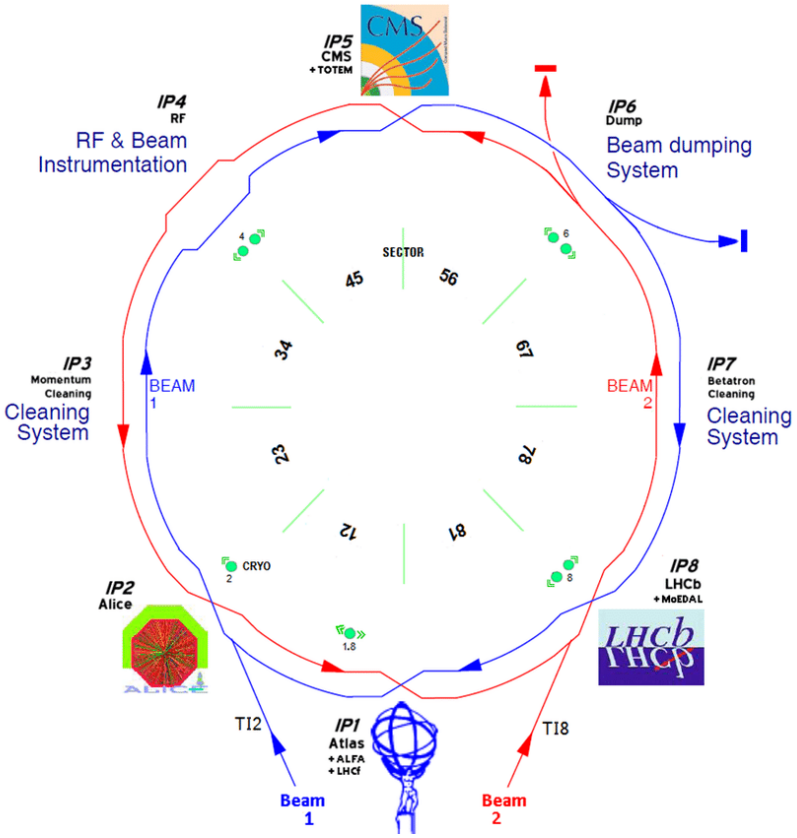

Figure 8: The eight interaction points labelled IP1 to IP8. ATLAS, ALICE, CMS and LHCb experiments are respectively installed in IP1, IP2, IP5 and IP8 [38].

The strongest magnets in the world are employed to guide and focus the LHC beams. They produce an 8.3 T uniform magnetic field and were designed using the best industrially scalable technologies available at the time. In order to preserve superconductivity, a cooling system is required to preserve the magnets at cryogenic temperatures below 2K. The beams are guided around the circular tunnel of the LHC by 1232 dipole magnets. Before the beam approaches a detector, it is focused using quadrupole magnets to optimize particle interactions. Inside the detectors, The beam is constricted to a size of 16 nm instead of 0.2 mm [39].

2.1.1 LHC Experiments

Four interaction points (see Figure 8) where the LHC's proton beams intersect each other are home to particle detectors. The two largest general-purpose detectors, CMS (Compact Muon Solenoid) and ATLAS (A Toroidal LHC ApparatuS) [40], are built to carefully study SM properties, and ultimately search for beyond SM physics. The forward detector LHCb (LHC beauty) [41] focuses primarily on the physics of bottom hadrons to investigate CP-violating phenomena in the early cosmos. Heavy ion collisions are studied by ALICE (A Large Ion Collider Experiment)[42], with a focus on the quark-gluon plasma and hadronization

processes. Alongside the four main experiments are several minor ones: ToTEM (TOTAL cross-section, Elastic scattering and diffraction dissociation Measurement) [43] evaluates the total cross-section of proton-proton interactions and the internal structure of the proton, while LHCf (LHC forward) [44, 45] focuses its efforts in forward regions to simulate cosmic rays in a controlled environment. MoEDAL (Monopole and Exotics Detector at the LHC) [46] searches for magnetic monopoles.

2.1.2 Luminosity and Pileup

The LHC beam's bunch structure was created to maximize the number of proton–proton collisions. The luminosity, which can be quantified as the amount of data collected when integrated across time, is the rate at which data are collected. Given that many uncommon and exotic processes are known to have very small cross sections, a high luminosity enhances the physics agenda of the LHC. A big data set further improves the possibilities of observing and measuring these uncommon phenomena, even though higher collision energy increases the likelihood of these processes occurring. The event rate production is defined in terms of cross section and Luminosity:

$$\frac{dR}{dt} = L.\sigma_p \tag{53}$$

The instantaneous luminosity L is defined as the sum of proton bunches luminosity L_b defined in terms of the average number of inelastic p-p collisions per bunch crossing μ and the evolution frequency f_{rev}, and a calibration constant σ_{vis}:

$$L_b = \frac{\mu f_{rev}}{\sigma_{vis}}$$

$$L = \sum_{b=1}^{n_b} L_b = n_b \frac{< \mu > f_{rev}}{\sigma_{vis}} \tag{54}$$

The ultimate figure of merit is the integrated luminosity for a running period t:

$$L_{int} = \int_0^t L.dt \tag{55}$$

The integral is calculated throughout the sensitive time, ignoring any potential dead time. The integrated luminosity is measured in cm^{-2} and is commonly given in inverse barn fb^{-1}, where 1 $\text{fb}^{-1} = 10^{-24} cm^{-2}$. During run–2, the LHC supplied a total integrated luminosity of 156 fb^{-1} to ATLAS, which recorded 147 fb^{-1} as shown in Figure 9. For calibration purposes, the luminosity can be expressed in terms of the LHC beam parameters:

$$L_b = \frac{\mu f_{rev} n_1 n_2}{2\pi \sum_x \sum_y} \tag{56}$$

Where n_1 and n_2 are the numbers of protons in the two colliding bunches, $\sum_x$ and $\sum_y$ are the convolved beam sizes in the horizontal and vertical planes [47, 48]. To account for other

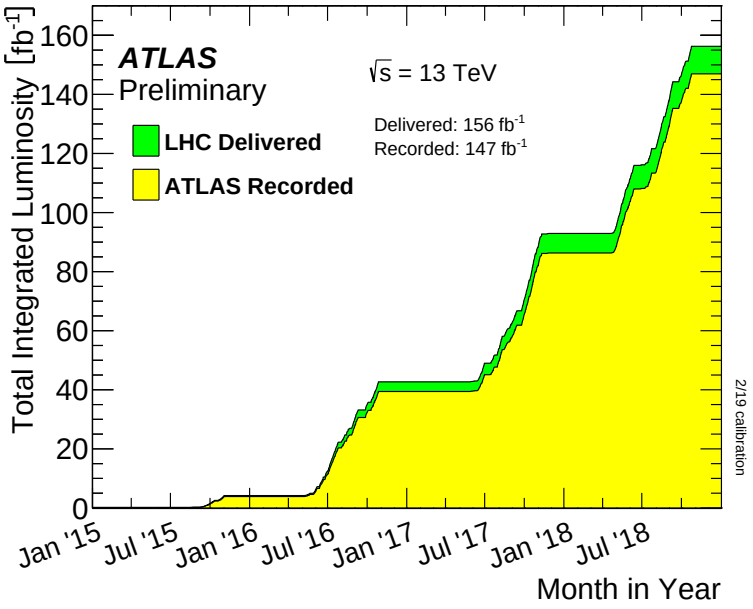

Figure 9: Integrated luminosity given as function of time delivered to ATLAS at $\sqrt{s}$ =13 TeV in LHC run–2. The green indicate LHC delivered data while yellow indicate recorded data by ATLAS during stable beams of p-p collisions.

effects in LHC beams such as the influence of crossing angle and the hour glass effect, a more sophisticated formalism with extra correction factors can be examined i.e [49, 50]:

$$L = \frac{\gamma_r f_{rev} n_b n_1 n_2}{4\pi\epsilon^*\beta^*}.F(\theta_c, \sigma_Z, \sigma^*) \tag{57}$$

Where γ_r is the relativistic gamma-factor, ϵ^* is the RMS normalised transverse emittance, and β^* is the beta-function at the collision point.

The total cumulative quantity of data gathered during an LHC run is then presented by the integrated luminosity. The average number of interactions per bunch crossing is large and referred to as pileup (the average pileup $< \mu >$ is given in Equation 58).

$$\mu = \frac{L_B.\sigma_{ine}}{f_{rev}} \tag{58}$$

Interactions stemming from hard scatter where the quark and gluon components of the protons interact, can provide answers to the most intriguing physics puzzles, but these events are much more uncommon. Each bunch crossing consists primarily of soft, uninteresting, inelastic scattering interactions that create an in-time pileup and contaminate events from the hard scatter processes. Due to some subsystems' time resolution exceeding the time interval between bunch crossings, out-of-time pileup might happen when interactions from one bunch crossing are observed with the next one. Applying minimum momentum criteria on physics objects to reject the soft pileup items can mitigate pileup.

Physics processes cross sections are measured in units of barns (10^{-24} cm^2), therefore multiplying the cross section by the total integrated luminosity of a data set provides the

number of events for a particular physics activity. Each of the four years of run–2 had a highly diverse pileup environment, resulting in a high overall value (see Figure 10). Only detector objects that are found to match to a certain defined hard scatter vertex are taken into account because of the run–2 enhanced pileup conditions.

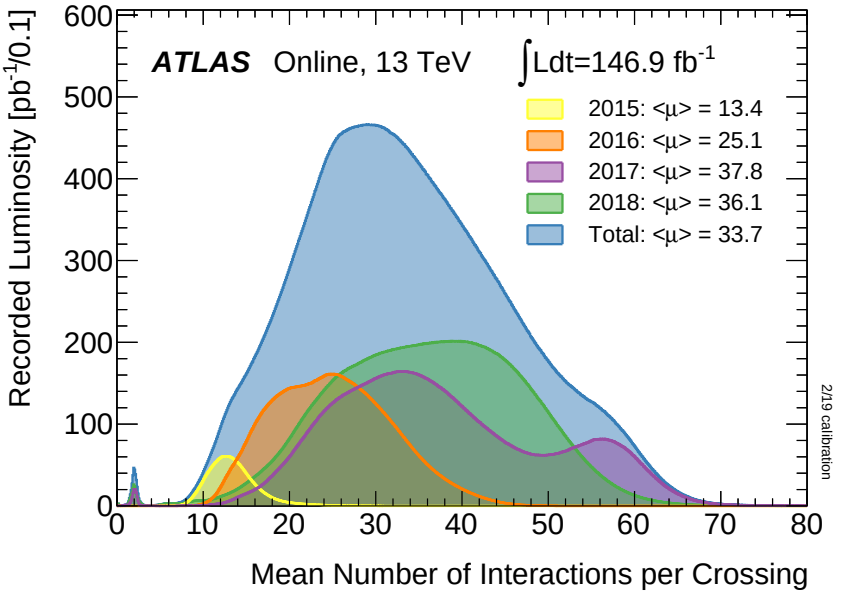

Figure 10: Luminosity weighted distribution of the mean number of interactions per crossing for the run–2 p-p collision data at $\sqrt{s}$ =13 TeV collected by ATLAS at the LHC.

2.1.3 LHC runs

On September 10, 2008, the first LHC single beams were measured. Sadly, after early successes, a serious malfunction forced the LHC program to be suspended for more than a year. On November 20, 2009, when data from the first circulating beams following the failure were collected, the LHC resumed its program. Shortly after, on November 30, 2009, the LHC surpassed the previous record-holder Tevatron and became the particle accelerator with the highest energies ever achieved, hitting 1.18 TeV per beam. In 2011, the ATLAS and CMS detectors recorded around 5 fb^{-1} of data at a center of mass energy of 7 TeV for the LHC. Proton-proton collisions were resumed on April 5th, 2012, and continued through the intended long shutdown, which ended the LHC program's run-1 on December 31, 2012. Around 20 fb^{-1} of proton-proton collision data were collected by the ATLAS and CMS detectors at $\sqrt{s}$ = 8 TeV. On June 3, 2015, the start of run-2 data collection, the LHC restored stable beam conditions with an unparalleled energy of 6.5 TeV per beam, leading to a center of mass energy of $\sqrt{s}$ = 13 TeV. During the years 2016, 2017, and 2018, data on proton-proton collisions at $\sqrt{s}$ = 13 TeV were collected, generating a total integrated luminosity of about 139 fb^{-1}. The results presented in this work are part of run–2 efforts on searching for dark matter particles through invisible Higgs decays. Table 1 summarizes the important improvements on the beam parameters during the four runs scheduled by CERN for the LHC.

Table 1: Important parameters for different LHC runs

parameters	Design	run–1	run–2	run–3	run–4
$\sqrt{s}$ (TeV)	14	7/8	13	14	14
Bunch spacing (ns)	25	50	25	25	25
Bunch Intensity (10^{11} ppb)	1.15	1.6	1.2	1.8	2.2
Number of bunches	2800	1400	2500	2800	2800
Emittance (μm)	3.5	2.2	2.2	2.5	2.5
β^* (cm)	55	80	30-25	30-25	~ 15
Crossing angle (μrad)	285	-	300-260	300-260	TBD
Peak Luminosity ($10^{34} cm^{-2} s^{-1}$)	1.0	0.8	2.0	2.0	5.0
Peak pileup	25	45	60	55	150

2.2 The ATLAS Detector

With about 4π solid angle coverage all over the interaction Point 1 (IP1), the ATLAS is a multipurpose particle detector that was designed to be sensitive to a wide variety of physics signatures. It is the largest of two such detectors at the LHC, measuring 44 m in length and weighing almost 7000 tonnes. Similar physics objectives are served by CMS, which is located at Point 6 (IP6) across the ring. It is designed for the search for new physics and the evaluation of precise measurements of the Standard Model of particle physics. The sensitivity of searches as well as the precision of measurements depends crucially on the ability to accurately reconstruct the full four momenta of each particle from its energy deposits in the detector. The detector must therefore be designed to provide a high energy, momentum and angular resolution. The latter is also important to distinguish close-by particles in the dense event topologies that result from the decays of highly-energetic massive particles, such as top quarks. Furthermore, the detector must be designed in a way to allow the identification of different particle such as electrons, muons and hadrons. Given the large cross-sections and the diversity of processes with purely hadronic final states; typically for a hadron collider like the LHC; the ability to distinguish different types of hadrons such as pions, kaons and heavy-flavour states is also desirable. The ATLAS detector longitudinal view, is shown in Figure 11. The Inner Detector, which is responsible for particle tracking and vertex identification, calorimeters, which are essential for measuring the energy of electrons, photons, and jets, and muon spectrometer, which is required to accurately reconstruct muon momenta, are the sub-detectors that make up the ATLAS detector. The individual sub-detectors are summarised in the following sections.

2.2.1 The Magnet System

In order to measure particle momentum and charge, the magnet system is an essential component of the detection systems that must be operational. Inner solenoid, barrel toroid, and end-cap toroids are the three components that make up the whole system. Around the inner detector is where the superconducting inner solenoid is situated. The resulting

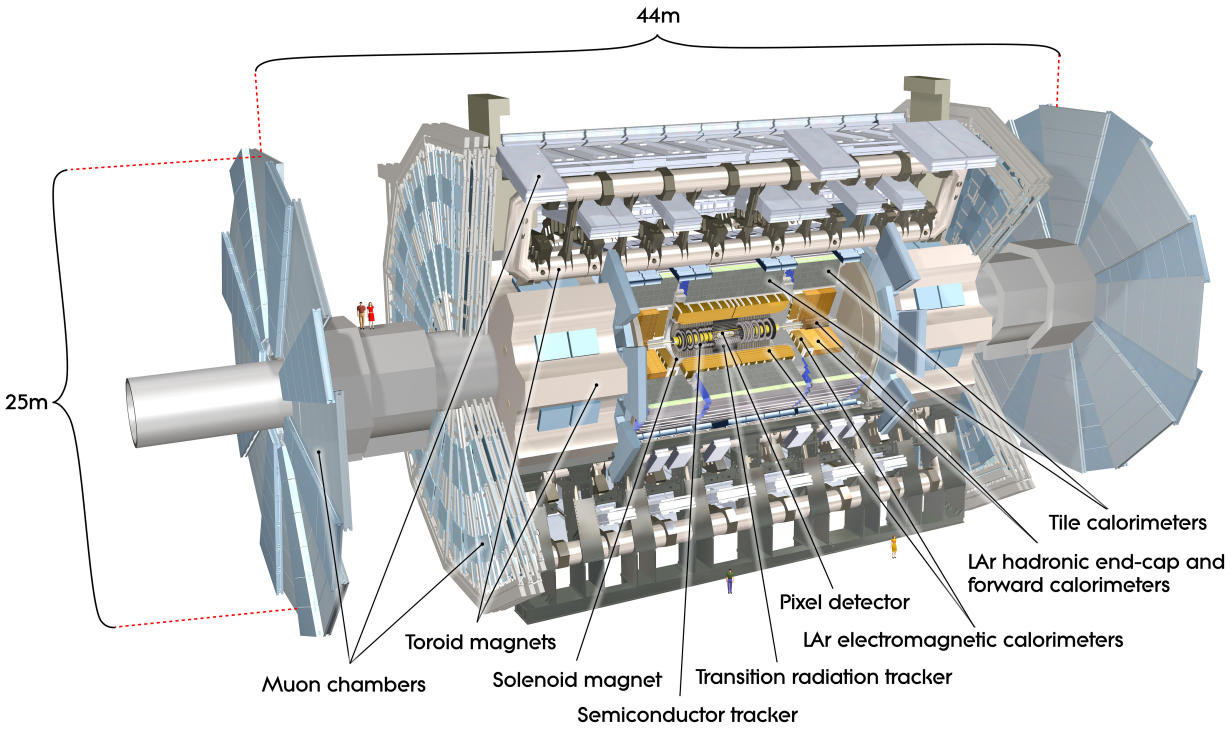

Figure 11: Schematic of the ATLAS detector configuration, showing different parts of the sub-detectors and magnet system [51].

2T magnetic field is largely homogenous. Having a thickness of just 0.66 radiation length, the inner solenoid is extremely thin in order to absorb as little as possible of the particle energy. The solenoid has an axial length of 5.8 m, 2.46 and 2.56 meters for its inner and outer diameters, respectively. To generate a strong magnetic field, the solenoid is constructed of NbTi conductor. The calorimeters are encapsulated by the barrel toroid, which comprise eight coils contained within vacuum vessels made of stainless steel. The barrel toroid measures 25.3 m in length, 9.4 m in interior diameter, and 20.1 m for the outer. The Muon Spectrometer uses the 4 T magnetic field that the barrel toroid produces to evaluate the momenta of muons as their tracks bend in the magnetic field. Similarly to how a barrel toroid functions, end-cap toroids also do. The end-cap toroids' magnetic field is tailored specifically for the end-cap muon spectrometer. Eight flat, square coil components make up each end-cap toroid. The coils are put together in an insulating vacuum tank that is 11 meters diameter and 5 meters wide.

2.2.2 The ATLAS Coordinate System

ATLAS uses right-handed coordinate system. The origin of the coordinates is defined to be the interaction point IP1 at the center of the detector. The z-axis is parallel to the LHC beam pipe, and the x-axis pointing toward the center of the LHC, while y-axis is pointing toward the surface. The x-y plane is perpendicular to the z-axis and it is called transverse plane. It is described using r-ϕ coordinates as shown in Figure 12. ϕ is the azimuthal angle in the transverse plane from the x-axis to the given position, and r is the radial distance to the z-axis. The polar angle θ is measured from z-axis. Often the pseudorapidity is more

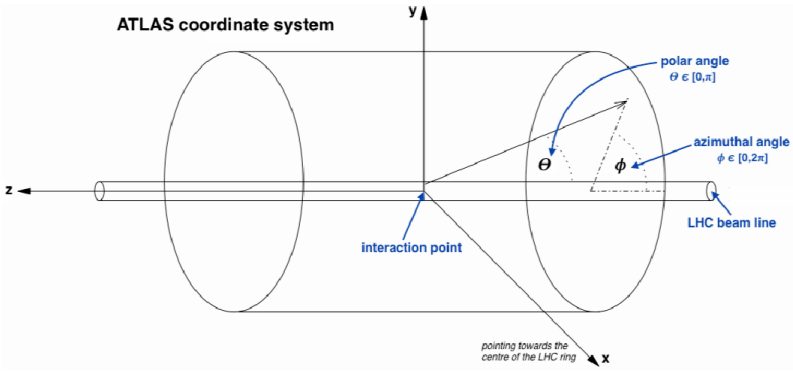

Figure 12: Schematic of the ATLAS detector coordinate system [52].

common, and is defined as:

$$\eta = -\ln\tan(\frac{\theta}{2}) \tag{59}$$

An important parameter for ATLAS analysis is the distance in η-θ space defined as:

$$\Delta R = \sqrt{\Delta\eta^2 + \Delta\phi^2} \tag{60}$$

2.2.3 The Inner Detector

The Inner Detector (ID) is the closest part of the detector to the IP1 interaction point. It is comprised of a very compact and extremely sensitive material to measure the momentum, direction, and charge of electrically charged particles produced in each p-p collision. Pixel Detector, Semiconductor Tracker (SCT) and Transition Radiation Tracker (TRT) are three separate sub-detector systems of the ID, that are all immersed in 2 T magnetic field parallel to the beam axis, and generated by the central solenoid.

Every 25 ns, a Large number of particles emerges from the interaction point toward out-layers, creating a very large track density in the detector. The use of pixel and silicon microstrip trackers with the straw tubes of the TRT is imposed by the high precision requirements on the momentum and vertex resolution needed to achieve the physics benchmark sought by the LHC. Figure 13 shows the sensors and the elements of the ID barrel. It is traversed by a track, that passes through three cylindrical silicon-pixel layers. The Pixel size is 50 x 400 μm^2 for the external layers and 50 x 250 μm^2 for the innermost layer (IBL). The track continue its journey through the four cylindrical double layers covering the region $|\eta| < 2.5$, and the barrel transition-radiation tracker that contains axial straws of 4 mm diameter and 144 cm long.

The pixel detector is made up of three barrel layers known as PIX1, PIX2, and PIX3, as well as two end-caps each with three disks. A fourth Pixel layer was introduced during the Long Shutdown 1 (LS1) to preserve vertexing and tracking performance even in the presence of increased luminosity. It started operating with start of run–2. IBL was put between PX1 and a new reduced-radius beam pipe at a radius of $\sim$ 33 mm, to boost the tracking precision. SCT is a silicon strip detector consists of 4 layers in the barrel named as Barrel 3, 4, 5 and 6, with 9 endcap disks perpendicular to the beam axis in each side. Each module has two planes of silicon with 40 mrad stereo angle, which enables reconstruction of space point of electrically charged particles. The TRT system is a tracking drift chamber, that allows continuous tracking and the identification of the electron using transition radiation from foils or fibers interleaved between the straws. The barrel part cover the range of $|\eta| < 1$ while the end of the two EndCaps cover the region of $1 < |\eta| < 2$.

About 92 million electronic readout channels are used for the pixel detector. The intrinsic accuracy provided by Pixel layers in the barrel is 10 μm in the (R - ϕ) plane and 115 μm along the beam axis (z-axis). In the disks, the precision is 10 μm in(R - ϕ) plane and 115 μm along (R). In the SCT, About 6.3 million readout channels are used to extract information from the sensors, with an intrinsic accuracy per module of 17 μm in the (R -ϕ) plane and 580 μm along the beam axis in the barrel. While in the disks, the precision is 17 μm in the (R - ϕ) plane and 580 μm along (R). TRT uses 350 000 read-out channels and provides measurement with precision of 0.17 mm.

After combination of Pixel, SCT trackers and the TRT, a very strong pattern identification and excellent precision in (R - ϕ) and z coordinates are achieved.

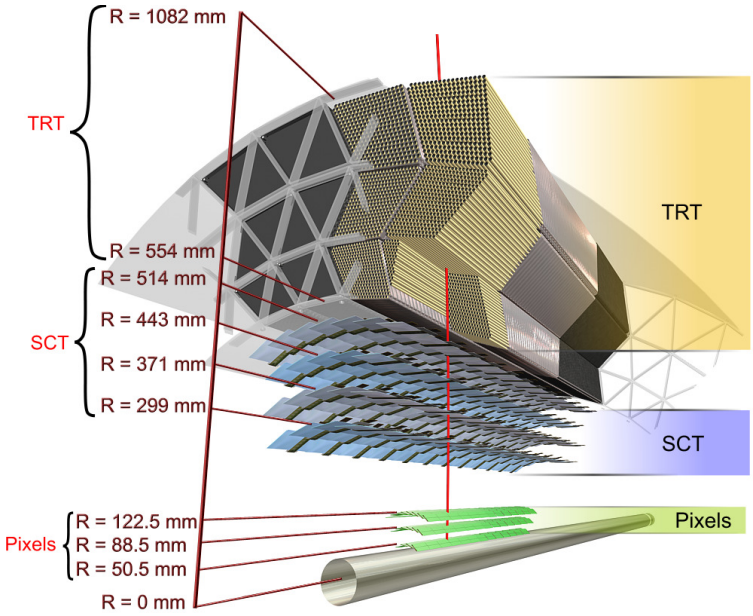

Figure 13: Layout showing the main components of the Inner Detector.

2.2.4 The Electromagnetic and Hadronic Calorimeter System

Unlike tracking detectors like ID, calorimeters use a destructive method for the energy measurement. Charged and neutral particles are forced to deposit all of their energy and stop within the detector. The provided information are accurate measurements of the total energy of the particles with position and missing energy transverse in the case of hermetic detector. They are very well suited detectors for the high energies of the LHC, since their intrinsic resolution is proportional to the energy deposit. So far, two types of Calorimeters can be made, sampled or Homogeneous. The first type is made by interleaving layers of an absorbing high-density material such as Pb, Fe or Cu; that stops incoming particles, with layers of an active detector medium as Si, scintillator or noble liquids used to measure particles energy. The second type made by using single material that serves as absorber and detector in the same time. The material can be i,e BGO, PbWO4 dense crystal scintillators or lead glass.

In front of the calorimeter, in the range of $|\eta| < 1.8$ a LAr presampler detector is installed immediately behind the cryostat cold wall. It is used to correct for the energy lost in the material (tracker, cryostats, and solenoid coil in the barrel region, etc), as well as measurement of the EM shower direction η. Particles emerging from the ID reach the calorimeter system, which consists of an electromagnetic (EM) calorimeter that covers the region of $|\eta| < 3.2$, a hadronic barrel that covers the region of $|\eta| < 1.7$, hadronic end-cap covering region of $1.5 < |\eta| < 3.2$, and forward calorimeters to cover the region of $3.1 < |\eta| < 4.9$. The EM calorimeter and the hadronic calorimeter are shown in Figure 11. Detailed view of different components of the calorimeter is shown in Figure 14. ATLAS EM calorimeter uses sampling technique with lead as absorber and liquid argon (LAr) as a scintillator. An accordion geometry has been chosen to have several active layers in depth, for both the barrel and end-caps. This ensures that no particle escapes unchallenged. A fine-grained position sensitive device is needed to cope with the dominant backgrounds. In the case of electrons and photons,

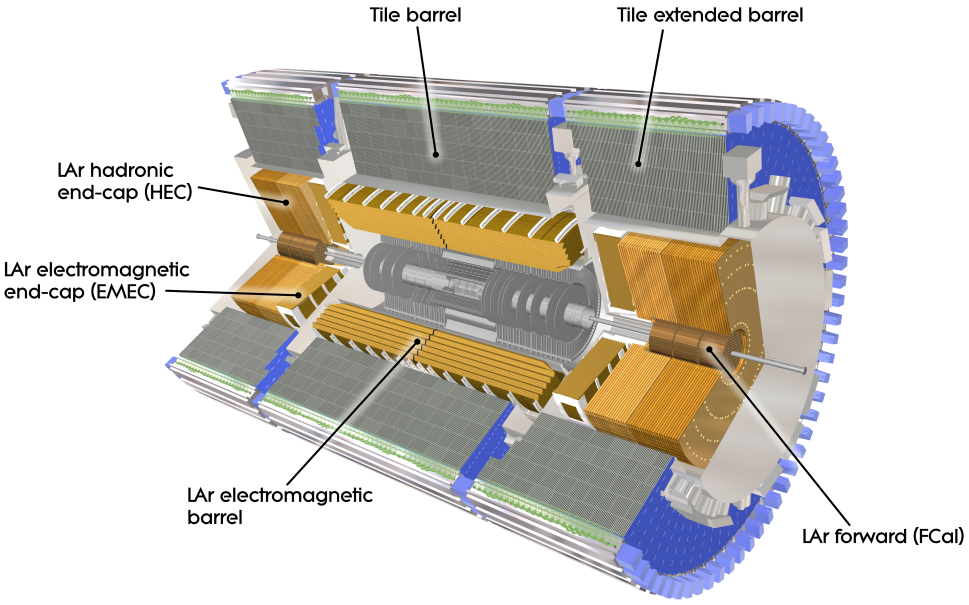

Figure 14: Layout showing the different components of the ATLAS calorimeter.

background arises from the production of hadronic jets. A rejection factor of $\sim 10^4$ is required for $H \to \gamma\gamma$ searches, which can be achieved by $\Delta\eta\Delta\eta \simeq 0.003 \times 0.1$ [51].

The hadronic calorimeter (HCal) surrounds the electromagnetic calorimeter and is designated to measure the energy deposits of hadrons. The hadronization of quarks and gluons via strong interaction produces hadronic parton showers, which are absorbed within the HCal. Covering a pseudorapidity range of up to 4.9 in $|\eta|$, different techniques are used to accommodate the various requirements. The tile calorimeter over the range of $|\eta| < 1.7$ is a sampling calorimeter using iron as passive material and scintillating tiles as active material. It consists of the tile barrel and two tile extended barrel sections. The next subsystem within the hadronic calorimeter is the LAr hadronic end-cap calorimeter along the z-axis at both sides of the barrel, built with copper plates as absorber material and liquid argon as active material. The end-caps cover an $|\eta|$ range up to 3.2, overlapping the forward calorimeter thereby. The forward calorimeter (FCal), also using LAr as active material, faces high level of radiation due to its position about 4.7 m from the interaction point along the beamline. It consists of three sections, varying in the choice of the passive material: the first is built from copper, while the other two are made out of tungsten.

2.2.5 The Muon Spectrometer

Muon system is the outermost part of the ATLAS detector. It measures with high accuracy the trajectory and momentum of muons steaming from the p-p collisions in the IP1 interacting point. It comprises about 4000 chambers, that makes 4 different components: Thin Gap Chambers (trigger chamber for endcap), Resistive Plate Chambers (trigger chamber for barrel), Monitored Drift Tubes, and Cathode Strip Chambers.

The space covered by the spectrometer can be divided to three regions: the region of $|\eta| \leq 1.2$ covered by barrel extending, the regions of $1 \leq |\eta| \leq 2.7$ covered by the two End-Caps. The barrel is filled with the magnetic field generated by the eight coils of the ATLAS toroids. The field integral in the barrel varies as function of the azimuthal coordinate from 2 to 5 Tm. The saggitta of the muon trajectory caused by the magnetic field is used to calculate the momentum. Muons trajectory is provided by the monitored drift tubes arranged in three stations of monitored drift tube (MDT) precision chambers in cylindrical layers inside the toroid (Figure 15). Cathode strip chambers (CSC) are employed instead of MDTs in the MS's innermost end-cap wheels [53]. Tubes are filled with a gas mixture of argon and carbon dioxide.

Each layer provides position measurement with $\sim 50\ \mu m$ precision, in order to provide high resolution measurement of momentum ranging from 5 GeV to 1000 GeV.

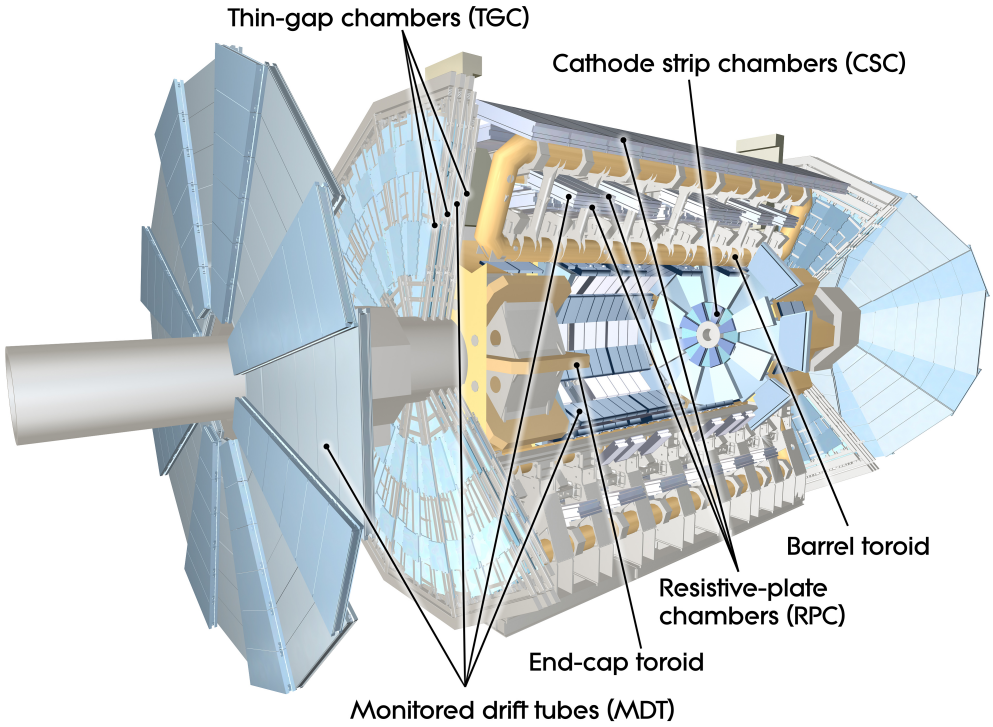

Figure 15: Schema of the Muon Spectrometer's main components in the ATLAS detector [54].

The muon spectrometer has an optical alignment system that tracks the positions of chambers in relation to each other and to the calibrated reference objects in the detector, as well as their deformations, in real time. Using χ^2 minimisation calculated from sensor measurements with a detailed mathematical model of the chambers and reference objects. The mathematical model of the chambers is tweaked to match the real and simulated sensor measurements as closely as possible. "Alignment corrections" are the name for these shifts and rotations [53].

Muon Spectrometer played a crucial role in ATLAS Higgs discovery, and it is also designed

to follow the LHC program aiming the detection of beyond Standard Model particles.

2.2.6 Trigger system and Data Acquisition

The Trigger and Data Acquisition system (TDAQ) [55, 56] is responsible for deciding whether or not an event from a given bunch crossing is stored for later analysis. At a rate of 40 MHz, there are around one billion collisions every second. Since each raw event is about 1.6 MB in size, it would take about 64 TB/s to read out and store all of this data [57, 58]. The bandwidth of the readout systems of the detector and the storage capacity of computers place a limit on the amount of data that can be saved. This implies an exigency of a TDAQ system, which during data gathering may identify interesting events in real time. The Level 1 (L1) trigger, based on hardware, and the High Level Trigger (HLT), based on software, are the two distinct levels used by the ATLAS trigger system for run–2. A trigger menu lists the different types of requested physics objects and arranges selected events based on the L1 and HLT criteria they satisfy before allowing them to be read out into permanent data storage after passing from L1 (see Figure 16). The hardware-based L1 takes into account signals from the calorimeter and muon systems to reduce the data from the 40 MHz event rate provided by the LHC to around 100 kHz. η and ϕ are used to define regions of interest (RoI), which regarded as locations with important energy deposit (muon p_T is used instead of energy deposit) that was probably caused by the formation of a physics object (photon, electron, muon, jet, tau). The Central Trigger Processor, which takes object multiplicities into account, considers more general detector-wide kinematic, i.e., events with two forward jets or missing transverse energy, for instance, can be chosen. The central trigger processor uses the timing information from the detector subsystems, to determine if the event is accepted (meets the requirements) or not. This determines if the event that passed the L1 trigger take place in coincidence with a collision at the interacting point. Such decision is made in 2.5 micro seconds, while collecting data. The RoIs are subsequently sent to the software-based HLT if they are accepted. By running over a processor farm with about 40,000 processor cores, the RoI are used by the software to produce pseduo-reconstructed physics objects in less than 300 milliseconds. Several object or event criteria known as chains [59] are provided by the trigger menu, i.e., the menu might define a trigger chain that require at least one jet with an energy greater than 100 GeV at L1 level. If the event contains objects that satisfy the relevant HLT requirements, it is stored. Depending on the requirements of the readout stream, partial or complete event reconstruction can be performed. Based on the intended purpose, i.e., for physics analysis, calibration, or monitoring reasons, events may be written to various streams. Given that the entire event is always stored, the physics stream dominates the output saved to long-term storage (which is not the case for the other streams). The 2500 trigger chains must share the 1 kHz event rate that the HLT reduces from 100 kHz. Prescale factors are employed to control the rate at which some triggers read out data. With a factor of N, the trigger rate is kept under control independently of variables like pileup or increasing luminosity. It means that only the N-th passing event is saved. Prescaling is an alternative method used to lower the bandwidth of the calibration and monitoring streams while giving the physics stream as much room as feasible to read out,

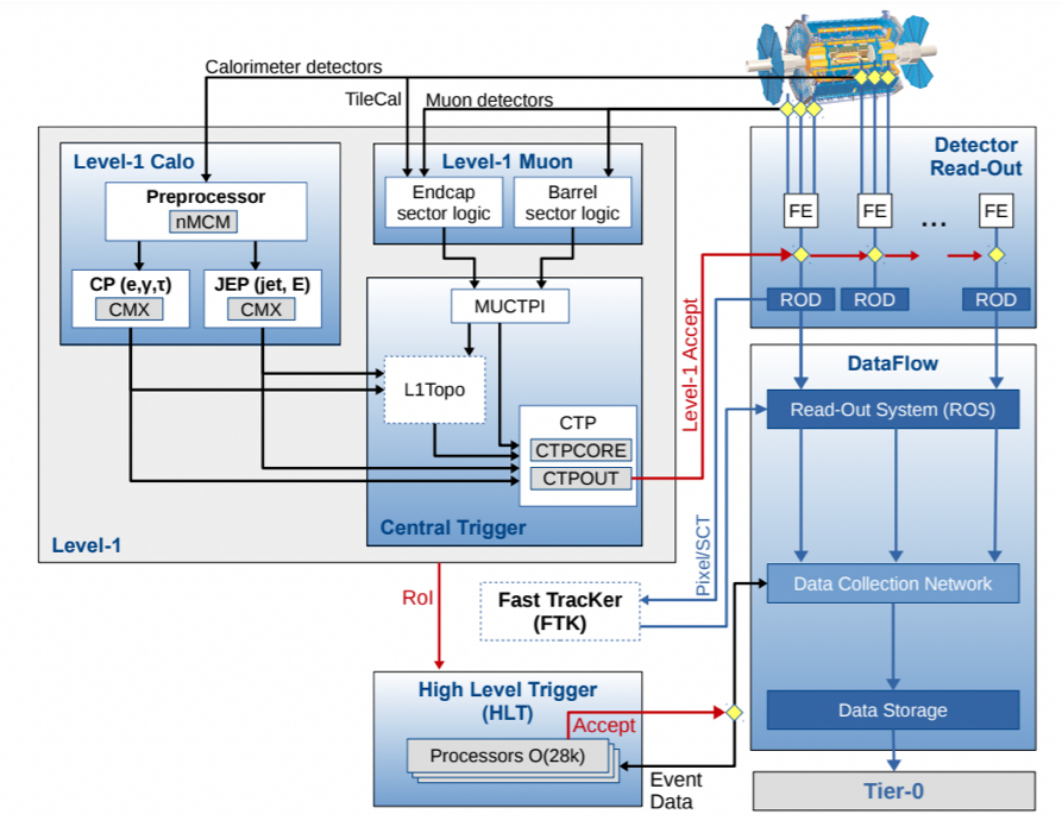

Figure 16: Schematic of the three-level ATLAS detector trigger system [60].

Chapter 3:
Reconstruction and Identification of Physics Objects

Physics objects are the tools by which collisions are reconstructed. Final-state particles are the emitted electrons, muons, photons, and hadrons that survive long enough to interact with the detector. Each leaves behind a unique footprint that is made up of signals in the different subsystems: the ID, the calorimeters, and the muon spectrometer. Physics objects can be a final-state particle such as either photon, electron and muon, or collections of final-state particles. Hadrons are assembled into structures known as jets, which are associated to the color charged particles created in the hard scatter. To recreate the kinetics of any particles that escape the detector and leave no physical traces, the missing transverse energy physics object is constructed utilizing all the other physics objects present in the event. Neutrinos are the only Standard Model particles that can leave the detector with no traces behind. Physics objects associated with final state particles are used to reconstruct short-lived and heavier mother particles, and eventually identify the type of the physics process that took place during the hard-scatter and its kinematics. Even if the reconstruction of physical objects were totally precise, there would still be some uncertainties, since similar final-state particles can be produced from different processes. When targeting a defined type of events in the collected data, a portion of events that mimic the signal and pass the selection are less important and known as background, of which the amounts need to be known precisely. Trigger, reconstruction, and identification are steps involved in creating a physics object. The trigger system is useful for flagging signatures consistent with different types of physics objects by deploying only a limited amount of information that can be analyzed rapidly. Reconstruction algorithms that have access to the full event information, build a physics object candidate with full kinematic information, such as four-momentum. The final step for creating a final set of objects is applying the identification algorithms to the early reconstructed candidates. There is an efficiency that characterizes every mentioned step, because signal objects might fail a stage, and fake rates might pass due to background objects. Fakes include objects not from the hard scatter, objects of the same type but originating from an in-flight decay. Analyses tend to have defined requirements fixed at the stages of trigger and reconstruction. The identification stage is more adjustable and may typically be altered to satisfy the analysis's objectives. In order to obtain the best background suppression for appropriate efficiency, there are a number of widely used "working points" algorithms of identification. Reconstruction and identification of different objects will be discussed below, and the missing energy transverse object will be detailed in Section 4.

3.1 Tracks and Vertices reconstruction

Tracks of charged particles are built using hits in the ID layers of the pixel, SCT and TRT detectors. These hits are primarily used to form clusters. One cluster forms one space-point

in the pixel detector, while two clusters from both stereo views of a strip layer are required to form the space-point in the SCT. The combination of three space-points in the silicon detector are required to form a seed track, with the condition of being originated from 3 different layers. The algorithm can also allow the use of a configurable number of space-points from pixel and SCT for the track seeding. Then the track is reconstructed following three stages, starting by pattern recognition, ambiguity resolution and extension of the track in the TRT detector [61].

For seeds that share multiple space-points from the same layer, the ones with minimum distance between space points are kept while others eliminated. Also, requirements on momentum and impact parameters are used for seeds selection. Seeds are extended following the most likely path using a pattern recognition algorithm. Candidates with values of $p_T > 400$ MeV are fitted using the ATLAS Global χ^2 Track Fitter [62], which resolve ambiguity from tracks with the same hits. At this stage, track parameters are evaluated. To model the energy loss, The pion hypothesis is used in the pattern-recognition algorithm, if the fit fails, a second attempt according to the electron hypothesis is made to prevent inefficiencies for electron tracks with significant bremsstrahlung.

In the case of a perfectly constant magnetic field, the track projected to the transverse plane is a circular trajectory which can be parametrized by the transverse momentum (p), the azimuthal angle (ϕ) and the transverse impact parameter d_0. However, in the case of the ATLAS inhomogeneous magnetic field, two additional parameters are used: the polar angle θ and charge-momentum ratio ($\frac{q}{p}$). Additionally, to account for charged particle energy loss in the detector, a series of subsequent fits using an optimized Gaussian-sum filter (GSF) are performed to the basic cluster measurements for tracks with more than four hits in SCT and that loosely match the EM clusters: The position of primary vertices of the parton interactions (inside the proton-proton collision) is reconstructed using tracks. The positions of secondary vertices, which result from subsequent decays of emitted particles and have the characteristic of being displaced from the interaction point, are reconstructed using tracks. By identifying the z-position of the track origin from the IP, a longitudinal impact parameter z_0 is discovered for each track; the maximum of the z_0 distribution serves as the seed for the iterative vertex finding algorithm. Tracks in the proximity of the seed are weighted according to their level of compatibility with the seed, which alters the seed position. This approach is applied iteratively, with the IP providing a three-dimensional constraint, and ultimately determines which tracks are matched to the vertex and a final vertex position by assigning weights of 1 or 0 to tracks. The process is then repeated until all vertices have been reconstructed for tracks that are not matched to a vertex. The nominal primary vertex in the event is defined as the vertex having the largest value of the sum of associated tracks transverse momentum, that must have at least two matched tracks. This primary vertex is chosen with the purpose of extracting the most interesting physics of an event from the hard-scatter in the collision, and relegates other primary vertices to pileup. Performance of vertex reconstruction is sensitive to the number of interactions per bunch crossing and, thus, suffers from the growing instantaneous luminosity in run–2. It is important to maintain a balance between incorrectly matching tracks from a single parton-parton interaction to different vertices (splitting) and matching tracks from different parton-parton interactions to the same vertex (merging), the latter occurring more often as pileup increases. In run–2, the

vertex reconstruction used an imaging algorithm [63] that takes many vertex locations into account simultaneously (testing tracks with multiple seeds) to avoid merging.

3.2 Electron reconstruction and identification

The trigger system can use a selection chain in all three stages of triggering to initially identify electrons. In order to identify and reconstruct the four-momentum of the electron after a trigger selection, the offline algorithms use electromagnetic calorimeter clusters as seeds, which are later matched to ID tracks. All cluster reconstructions start by the reconstruction of their seeds first. A sliding window clustering algorithm is used for seed reconstruction, and it processes through three steps: tower building, precluster (seed) finding, and cluster filling [64]. Two types of sliding windows are available for ATLAS calorimeters, electromagnetic used for photon and electron and it is named "egamma". The second type is designed for jet finding and tau leptons identification. It is named "combined", and include information from both EM and hadronic calorimeters.

The calorimeter is segmented in $(\eta \times \phi)$ space into a grid of elements with definite size $(\Delta\eta \times \Delta\phi)$, determined by the granularity of the calorimeter. The tower building configuration for the two types is not the same. The EM (combined) calorimeter is divided into a grid of 200×256 (100×64) elements of size 0.025×0.025 (0.1×0.1), within the η range of $|\eta| < 2.5$ ($|\eta| < 5.0$) [64]. The energy of a tower is defined as the sum of energies deposited in the longitudinal cells of the calorimeter layers, in addition to the Presampler in the case of EM calorimeter.

To form a precluster, a window of fixed size $\Delta\eta \times \Delta\phi$ is used to scan over all elements of the grid tower built before. The window transverse energy is defined as the sum of the towers' transverse energy encompassed in the window. In order to acquire the best efficiency for discovering preclusters and to limit the rate of fake ones, the window size and a threshold for the transverse energy are optimized at this stage as shown in Table 2. Precluster position is calculated as the energy-weighted η and ϕ barycentres of all cells within a window of towers surrounding the central one. Defining the position permits the removal of duplicate preclusters. In the case where two preclusters share the same towers, the candidate with the highest transverse energy is chosen. The precluster reconstruction efficiency depends on $|\eta|$

Table 2: Precluster (seed) finding parameters. $(N_\eta \times N_\phi)_{\text{window size}}$ is the window's size of towers in $\eta \times \phi$ plane. If the Precluster have a transverse energy lower than $E_T^{threshold}$, it is not considered. $(N_\eta \times N_\phi)_{\text{window position}}$ is the size needed to calculate the Precluster position. Δ_η and Δ_ϕ is the distance to consider the Preclusters duplicated [64]..

Type	EM	Combined
$(N_\eta \times N_\phi)_{\text{window size}}$	5×5	5×5
$E_T^{threshold}$ (GeV)	3	15
$(N_\eta \times N_\phi)_{\text{window position}}$	3×3	3×3
Δ_η ; Δ_ϕ	2 ; 2	2 ; 2

and E_T, and it improves with E_T. It goes from 65% to 96% for E_T from 4.5 GeV to 7 GeV [65].

Lastly Pre-cluster positions are utilized as seeds to build around them final clusters. EM cluster formation consists of considering all cells inside a rectangle of size 3×7 (in tower unit) in the barrel and 5×5 in the EndCap, and centered arround the seed position. The choice of a large size to accommodate all of the shower is trumped by a smaller size choice to reduce pileup and electronic noise.

Electron interacts mainly through bremsstrahlung while it travel through the detector material, and lose the majority of its energy in the inner detector and the electromagnetic calorimeter. If the emitted photon is energetic enough, the pair production occur and the photon convert to a pair of electron positron that interact also in the detector creating an electromagnetic shower. The electron, positron, and photon all travel through the detector in a cone-like pattern and are considered to be part of the same cluster. Electron reconstruction is based on components that distinguish its signature. In the region of high-granularity of the EM calorimeter and the ID ($|\eta| < 2.47$), two components are used: localised clusters of energy deposits in the EM calorimeter and tracks of the ID (see Figure 17). Tracks and clusters are ensured to match closely in $\eta \times \phi$ space to obtain the electron candidates.

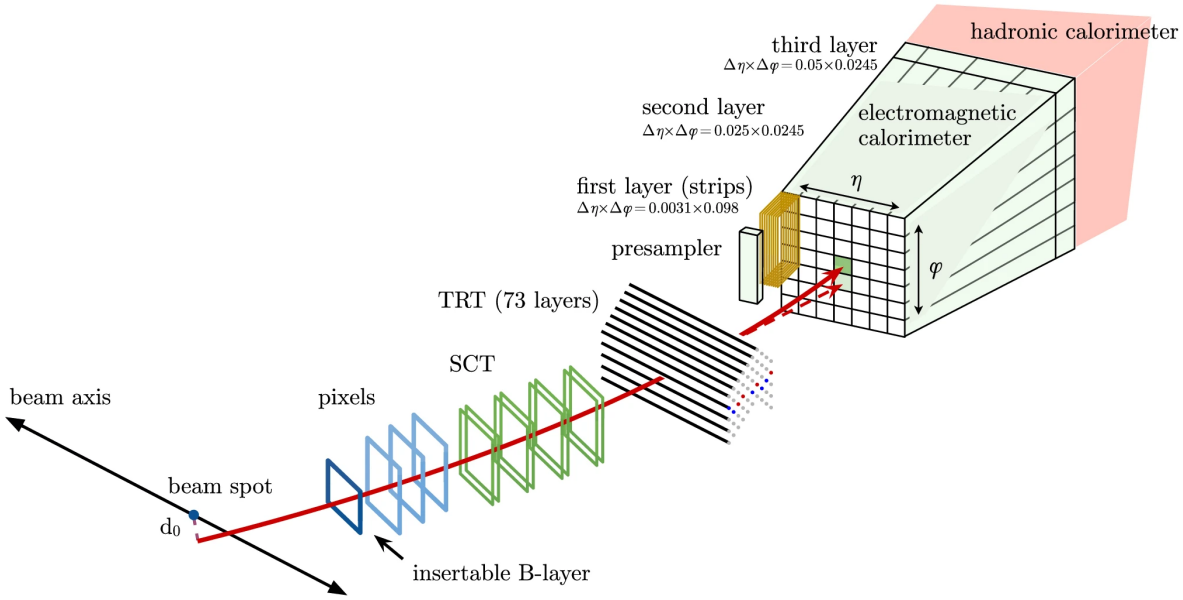

Figure 17: Schematic representation of an electron's journey in the ATLAS detector. The red line represent the electron track in the ID subsystems, while the hashed line is for the photon [65].

Regions of interest for the tracks in the ID can be established using the fixed size clusters in the calorimeter with a shower profile compatible with that of an EM one. The matching of the track candidate from GSF and the calorimeter seed is investigated using η and ϕ separation between the track extrapolated position and the calorimeter cluster barycenter. Two sets of requirements are used to complete electron reconstruction, a loose requirement with $|\eta_{cluster} - \eta_{truck}| < 0.05$, $-0.20 < \Delta\phi < 0.05$ and $-0.10 < \Delta\phi_{res} < 0.05$, where

$\Delta\phi_{res} = -q(\phi_{cluster} - \phi_{track})$ and q is the electric charge sign. A tight requirement can also be used where $-0.10 < \Delta\phi < 0.05$.

Track candidates with no hits in pixel detector and with possibility to be matched to a secondary vertex are considered as photon candidates rather than an electron. The use of the E/p of the candidate, p_T, hits in pixel detector, secondary vertex information is crucial to decide whether the candidate is an electron or a potential photon candidate.

A window size in $(\eta \times \phi)$ plane of 3×7 built around the seed cluster in the barrel region ($|\eta| < 1.37$), and of 5×5 in the EndCap region of $1.52 < |\eta| < 2.47$ is used for cluster reconstruction. The cluster energy calibration is conducted based on data and simulated samples to correspond to the original energy of the electron [66]. Then this calibrated energy is used to evaluate the photon energy. Figure 18 shows the electron reconstruction efficiency.

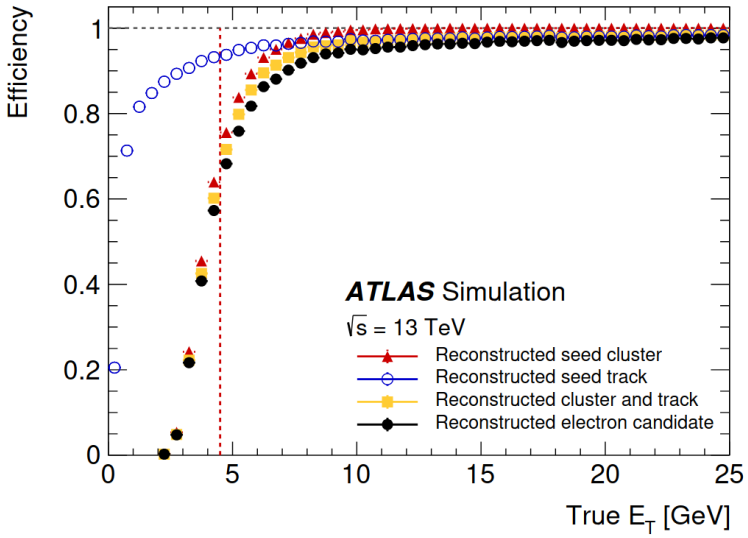

Figure 18: Electron reconstruction efficiency for simulated samples as function of the truth energy [62].

3.3 Photons

Like electrons, photons are reconstructed using combined information from the ID and the EM calorimeter (see Figure 17). Based on this information, photons are categorized as unconverted or converted photons; that transform into a pair of electron-positron before reaching the calorimeter. It can also be categorized as prompt or fake; where the hard scattering process or the fragmentation of a parton produce prompt photons, and a reconstructed photon originating from a different source is deemed a fake.

The calorimeter seed finding and track finding are similar for the electron and photon. The size of the cluster in the barrel changes from (3×5) to (3×7) based on if the photon is respectively unconverted or converted one, while it is the same (5×5) in EndCap region. In order to define the converted photons, a conversion finding algorithm is employed and applied to tracks matching loosely the cluster. Clusters that match a conversion vertex are

considered as converted photons, and they make about 20% of photons in the ID at low η. While clusters that do not match the electron or the conversion vertex are considered as unconverted photon, and they make about 65% of photon in the ID at $|\eta| \approx 2.3$ [67]. TRT track's criteria were strengthened in order to limit the percentage of unconverted photons reconstructed as double or single track TRT conversions. TRT tracks must have at least 30% precision hits, defined as a distance from track to wire that is within 2.5 times its uncertainty.

Similarly to electrons, the photon energy is computed using the reconstructed cluster energy, then calibrated with correction applied to account for the energy loss in the material upstream of the detector. A multivariate regression approach based on the features of the shower development in the EM calorimeter is used to optimize the energy resolution of the electron or photon [68].

The presence of non-prompt photons, primarily from hadron decays in jets and hadrons that imitate photon energy depositions showering early in the EM calorimeter, makes it challenging for the identification of the photon. Shower shape and isolation variables are used for photon identification as well. They are considered separately for converted (photons which convert into an electron-positron pair before reaching the calorimeter) and unconverted photons, which leave different electromagnetic signatures. The efficiency of the photon identification in data ranges from 0.5% to 5% based on photon p_T and η.

3.4 Muons

Muons reconstruction exploits information from both the ID and MS, and additionally from the calorimeter, to account for energy loss in the EM and hadronic regions. Tracks from the MS are used for the ID tracks tagging as muon candidates. Hits in the MS stations are the starting point for muon reconstruction which, combined, looks like a straight line local track. Primarily, these segments in the three stations are loosely joint using parabolic trajectory steaming from the interacting point. Then a Global χ^2 fit is applied to perform precise trajectory measurements accounting for energy losses in the detector material.

Different five muon types can be defined based on the reconstruction methodology carried out (see Figure 19). Combined muons (CM) are obtained by applying a fit combining hits from MS and ID, and also accounting the energy losses in the calorimeter. Inside-out combined (IO) result from extrapolation of ID tracks to the MS ones with a condition of having at least three hits loosely aligned in the MS. A combined fit matching the ID track to the MS ones is performed taking into account the energy deposit in the calorimeter. Muon-spectrometer extrapolated (ME) called also Standalone muon, consist of only MS track extrapolated to the interacting point, and which don't match any ID track. This is used to benefit from a large acceptance up to ($|\eta| = 2.7$). Segment-tagged (ST) consist of a fitted track with tight angular matching of a MS segment. ID track fit is used to define the muon candidate parameters. Calorimeter-tagged (CT) muons are built using an ID track extrapolated to an energy deposit in the calorimeter [70].

After reconstruction and based on the defined parameters of the muon candidates i,e: the number of hits in the different ID subsystems and MS stations and track fit properties; additional requirements are used to select high quality muons that will be used for physics analysis. This set of requirements are known as the working points.

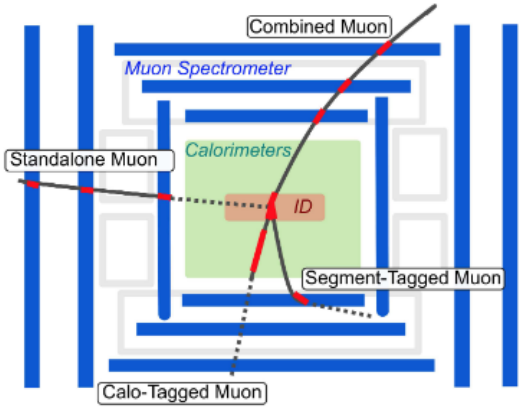

Figure 19: The five types of reconstructed muons in ATLAS detector [69].

3.5 Jets

A jet describes a stream of particles resulting from the hadronization of an initial quark or gluon, produced during proton-proton collisions. Given the phenomenon of confinement in QCD, color-charged particles can't exist freely. These hadrons form highly collimated jets, that are an important ingredient in the physics analyses shown in this thesis. Jets arise from a complex series of interactions that happen in the rgion between the physics of interest at the interaction point and the observed physics at the detector, which can start with initial and final state radiation, or heavy particles decaying hadronically. Therefore, there is an inherent element of ambiguity when associating specific physics processes to jets, and there is no reliable one-to-one correspondence between parton and jet kinematics. Particles in a jet, carrying about 60% of the total energy of the jet, leave tracks in the ID if they are charged and leave energy deposits inside calorimeters even for uncharged particles. Photons contained within the jet contain about 30% of the jet's energy, and shower in the LAr electromagnetic calorimeter. The energy deposited in the EM calorimeters is produced only from electromagnetic processes, while in the case of the hadronic calorimeter, this results from the ionisation processes originating from the hadronic showers and by excitations of molecules in the scintillators. Different algorithms can be deployed to reconstruct a four-momentum which would be related to the particle that initiated the shower and lead to the jet formation. Jet-finding algorithms are used by ATLAS for the jet identification. The most basic jet-finding algorithm might identify the core with high energy, construct a cone with a predetermined radius around the core, collect all energy deposits inside the cone, and then sum them to obtain the energy of the reconstructed jet. Reliable jet-finding algorithms must consider the behavior of jet algorithms carefully; choices at the jet building stage propagate backwards to the event reconstruction. An infrared and collinear safe clustering algorithm widely used in particle physics. Infrared safety refers to the independence of jet definitions under the inclusion of jet soft radiation, while collinear safe algorithms have the property of reliably including a split parton (a gluon parallel to its own direction) within a given jet. This is because theoretical calculations that consider these scenarios diverge and produce infinities, which are not observable, so a jet algorithm should not be sensitive to whether they manifest.

This prevents the number of identified jets from altering as a result of splitting or merging of the high transverse momentum particles, or as a result of soft gluon emission between jets [71].

Energy depositions in topological clusters [64] are amassed together into Topo-clusters associated with particle showers [72], which can define calorimeter-only jets (EMTopo jets). Topo-clustering diminishes noise that can be associated with the simple summing of all energy deposits in a cone. Then, the energy measurement is corrected using information from the tracker. Including tracker information at the stage of jet-finding intends to identify individual particles within the jet (PFlow jets). This method enhance the precision of the measurement of charged hadrons and improves the transverse momentum resolution of low-p_T jets [73]. The inspiration for this 'particle flow' (PFlow) method comes from the ALEPH experiment at LEP, which is the earliest to use successfully the technique of 'energy flow'. The main consideration for using PFlow jets, instead of those based on calorimeter information alone, is an improved performance in higher pile-up environments. A detailed description of the jet calibration procedure can be found in [74]. Jets with $|\eta| < 2.5$ containing b-hadrons are identified using a b-tagging algorithm [75].

3.6 Jet Vertex Tagging

At large average number of interactions per bunch crossing, local fluctuations may lead to the reconstruction of spurious low-p_T pileup jets. The jet-vertex-fraction (JVF) [76] variable was developed with the aim to reduce such contributions. JVF is defined as the scalar sum of the transverse momenta of tracks belonging to the HS vertex and associated to a jet, divided by the same quantity, evaluated over all the interaction vertices reconstructed in the collision. This quantity though is not stable as a function of N-PV, as the denominator increases. Therefore, a corrected version of JVF is introduced [76] to scale by N-PV the sum of the p_T of tracks associated with a jet but not with the HS vertex.

The JVT discriminant is constructed as 2-dimentional likelihood using the ratio (R_{pT}) of the sum of p_T of the tracks associated to the jet and originating from the hard-scatter vertex to the p_T of the fully calibrated jet, as well as a corrected version of the JVF (corrJVF) for the linear increase of p_T of tracks associated to pileup interaction with the total number of pileup tracks per event, by dividing the pileup p_T by the number of pileup tracks [76]. Unlike JVF, JVT combines both calorimeter and tracking information, and it is bound between 0 and 1, but a value of -1 is assigned to jets with no associated tracks. The JVT likelihood distribution, as a function of the two aforementioned variables, is shown in Figure 20. The hard-scatter identification efficiency is shown in Figure 21 as a function of average number of interaction per bunch crossing, as obtained from MC multi-jet events. One can observe how the efficiency for JVT is almost flat as a function of pileup, while it decreases for JVF. The implementation of JVT leads to improved pileup jet rejection, as $< \mu >= 33.7$ in the run–2 data set. The efficiency is measured in Z+jets events and scale factors are derived to take into account potential mismodelling in the simulation as described in [76].

For many physics analyses, jets in the forward region are more essential and suppression of pileup there is crucial. forward-Jet-Vertex-Tagger (fJVT) is the forward pileup tagging technique used to reject pileup in the forward region of the detector [77]. It exploits the

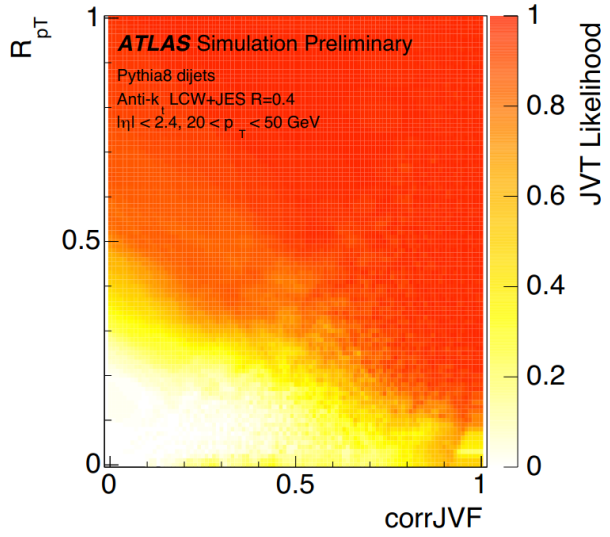

Figure 20: JVT likelihood function shown in the (JVF, R_{pT}) plane using simulated multi-jet events [76].

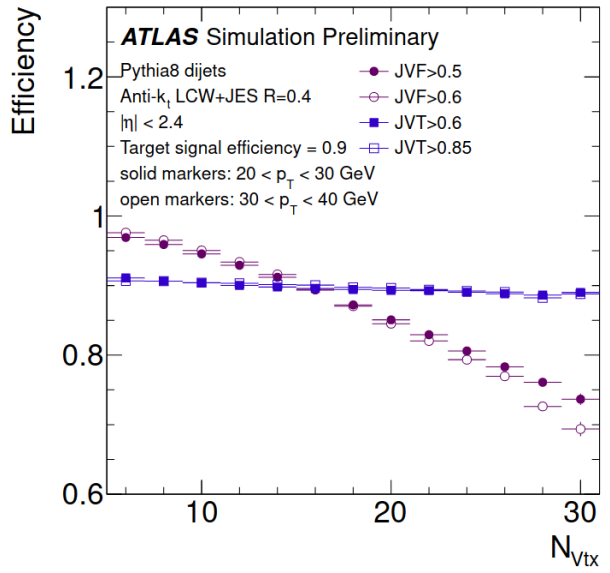

Figure 21: Dependence of the hard-scatter efficiency as a function of actual interaction per bunch crossing for JVF and JVT for different requirements on the discriminant variables using simulated multi-jet events [76].

correlation between central and forward jets originating from pileup interactions, where forward pileup jets that are back-to-back to central pileup jets are indirectly tagged and rejected using tracking and vertex information in the central region.

3.7 Taus

Taus are unique among leptons in that they are the only ones heavy enough to decay into hadrons. The reconstruction of these hadronic decays can be done through two possibilities, using tracks or jets. Tracks are required to have at least two hits in the pixel detector and IBL, and 7 hits in total when including the SCT. They need to have $p_T > 1$ GeV and to be enclosed in the cone region of $\Delta R < 0.2$. The second type of seeds is jets reconstructed using topoclusters with energy $E_T > 10$ GeV in the region of $|\eta| < 2.5$, while taus candidates from $1.37 < |\eta| < 1.52$ region are thrown [78, 79]. Then Topojets are matched to seed tracks if they are present in the event, and the tau candidate is considered to have two valid seeds. In the case of $Z \to \tau\tau$ events, taus candidates with only topojet seeds account for 25% of the reconstructed events, and 5% for candidates with only track seeds, while 70% have both the two possible seeds.

The candidate track vertex with the largest proportion of momentum from tracks related to the jet ($\Delta R < 0.2$) is considered as the tau vertex [76]. The shortest distance between the track and the tau vertex must be $d_0 < 1.0$ mm in the transverse plane, and $\Delta z_0\ sin(\theta) < 1.5$ mm in the longitudinal plane, are added as additional requirements on the tracks.

Tau energy calibration using Monte Carlo samples is necessary to apply the needed corrections to energy evaluated by calorimeters. Two mains calibrations are conducted, the baseline, and the boosted regression tree (BRT) calibration [79].

Chapter 4:

Muon overlap with jets and E_T^{miss} performance study

In the LHC proton-proton collisions, interacting particles associated to Hard Scattering (HS) are quarks and gluons, which have momentum depends on the corresponding parton densities and known to be intrinsically random. The conservation laws require momentum of the two proton system to be conserved, resulting in a zero transverse momentum. As a result, also the transverse momenta of the collision products must sum up to zero. Hence, non-zero measured transverse momentum hints to undetected particles. Non-zero missing transverse energy (E_T^{miss}) suggests the possible production of particles that interact weakly with the detector. For these undetected particles, E_T^{miss} serves as an experimental proxy to estimate their transverse momentum. The reconstruction is challenging as it involves all detector subsystems for the precise reconstruction of all detectable particles of the hard interaction of interest. The measurement of E_T^{miss} in the detector is an important component for physics analyses, which quantify the imbalance of the total transverse momentum after the collision. Particles that escaped the detector without any interaction are the origin of the imbalance. The undetected particles in the Standard Model are neutrinos, while other models include different new particles beyond the SM that escape the ATLAS detector without being detected easily, and they could be a source of missing transverse energy. The E_T^{miss} is evaluated based on the measured calibrated objects. The x and y components of the E_T^{miss} are calculated using the magnitude along the x and y axes of the various contributions:

$$E_{x(y)}^{miss} = E_{x(y)}^{miss,\mu} + E_{x(y)}^{miss,e} + E_{x(y)}^{miss,\gamma} + E_{x(y)}^{miss,\tau} + E_{x(y)}^{miss,jet} + E_{x(y)}^{miss,soft} \tag{61}$$

Each term of this equation corresponds to a negative vectorial sum of transverse momenta of both energy deposits and tracks. Energy deposits and tracks are matched to physics objects, which are all reconstructed and calibrated. The priority order is the following: muons, electrons, photons, hadronically decaying τ-leptons, jets (so-called hard term). In order to avoid the double-counting of detector signals, an ambiguity solving procedure is considered [80]. $E_{x(y)}^{miss,soft}$ (so-called soft term) represents all the signals not associated with any of the previous objects:

$$E_{x(y)}^{miss} = -\sum_{i\in \text{ hard objects}} p_{x(y),i} - \sum_{j\in \text{ soft signal}} p_{x(y),j} \tag{62}$$

Then it is easy to construct other widely used variables based on Equation 62:

$$E_T^{miss} = |\vec{E}_T^{miss}| = \sqrt{(E_x^{miss})^2 + (E_y^{miss})^2} \qquad \phi^{miss} = \tan^{-1}(\frac{E_y^{miss}}{E_x^{miss}}) \tag{63}$$

The E_T^{miss} has a non-negative value by definition. ϕ^{miss} is the azimuthal angle that represents the direction. The E_T^{miss} is determined in both the trigger and the offline computation.

The soft term can be evaluated considering ID tracks or topo-clusters in the calorimeters. ATLAS considers a track soft term (TST) that is insensitive to pileup, because only tracks associated to the HS vertex are used. However, TST does not take into account the presence of neutral particles.

4.1 E_T^{miss} soft term

The soft term is an essential but challenging component of E_T^{miss}. It is built of all detector signals not matched to the reconstructed objects in the hard term. Contributions from the hard term and pileup can taint the soft term construction. Different algorithms have been designed in the past for the E_T^{miss} reconstruction based on the type of the jets deployed [81, 82]. The definition used here is the track-based soft term (TST), which includes tracks not associated to hard objects.

For EMTopo E_T^{miss}, the longitudinal and transverse impact parameters z_0 and d_0 determined with respect to the hard scatter vertex position are used to associate tracks with the hard scatter vertex. The following criteria eliminate neutral contributions and the out-time pileup signals to offer excellent track-to-vertex matching [83]:

- $p_T > 0.4$ GeV,
- $|\eta| < 2.5$ (ID coverage),
- $|\frac{d_0}{\sigma(d_0)}| < 2$,
- $|z_0 \sin\theta| < 3.0$ mm.

While tracks with the following criteria are removed from the soft term to avoid double counting of the same particle and mismeasured tracks [83]:

- Tracks found in the proximity of the electron or the photon: $\Delta\eta < 0.2$ and $\Delta\phi < 0.05$
- Tracks found within the cone of a hadronically decaying tau lepton of a size: $\Delta R = 0.2$
- ID tracks associated to an identified muon.
- Tracks associated to jets using the ghost association technique [84].

- Isolated tracks with $p_T > 120$ GeV and $p_T > 200$ GeV with $|\eta| < 1.5$; p_T relative resolution larger than 40%.

For PFlow E_T^{miss}, tracks associated with charged PFlow particles that are not related with any well-identified reconstructed object and which withstand the track-to-vertex association, are included to the soft term. The requirements are identical to those utilized in the EMTopo-based approach. The few changes are related to the PFLow algorithm's track quality consideration, as well as the different tracks to vertex association. The different requirements are as follows [83]:

- $p_T > 0.5$ GeV,
- $|\eta| < 2.5$ (ID coverage),
- $|z_0 \sin\theta| < 2.8$

With no requirement on the transverse track parameter d_0 for PFlow-TST to prevent biases on displaced jets.

4.2 E_T^{miss} working points

Additionally, E_T^{miss} definitions are given based on the selection of jets used in the reconstruction, in order to provide different working points for physics analyses with different needs. The "Loose" working point, uses jets that have $p_T > 20$ GeV with the JVT selection if the jet has $p_T < 60$ GeV and lies in the region of $|\eta| < 2.4$ [83].

The "Tight" working point is defined to suppress pileup contribution. The jets in the forward region with $|\eta| > 2.4$ and $20 < p_T < 30$ GeV are removed, because it is the region of phase space with more pileup. However, the risk of loosing hard jets degrades the scale of the reconstructed E_T^{miss}. In low pileup conditions, the resulting resolution is worse with large fraction of hard scatter jets removed. The method gives better E_T^{miss} resolution in high pileup conditions [83].

The "Forward-JVT" E_T^{miss} working point is evaluated to suppress tails in the E_T^{miss} distribution. The E_T^{miss} in this working point includes jets with $p_T > 20$ GeV; calculated without including jets in forward region of $|\eta| > 2.5$, $20 < p_T < 50$ GeV and failing the "Loose" fJVT cut [77].

4.3 Systematic uncertainties

For any analysis using E_T^{miss}, it is necessary to be able to evaluate the systematic uncertainty on the E_T^{miss} scale. The E_T^{miss}, as defined in this chapter, is the sum of several terms corresponding to different types of reconstructed objects. The missing transverse energy uncertainty is evaluated using systematics associated to each object that enter the E_T^{miss} reconstruction. Systematic uncertainties of each reconstructed object are propagated to the E_T^{miss} for hard term uncertainty. While a specific uncertainty is assessed for the soft term. The soft term $E_T^{miss,soft}$ is expected to balance the hard term momentum $E_T^{miss,hard}$ in $Z \to \mu\mu$ events topology known to have no real E_T^{miss}. Unfortunately, this balance is spoiled

by effects related to detector resolution. Three different quantities illustrating the soft term $E_T^{miss,soft}$ projection along the hard term $E_T^{miss,hard}$ are used to study the modeling of the soft term [83].

- The parallel scale Δ_L , that represents the mean value of the parallel component of the projection ($E_{T,||}^{miss,soft}$).
- The parallel resolution $\sigma_{||}$, that represents the root-mean-square RMS of the ($E_{T,||}^{miss,soft}$).
- The transverse resolution $\sigma_{\perp}$, that represent the root mean square RMS of the component of the projection ($E_{T,\perp}^{miss,soft}$).

The maximum discrepancy between the data and the different Monte Carlo generator plus parton shower models is used to calculate the systematic uncertainty. Differences between event topologies with large numbers of jets and those with no jets, are taken into account by a further splitting of the total systematic into jet-inclusive and jet-veto selections and merging them later as the maximal variation between the two cases.

The TST systematic is calculated similarly for the EMTopo and EMPFlow. Since the TST has similar definition, a good agreement is expected between the two systematic envelopes from the two jet collections [83].

Systematic uncertainties are dominated by jet energy scale (JES) and η-intercalibration uncertainties in 2015–2016 data of $Z \to \mu\mu$ events. At low E_T^{miss} the large JES systematic uncertainties can push a pileup jet above the JVT threshold requirements ($p_T < 60$ GeV and $|\eta| < 2.4$) which lead to include the pileup jet into the E_T^{miss} which can degrade the agreement between data and simulation at low E_T^{miss} [83].

Concerning the E_T^{miss} distribution comparison of the EMPFlow and EMTopo jet collections in $Z \to \mu\mu$ MC samples, the PFlow E_T^{miss} distribution is slightly narrower compared to EMTopo in case of inclusive jet selection. The difference gets more significant in the case the forward jets are removed ($|\eta| > 2.4$). Because the pileup rejection is better for PFlow jets, a slightly reduced distribution around 100 GeV is expected in this case. Finally, the 0-jet selection results in a distribution that is extremely comparable between EMTopo and PFlow E_T^{miss}. The tail is mostly affected by muon mismeasurement or jets misidentified as muon or electrons [83].

4.4 Electronic saturation

The bunch train in the high pileup of run-2 data (2016), is made up of eight filled and four empty bunches. At the end of a bunch crossing and the start of a new one, the electronic in the inner wheel of the electromagnetic calorimeter EndCaps, which cover the region $2.5 < \eta < 3.2$, remain saturated and recover only after the few bunch crossings. This phenomenon affect firstly the calorimeter energy of the first two crossings, which is observed to be low. The effect is small for jets and corrected for in electron calibration. Secondly, a large electronics noise is observed when the readouts electronics recover, which result in reconstruction of fake jets in small fraction of data. The presence of fake jets gives rise to spurious E_T^{miss} tail, which is suppressed by requiring the problematic clusters to have:

- $p_T^{EM} > 0.5$ GeV,
- $Q_{LAr} > 0.2$, the energy-squared weighted average of the liquid argon cells quality.
- Events with more than 20 of these clusters in $2.5 < \eta < 3.2$ are vetoed.

The effect is observed only in data, and the above cleaning is applied only for data not to simulation. The effect of this cleaning is measured for $Z \to \mu\mu$ samples; That shows no substantial bias when it comes to calorimeter issues; and found to be 98.34% [83].

4.5 Reconstruction of E_T^{miss} in ATLAS

Reconstructing the missing transverse energy (E_T^{miss}) for an event at ATLAS is characterized by two contributions: Firstly, using signals from hard physics objects that are composed of reconstructed muons, electrons, photons, τ-leptons and jets, while the second contribution comes from soft-event signals. The terms associated to the physics objects need to pass object selection criteria. Electrons are reconstructed from their shower shapes in ECAL calorimeter, and which are matched to ID tracks [85]. In order that electrons enter in the E_T^{miss} calculation, they must be identified in the range of $|\eta| < 2.47$, avoiding the transition region between the barrel and end-cap EM calorimeters, $1.37 < |\eta| < 1.52$. They are calibrated at the EM scale [86]. Electrons must satisfy the "Medium" likelihood and "Loose" isolation [85] with $p_T > 10$ GeV. The identification and reconstruction of photons are based on the electromagnetic showers in the calorimeters [87]. Photons are chosen and calibrated using the "Tight" selection criteria discussed in [88]. Photons with $p_T > 25$ GeV, $|\eta| < 1.37$ or $1.52 < |\eta| < 2.37$ are used. Hadronically decaying τ leptons with $|\eta| < 1.37$ or $1.52 < |\eta| < 2.47$ are considered. τ-leptons should satisfy the "Medium" quality selection given in [89]. In addition, τ-lepton that does not verify these criteria could contribute to E_T^{miss}, instead of if it satisfies the jet selection criteria. Muons candidates are reconstructed within $|\eta| < 2.5$ using an association of MS and ID tracks. Outside of the ID area coverage, muons are identified in the region of $2.5 < |\eta| < 2.7$ from a track fit to MS track segments alone. Medium muons with $p_T > 10$ GeV in $|\eta| < 2.5$ contribute to the E_T^{miss} terms. Jets are reconstructed using the anti-kt algorithm with radius R = 0.4 including electromagnetic, jet energy scale and pile-up corrections. The $E_T^{miss,soft}$ term is constructed from tracks that have $p_T > 400$ MeV and $|\eta| < 2.5$ and additional fit quality criteria. Vertices are constructed from at least two tracks passing selections on the transverse (longitudinal) impact parameter $|d_0| < 1.5$ mm ($|z_0 \sin\theta| < 1.5$ mm) relative to the vertex candidate [80]. The E_T^{miss} scale and resolution are calibrated using events from $Z \to \mu^+\mu^-$ samples, where no genuine E_T^{miss} source is present. For most calorimeters, the muon is a minimum ionizing particle (MIP) which leaves only a small fraction of its energy in the calorimeter (ranging from 100 MeV to 100 GeV) A di-muon decay is then the perfect, no genuine source of missing transverse momentum.

The two muons produced by the Z boson need to have an opposite electric charge due to the conservation of charge in the decay process. The leading muon is required to have a p_T greater than 25 GeV, while the requirement on the sub-leading muon is $p_T > 20$ GeV. The identification of muon is mainly achieved by applying quality requirements, which assess

how likely the object is a muon based on variables such as the χ^2 value of the fit and the p_T difference between ID and MS measurements. The isolation criterion requires the muon to be isolated from other objects, such as jets. Both muons are required to be a medium quality muon within $|\eta| < 2.5$ while passing isolation requirements [80]. From the two muons found in the events, one can construct the invariant mass of the Z-boson by using their four momenta.

The performance of the modelling in simulation of the E_T^{miss} magnitude calculation was tested in events with and without genuine E_T^{miss} is shown in Figure 22. In the left panel of

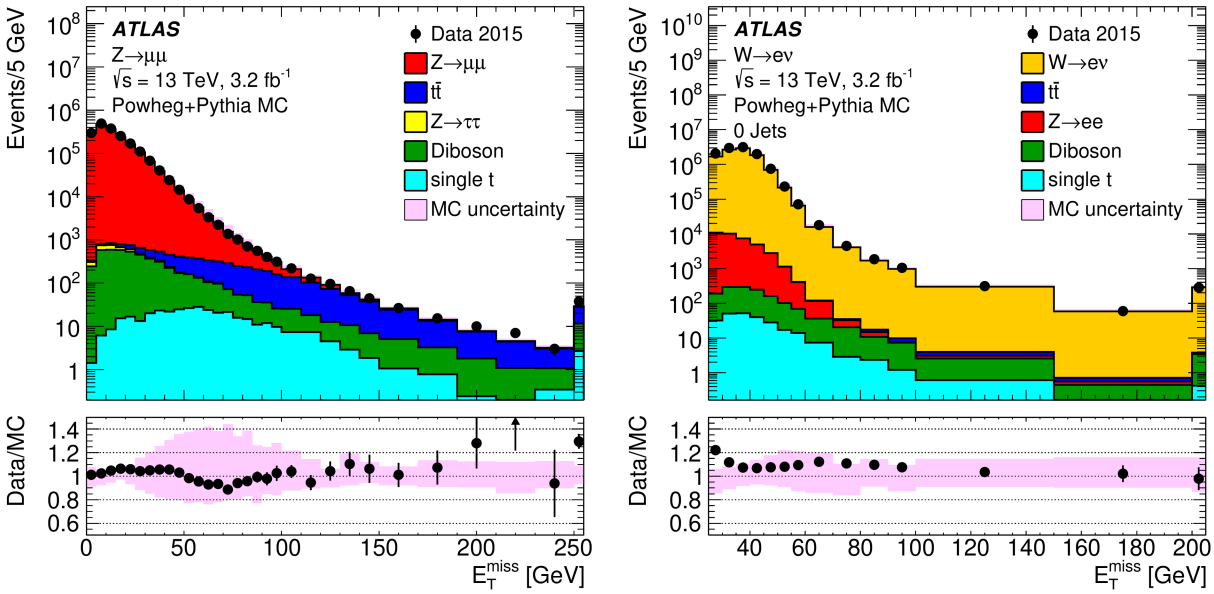

Figure 22: Comparison of the E_T^{miss} distribution in Z+jets events where no genuine E_T^{miss} is expected from the non-reconstruction of the neutrino (left), and comparison of the E_T^{miss} distribution in W +jets events, where genuine E_T^{miss} is expected from the non-reconstruction of the neutrino (right) [80].

Figure 22 distributions of E_T^{miss} for an inclusive sample of Z($\rightarrow \mu\mu$) +jets events extracted from data and compared to MC simulations including all relevant backgrounds. Total uncertainty is indicated using the shaded areas for MC simulations, including the systematic uncertainties from the p_T scale and resolution which are contributed by muons, jets, and the soft term, combined with the overall statistical uncertainty. Below the distributions, the corresponding data to MC simulations ratios are displayed, with the overall MC simulation uncertainties indicated by shaded areas. Distributions of E_T^{miss} reconstructed in N-jet =0 events with $W \rightarrow e\nu$ in data collected in 2015 and compared to MC is displayed as well in Figure 22. Events like $W \rightarrow e\nu$ provide a well-defined topology with neutrinos produced in the hard-scatter process. The expectation from MC simulation includes all relevant background final states passing the event selection, and is superimposed. The inclusive E_T^{miss} distribution from MC simulations contains a small contribution from multijet final states at low E_T^{miss}, which is absent for the N-jet=0 selection. The shaded areas display the total uncertainty for MC simulations, including the overall statistical uncertainty combined with systematic

uncertainties comprising contributions from the electron, jet, and the soft term. To reduce the dependence of the comparison on the MC generators adopted, each process is normalized to the generator cross-section, and the overall distribution is scaled to the same integral of data. A good agreement is observed in di-muon events, with data compatible with MC within uncertainties. The mis-modelling observed at low E_T^{miss} in W +jets events is due to the fact that the contribution from multijet events were not taken into account in simulation.

4.6 E_T^{miss} performance

The performance of E_T^{miss} has been studied using $Z \to \ell\ell$ events which has relatively large cross-section and represents a clean event signature because of the absence of genuine E_T^{miss}. In each event topology with $Z \to \ell\ell$ decays, one can define an axis in the transverse plane such that the component of E_T^{miss} along this axis is sensitive to detector resolution and biases. The projection of the vector E_T^{miss} onto the reconstructed flight direction of the Z boson (A_Z) is built. The direction of A_Z thus reconstructs the direction of motion of the Z boson. The perpendicular axis in the transverse plane (AA_Z), is a unit vector placed at right angles to A_Z, with a positive direction anticlockwise from the direction of the Z boson. The mean value of the projection of E_T^{miss} onto the longitudinal axis, $< E_T^{miss}.A_Z >$, is a measure of the E_T^{miss} scale, as this axis is sensitive to the balance between leptons and the hadronic recoil. In events without jets, the expected value of such quantity is 0. Values below 0 are expected if the hadronic recoiling activity is underestimated. The left panel of Figure 23 shows the value of $< E_T^{miss}.A_Z >$ as a function of p_Z^T. These mean values are used as a diagnostic to validate the E_T^{miss} reconstruction algorithms. If the leptons perfectly balanced the hadronic

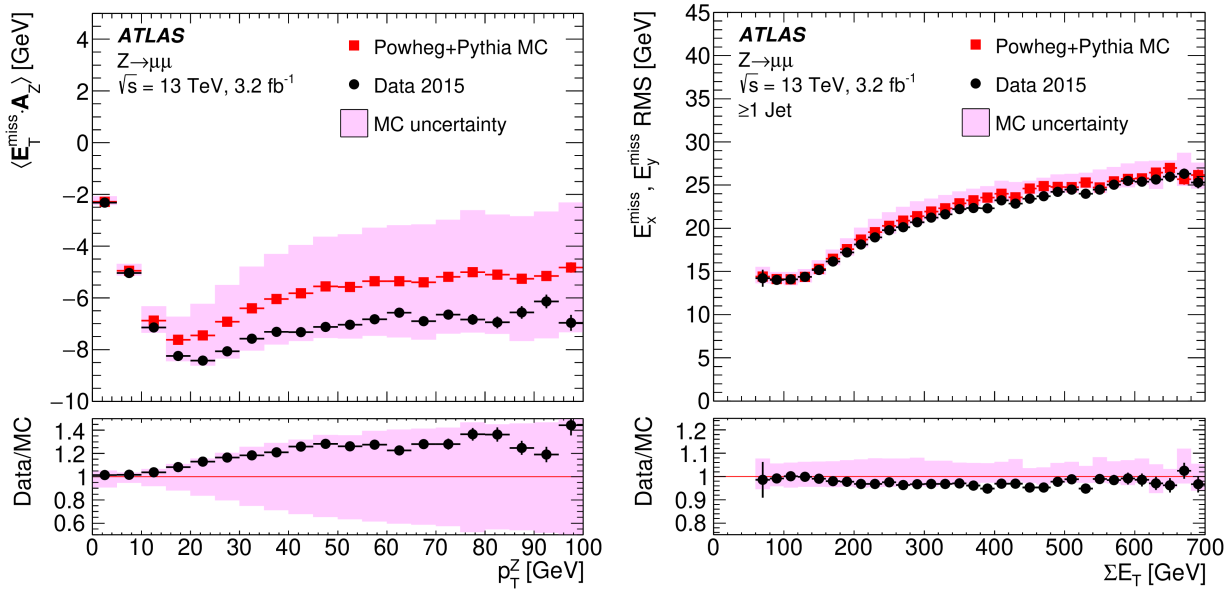

Figure 23: Comparison of the average projection of E_T^{miss} on the flight direction of the Z boson in $Z \to \mu\mu$+ jets events (left), and the resolution on the measurement of E_T^{miss} ($E_{(x)}^{miss}$, $E_{(x)}^{miss}$) components as measured in data and obtained in MC simulation in $Z \to \mu\mu$+ jets events (right) [80].

recoil, regardless of the net momentum of the lepton system, then that $< E_T^{miss}.A_Z >$ would be zero, independent of p_Z^T. Instead, $< E_T^{miss}.A_Z >$ displays a small bias which is reasonably reproduced by the MC simulation. At low values, the missing neutral component in the soft term leads to an underestimation of the hadronic recoil activity. At higher p_T, the jet term in the E_T^{miss} definition tends to dominate, and a flat offset is observed. Data and MC simulation are found to be in good agreement within uncertainties.

A more quantitative evaluation of the E_T^{miss} performance can be obtained from studying the ($E_{(x)}^{miss}$, $E_{(y)}^{miss}$) resolutions as a function of $\sum E_T$. The resolution is estimated from the RMS of the combined distribution of $E_{(x)}^{miss}$ and $E_{(y)}^{miss}$ in bins of $\sum E_T$. This can be measured in data selecting Z($\rightarrow \mu\mu$) events, where E_T^{miss} is expected to be zero. The right pannel of Figure 23 illustrates the RMS of the $E_{(x)}^{miss}$ and $E_{(y)}^{miss}$ components of E_T^{miss} as a function of the scalar sum of transverse energies of all objects reconstructed in $Z \rightarrow \mu\mu$ events, defined as $\sum E_T$. As can be seen, at low values of $\sum E_T$ the resolution is dominated by the measurement of the two muons, while the logarithmic behavior above $\approx$ 180 GeV is related to the Jet Energy Resolution.

4.7 Overlap removal of Physics objects

Physic objects considered in the calculation of E_T^{miss} should be reconstructed from exclusive signals deposed in different detector sub-systems to avoid double counting of the same signal. Hence, the energy deposits in the detector should be precisely associated to the jets or particles that produced them. To drop the possibility of double-counting of a reconstructed object, the energy deposit of particles in the detector material must be appropriately labeled to physics objects. After objects reconstruction, ATLAS uses an overlap removal process to eliminate conflict in cases where the same item is reconstructed as two or more objects. i.e: if a muon and an electron share the same ID track, the muon is kept, a tau candidate is kept if a jet is reconstructed as a tau lepton, also the electron is kept if a baseline electron and a baseline jet are located within a limited ΔR, unless if the jet is b-tagged the electron is discarded while the jet is kept.

Objects entering the E_T^{miss} reconstruction are divided into types, the highest and lower priority signature. Electron and muon are considered of the first types, while photons, tau and jets are a lower priority objects.

Overlap can also happen when electrons, photons, or taus are in close proximity to a jet. In this case, the overlap is removed using a parameter dubbed $f_{overlap}$(see Equation 64) that determines if the signal is from a real jet or a phony one. The parameter is derived as the ratio of EM energy deposit created by electron, photon, or tau to jet EM energy [83].

$$f_{overlap} = \frac{E_{e(\gamma,\tau)}^{EM}}{E_{jet}^{EM}} \tag{64}$$

However, this represents an issue, in case where the two objects are real, not fake and produced in proximity, which result in more long tail in E_T^{miss} distribution. An additional discriminating parameter is introduced to improve the missing transverse energy measurements

by suppressing the number of real jets labeled as fake ones. It is dubbed $\Delta p_T^{EM,e(\gamma,\tau),jet}$ and defined as follows [83]:

$$\Delta p_T^{EM\ e(\gamma,\tau),jet} = p_T^{EMjet} - p_T^{EMe(\gamma,\tau)} \tag{65}$$

The selection criteria for $\Delta p_T^{EM\ e(\gamma,\tau),jet}$ and $f_{overlap}$ are optimized based on data and MC samples for $Z \to \ell\ell$ event topology. The jet is considered as real signature and added to the jet term during E_T^{miss} reconstruction in Equation 61, if it satisfies $f_{overlap} < 1.0$ and $\Delta p_T^{EM\ e(\gamma,\tau),jet} > 20$ GeV [83]. These selections reduce significantly the tail in missing transverse energy distribution above 200 GeV by about 30% in the case of $Z \to ee$ events [83].

4.8 Muon overlap with jets

Jets that overlap with a reconstructed muon affect the E_T^{miss} reconstruction in such a way, its impact depends on the reconstructed jet origin. An overlap removal procedure is applied to nearby objects to make certain that a single signal does not result in two separate objects, which can causes a fake tail in the distribution and limit the E_T^{miss} resolution.

4.8.1 Muon-jet overlap origins

Pileup jets have significant impact on missing transverse energy calculations. Their contribution in jet term of reconstructed E_T^{miss} is efficiently suppressed through the JVT and fJVT discriminants (discussed in Section 3.6), that retain only hard scatter jets and reject pileup ones. However, a pileup jet can survive the JVT selection and enter the hard term, because of a mis-tag of a jet, produced when the p_T of the muon ID track represents a large proportion of the total jet p_T. Considering the pileup jet as a hard object affects mainly the tail distribution, degrading the E_T^{miss} response and resolution, due to the stochastic nature of the contribution.

The overlap between a muon and a jet can occur also when a muon expresses a significant energy loss in the calorimeter reconstructed as hard scatter jet from the primary vertex. The ID track from muon is found in the vicinity of the jet. This ambiguity lead to inclusion of the jet into the hard term, resulting in a double counting of the same muon signature, as this part of muon energy had been previously accounted for during the calibration stage.

In addition, Final State Radiation (FSR) of the final state muon can erroneous the missing transverse energy measurement. Hard photons emitted by muons can be energetic (up to tens of GeV) and well separated from the leptons (by more than a radian). They are not reconstructed as photons, because of the existence of the muon ID track in the proximity of the triggered cells of the calorimeter by the photon, which violate the isolation requirement. Due to a mismatch between the muon ID track momentum and the deposited energy measured in the calorimeter, they are also not reconstructed as electrons. The FSR photon signature in the detector is reconstructed as a jet with an associated ID track. The transverse momentum carried out by the FSR photon is not recovered during muon reconstruction, the jet representing this photon should be included in jets term of E_T^{miss} definition in Equation 61.

4.8.2 Muon-jet overlap suppression

Jets representing a significant energy loss in the calorimeter along the path of the muon and the ones from pileup, need to be rejected from the missing transverse energy reconstruction, through optimized selections on the following parameters:

- The fraction $p_T^{\mu-ID}/p_T^{jet-ID}$, Where the muon's ID track's transverse momentum $p_T^{\mu-ID}$ is a significant part of the jet transverse momentum p_T^{jet-ID} , which is the sum of the transverse momenta of all ID tracks emanating from the hard-scatter primary vertex associated with the jet.
- The fraction $p_T^{jet}/p_T^{\mu-ID}$, Where the jet's overall transverse momentum is not excessively large in comparison to the muon ID p_T.
- N_{track}^{PV}, There are a few tracks that are linked to the jet and originate from the hard scatter PV.

Jets are considered to be from FSR of the muon and need to be included into missing transverse energy reconstruction, using the following parameters:

- N_{tracks}^{PV}, A small number of tracks from the hard scatter primary vertex indicate that the jet has a small charged particle composition.
- $f_{EM} = E_{EM}^{jet}/E_{jet}$, The energy of the jet, as expected for a photon, is deposited in the electromagnetic calorimeter in large amounts.
- $p_T^{jet\ PS}$, The contribution of the large transverse momentum of the beam in the pre-sampler calorimeter layer (order of GeV) marks the initial starting point of the shower.
- w_{jet}, The jet is narrow, with a width similar to that of a dense electromagnetic shower; jet width is described as:

$$w_{jet} = \frac{\sum_i \Delta R_i p_{T,i}}{\sum_i p_{T,i}} \tag{66}$$

  where $\Delta R_i = \sqrt{(\Delta\eta_i)^2 + (\Delta\phi_i)^2}$ is Topocluster i's angular distance from the jet axis, and $p_{T,i}$ is the cluster's transverse momentum;
- $p_T^{jet-ID}/p_T^{\mu-ID}$, All ID tracks emanating from the hard-scatter primary vertex and associated with the jet have a transverse momentum that is close to ID p_T of the muon.

A scan was evaluated for these parameters to determine the values that provide the best performance of the missing transverse energy. The resulting E_T^{miss} performance distribution is shown in Figure 24 (left-hand plot) in $Z \to \mu\mu$ events using EMTopo jets. The fake E_T^{miss} is defined as the difference between the reconstructed E_T^{miss} and the truth E_T^{miss} in $Z \to \mu\mu$ events, and can be seen in Figure 24 (left-hand plot).

Table 3 represents the list of variables used to suppress the effect of jets that overlapped with muons using EMTop and PFLOW jet collections. The resulting values from the different scans conducted for each of them are listed as well. The E_T^{miss} mean and integral in the region ranging from 100 GeV to 1000 GeV were considered to decide on the scans that correspond to the best performance of the observable.

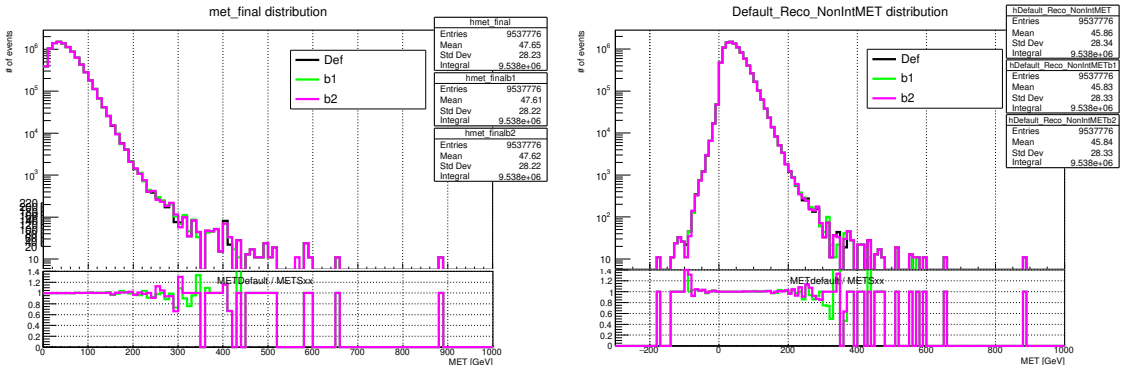

Figure 24: Comparison of the E_T^{miss} distribution performance (left-hand) and the fake E_T^{miss} distribution (right-hand) in $Z \to \mu\mu$ events for different values of the parameters used to suppress the muon-jet overlap.

Table 3: Resulting values of parameters corresponding to the best E_T^{miss} performance after suppressing jets from pileup, muon energy deposit in the calorimeter, and including the jets from FSR photons.

Scanned variables	EMTOPO jets	PFLOW jets
N_{tracks}^{PV} (muon energy loss)	3	8
N_{tracks}^{PV} (FSR)	6	2
w_{jet}	0.15	0.02
$p_T^{jet\ PS}$ (MeV)	2 10^3	12 10^3
f_{EM}	0.5	0.4
$p_T^{jet-ID}/p_T^{\mu-ID}$	0.95	0.7
$p_T^{jet}/p_T^{\mu-ID}$	0.5	1
$p_T^{jet-ID}/p_T^{\mu-ID}$	1.5	3

4.8.3 Dependence on pileup and correlation

In order to normalize the MC pileup conditions to those observed in experimental data, a pileup reweighing procedure was applied to weight the events in MC samples to match the distribution of the average number of interactions per bunch crossing (μ) to the one observed in data. Though, it is critical to determine whether pileup has an impact on the results. Figure 25 shows that the resulting missing transverse energy distribution corresponding to the best performance has no dependency on the average number of interactions per bunch crossing (μ) using EMTopo and PFLOW jet collections.

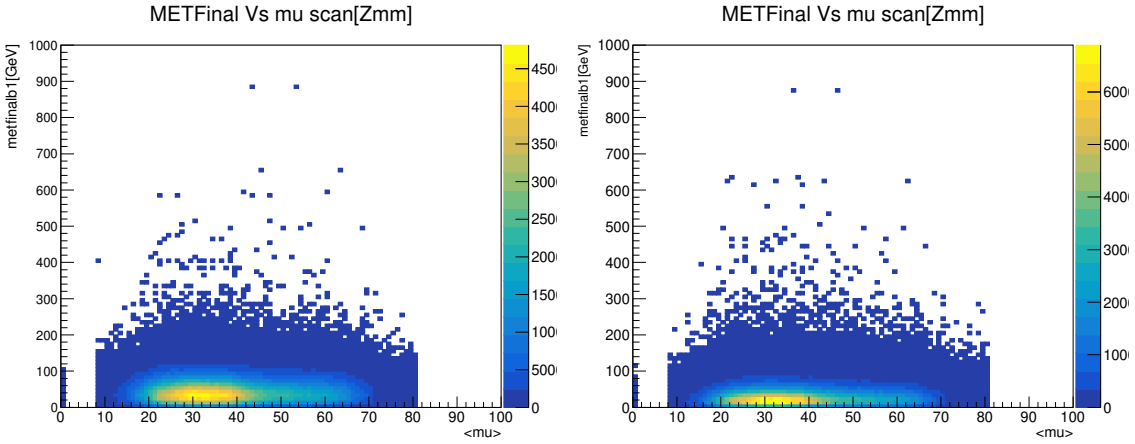

Figure 25: missing transverse energy versus the average number of interactions per bunch crossing (μ) for EMTopo (left-hand) and PFlow (right-hand) jets in $Z \rightarrow \mu\mu$ MC samples.

Furthermore, the correlation between the reconstructed E_T^{miss} using the best performance and the old one was evaluated for EMTopo and PFlow jet collection in $Z \rightarrow \mu\mu$ events. The results showed no correlation, as can be seen in Figure 26. No correlation found between this result (new tuning values) and default E_T^{miss}.

4.8.4 Results in $t\bar{t}$ events

Top quark is the heaviest particle in the standard model, and the only one decaying before hadronization. The high transverse momenta of the top quarks originating from p-p collisions give rise to a reach event topology. The $t\bar{t}$ samples are known to be a dense environment with real missing transverse energy, which make of them good candidates to check the performance of missing transverse energy. Events with $t\bar{t}$ in the final state allow the evaluation of the E_T^{miss} performance in interactions with a large jet multiplicity. Figure 27 shows the missing transverse energy performance for different scans.

The resulting performance of the missing transverse energy shows a consistent independence on the pileup conditions. The E_T^{miss} mean and integral in the region ranging from 100 GeV to 1000 GeV were evaluated for several intervals of the average number of interactions per bunch crossing ($< \mu >$), which are as follows: [0-20], [20-40], [40-60], and [60-80]. This study confirms the independence of the E_T^{miss} performance from pileup conditions, as can be seen in Table 4.

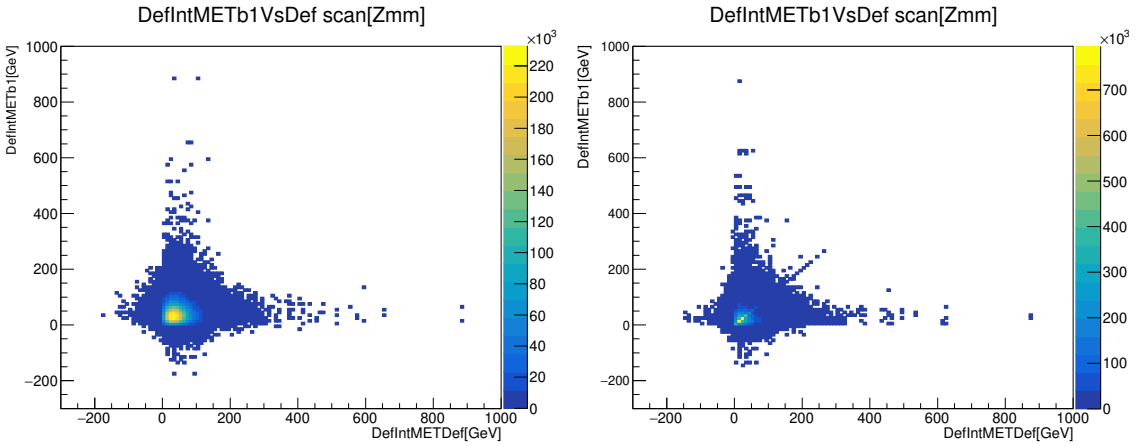

Figure 26: Reconstructed E_T^{miss} with the best performance versus truth E_T^{miss} for EMTopo (left-hand) and PFlow (right-hand) jet collections in $Z \rightarrow \mu\mu$ MC samples.

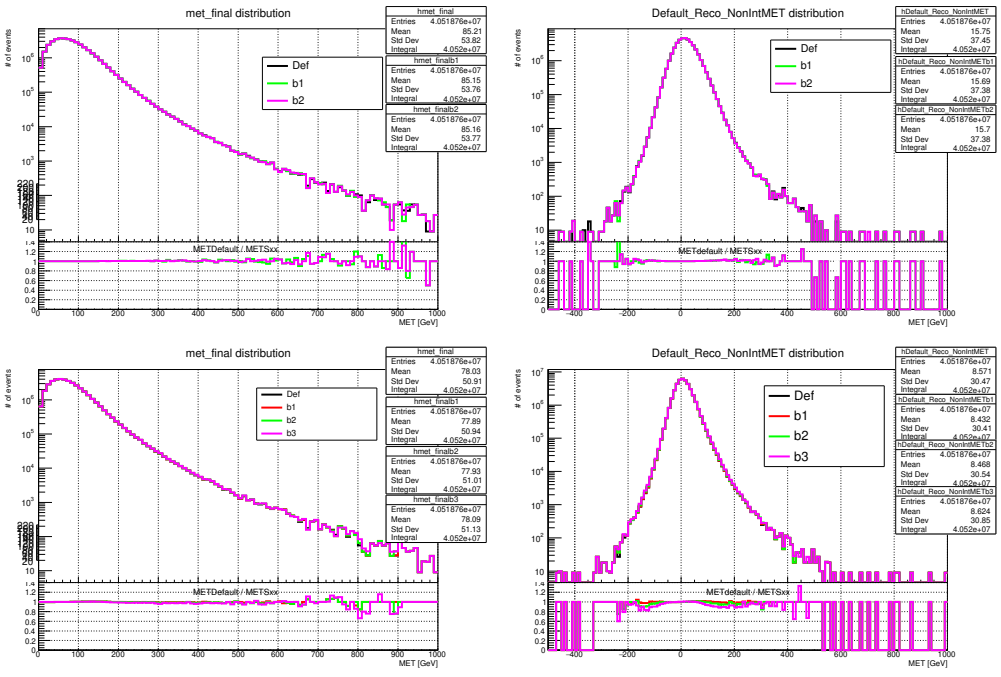

Figure 27: The reconstructed E_T^{miss} distribution (left-hand) and the fake E_T^{miss} distribution (right-hand) for EMTopo (top Plots) and PFlow (bottom Plots) jets collections in $t\bar{t}$ MC samples.

Table 4: Comparison of the obtained integral of the missing transverse energy tail in the region of [100 GeV,1000 GeV], for different intervals of the average number of interactions per bunch crossing ($< \mu >$).

μ	[0,20]	[20,40]	[40,60]	[60,80]
E_T^{miss} with the best performance	11281	37234	91414	151209
E_T^{miss} default performance	11387	37588	91839	151346

$t\bar{t}$ samples confirm that no abnormal statistical relationship between the missing transverse energy corresponding to parameters values in Table 3 and the default missing transverse energy. Figure 28 shows the correlation between the E_T^{miss} (fake E_T^{miss}) distribution, obtained after applying the scans in Table 3 and the default E_T^{miss} (fake E_T^{miss}) using EMTopo jets collection in $t\bar{t}$ events.

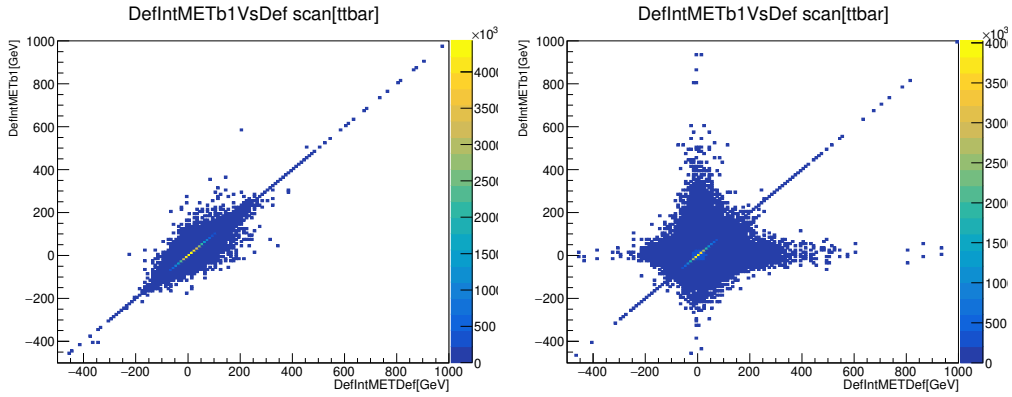

Figure 28: Reconstructed E_T^{miss} with the best performance versus default E_T^{miss} (left-hand) and fake E_T^{miss} with the best performance versus default fake E_T^{miss} (right-hand) for EMTopo jets collection in $t\bar{t}$ MC samples.

4.8.5 E_T^{miss} performance and validation.

The validation process has been evaluated using Bootstrap method. This method is a powerful and computer-based method for statistical inference without relying on too many assumptions. The aim of this study is to make inference about the mean and the integral of the missing transverse energy distribution for EMTopo and EMPFlow jets.

Bootstrap is a general and powerful tool introduced in 1979 by Bradley Efron for confidence intervals and assessment of uncertainty, suitable to control and check the stability of results [90]. It is a resampling method with replacement of the original sample which is, in this case, the missing transverse energy distribution. The first step consists of drawing bootstrap samples from the original one. Secondly, evaluating the statistics of E_T^{miss} for each bootstrap sample. Thirdly, construct from this bootstrap samples statistics; mean and integral in

this case; a sampling distribution and use it to make further statistical inference. Finally, estimating the standard error of statistic for the missing transverse energy. Additionally, the Confidence Interval can be defined. The standard error of the mean and integral are evaluated based on their standard deviation, which provide information on how much they deviate from the original values of parameters.

The number of repetitions must be sufficient to allow for accurate calculation of relevant statistics on the sample. In a perfect scenario, the sample of estimates would be as large as possible, taking into account the time consuming and computing resources used to produce hundreds of thousands of repetitions. Figure 29 shows the missing transverse energy mean and integral from bootstrap samples in the case of EMTopo and EMPFlow jets for $Z \to \mu\mu$ events. Table 5 summarizes the E_T^{miss} mean and integral resulting values, as well as their related standard errors. The improvements obtained based on the bootstrap method are shown along with the errors as well.

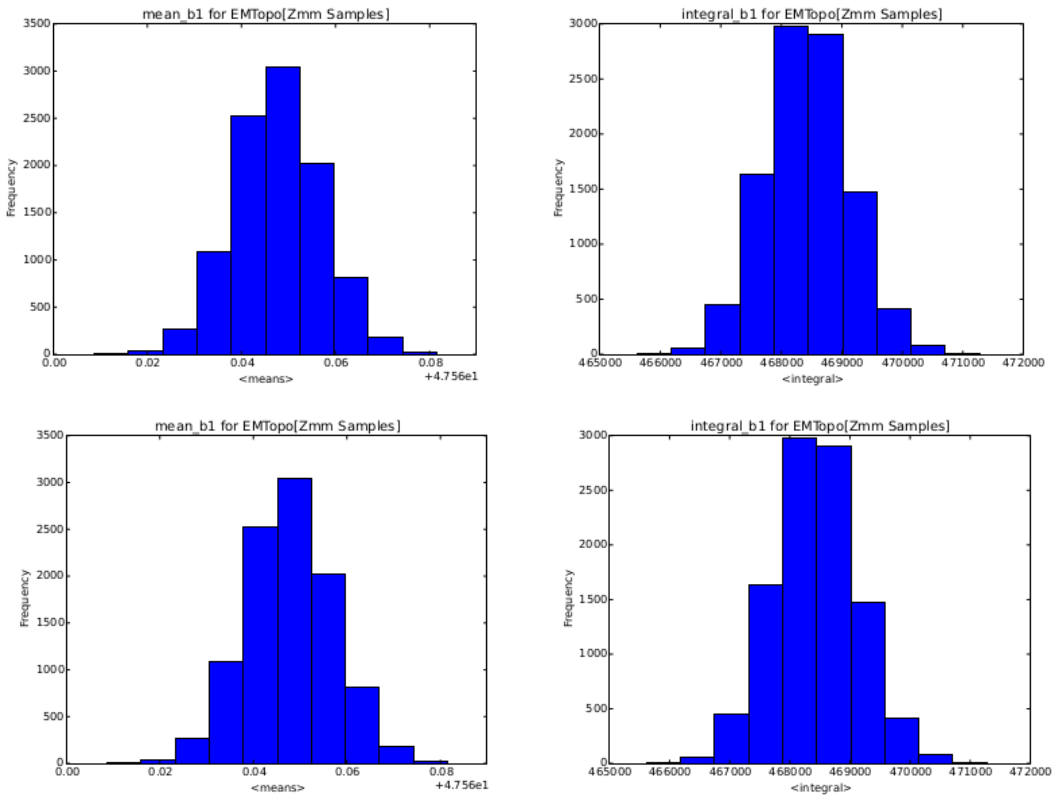

Figure 29: The obtained results of the E_T^{miss} mean distribution (left-hand) and the E_T^{miss} integral distribution (right-hand) using Bootstrap method for EMTopo (Top-Plots) and EMPFlow (Bottom-Plots) jets in $Z \to \mu\mu$ events.

4.9 Conclusion

The performance of the reconstructed missing transverse momentum in data collected from p-p collisions at the LHC are evaluated for selected event samples with genuine E_T^{miss} such

Table 5: Results of E_T^{miss} mean and integral along with their corresponding errors from bootstrap samples.

	E_T^{miss} performance	Mean	Integral
EMTopo	Best value	47.608 ± 0.009	468428.13 ± 689.06
	Default value	47.646 ± 0.009	470780.70± 694.70
	Improuvement (%)	0.08 ± 0.03	0.50 ± 0.20
EMPFlow	Best value	32.221 ± 0.007	130777.50 ± 357.96
	Default value	32.677 ± 0.007	139970.27 ± 369.70
	Improuvement (%)	1.4 ± 0.03	6.57 ± 0.33

as $W \to e\nu$ and $t\bar{t}$, and without genuine E_T^{miss} such as $Z \to \mu\mu$. The comparison of the data from the detector with the corresponding MC simulations generally yields good agreement in the covered phase space. The systematic uncertainty contribution from the soft event to the reconstructed E_T^{miss} is determined with $Z \to \mu\mu$ final states without jets. The parallel and perpendicular projections of the missing transverse momentum vector E_T^{miss} onto the vector sum of the transverse momenta of the hard objects $E_T^{miss,hard}$ have been used to compute the systematic uncertainty contamination from the data-to-MC-simulations comparison.

The parallel projections yield the uncertainty of the E_T^{miss} scale, estimated as a function of the total transverse momentum of the hard objects. The widths of the distributions of the parallel and perpendicular projections allow the respective systematic uncertainties of the E_T^{miss} resolution. Results show that simulation tends to underestimate the perpendicular resolution and overestimate the scale and parallel resolution, in each case differing from data by at most 10%.

The performance evaluation of E_T^{miss} obtained from the overlap removal study improves the E_T^{miss} integral value roughly 7.23% and 0.43% for PFlow and EMTopo jets collections, respectively. Whiles, the improvement on the E_T^{miss} average value is about 1.46% and 0.065% for PFlow and EMTopo jets collections, respectively, in $Z \to \mu\mu$ MC samples.

The results of the muon overlap with jet study has been validated in $t\bar{t}$ events. In addition, in $Z \to \mu\mu$ MC samples that have been produced using different generators such as Sherpa and Powheg. Furthermore, the powerful Bootstrap method was used to investigate the values of the E_T^{miss} integral and means, including the improvements and errors. Therefore, we conclude that the results are reliable, and as consequence the resulting values have been integrated in the E_T^{miss} calculation. Two jet definitions, EMTopo and PFlow, are used to study the E_T^{miss} performance. The impact of the overlap between physics objects (muon-jet and electron, photon, tau-jets) are studied using overlap removal techniques and applied. Different working points are defined to meet the requirements of all ATLAS analyses. The resulting E_T^{miss} reconstruction was deployed in the ATLAS Software framework and used by a large number of analyses to either reject no genuine E_T^{miss} backgrounds or events with large E_T^{miss}. E_T^{miss} is a crucial physics object for searches for invisible particles from BSM physics, where these invisible particles are included in the search requirements through cuts

on E_T^{miss}, such as in the case of searches for Higgs produced via VBF and decaying into invisible particles, one of the main contribution work of this dissertation (chapter 5).

Chapter 5:

Search for invisible Higgs boson decays with vector boson fusion signatures

This chapter represents a direct search for Higgs bosons produced via Vector Boson Fusion (VBF) and decay into invisible particles ($\chi\bar{\chi}$) [91, 92]. The data used in the analysis corresponds to an integrated luminosity of 139 fb^{-1} of proton-proton collisions at $\sqrt{s} = 13$ TeV recorded at the LHC by the ATLAS detector during the run–2 period from 2015 to 2018 [2, 4].

Many BSM extensions predict a significant value of $\mathcal{O}(10)\%$ for the branching ratio ($\mathcal{B}_{H\to\text{inv}}$) of the invisible Higgs decay. While the expectation of the SM is merely (0.12)%. The model targeted in this analysis is the one where the Higgs boson might decay into a pair of WIMPs . These models are known as the Higgs-portal models, where the Higgs boson plays the role of mediator to DM. They are able to predict the observed relic DM density using s-channel ($\chi\bar{\chi} \to f\bar{f}$) annihilation processes and provide DM candidate.

The VBF topology offers robust discrimination of the signal from backgrounds originating from a single vector boson produced in association with two jets from QCD radiation. Figure 30 shows Feynman diagrams for the signal and dominant backgrounds. The QCD multijet events represent the largest source of background and are suppressed by requiring a large missing energy transverse (E_T^{miss}). The second important background is from the single boson produced in association with two jets. Events with Higgs bosons created via gluon-gluon Fusion (ggF) mechanism, as well as the associated production with a vector boson (VH) are considered in the signal. The contributions of these two topologies are tiny compared to the VBF process after the event selections.

The analysis looks for excesses of events over SM predictions in various topologies: ggF, VBF, and the association production with a single vector (W or Z) or $t\bar{t}$ pairs. No excess is observed and an upper limit on $\mathcal{B}_{H\to\text{inv}}$ of the 124 GeV SM Higgs is placed. The statistical combination of results using 36 fb^{-1} run–2 data by ATLAS set an observed (expected) limit of 0.26 (0.16) [93], while CMS report values of 0.19 (0.15) at 95% (CL) [94]. The VBF channel for ATLAS and CMS represents the highest expected sensitivity among the combination inputs, with values of 0.37 (0.28) and 0.33 (0.25), respectively [5, 94].

5.1 Monte Carlo simulation

Monte Carlo samples used in the analysis are summarized in Table 6.

Table 6: Summary of generators used for simulation for both signals and dominant backgrounds.

Process	Generator	ME order	PDF	Parton shower	Tune
Strong V+jets	Sherpa 2.2.1, Sherpa 2.2.7 (m_{jj}-filtered)	NLO (up to 2 jets), LO (up to 4 jets)	NNPDF3.0nnlo	Sherpa MEPS@NLO	Sherpa
Electroweak V+jets	Herwig 7.2.1	NLO (for 2 jets)	MMHT2014nlo	Herwig angular-order and Pythia 8 dipole recoil	Herwig 7.2
V+jets α_{EW}^3 interference	MadGraph5_aMC@NLO	LO	PDF4LHC15	Pythia 8	
Strong VV+jets (including $gg \to VV$+jets)	Sherpa 2.2.1 or Sherpa 2.2.2	NLO (up to 1 jet), LO (up to 3 jets)	NNPDF3.0nnlo	Sherpa MEPS@NLO	Sherpa
Electroweak VV+jets	Sherpa 2.2.1 or Sherpa 2.2.2	LO	NNPDF3.0nnlo	Sherpa MEPS@LO	Sherpa
$t\bar{t}$	Powheg Box v2	NLO	NNPDF3.0nlo	Pythia 8	A14
QCD multijet	Pythia 8.230	LO	NNPDF2.3lo	Pythia 8	A14
ggF Higgs	Powheg NNLOPS	NNLO	PDF4LHC15nnlo	Pythia 8	AZNLO
VBF Higgs	Powheg	NLO	PDF4LHC15	Pythia 8 dipole recoil	AZNLO
VH Higgs	Powheg Box v2	NLO	PDF4LHC15	Pythia 8	AZNLO

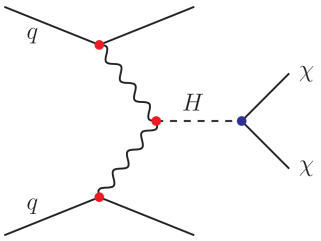

(a) Signal process

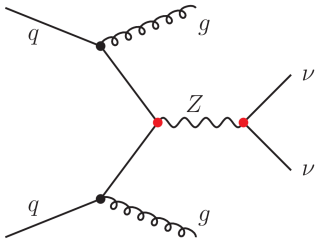

(b) Strong Z+jets background

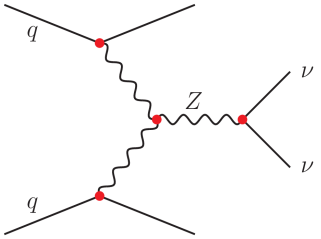

(c) Electroweak Z+jets background

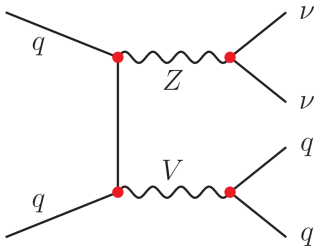

(d) Diboson (ZV) background

Figure 30: Feynman diagrams representating (a) the signal and the three dominant background processes: (b) strong Z+jets, (c) electroweak Z+jets, and (d) diboson production. The two latter processes are collectively referred to as 'electroweak' Z production. Electroweak vertices are shown as red markers. By reason of simplicity, no distinction is made between particles and antiparticles, or between different quark flavours [2].

5.2 Object and event selection

The analysis uses only events with a primary vertex, defined as the vertex with the highest sum of squared transverse momenta and having at least two associated tracks with $p_T > 0.5$ GeV. Electrons and muons are useful for background estimation, whereas photons are used to ensure orthogonality with other ATLAS analyses. Section 3 delves into more details on the reconstruction of these physical objects. For events with leptonic decays of vector bosons, the leading lepton is required to have a $p_T > 30$ GeV, and fulfill a loose isolation criterion. Lepton in $W(\to \ell\nu)$ + jets processes, uses a 'tight' criterion for electrons identification and a 'medium' criterion for muons. While for the two leptons in $Z(\to \ell\ell)$ + jets, the identification uses 'loose' criteria for electrons and muons. Only photons in the region of $|\eta| < 2.37$ with $p_T > 20$ GeV fulfilling 'tight' identification and isolation criteria. Events with this isolated photon are vetoed.

The analysis considers PFlow jets in the region of $|\eta| < 4.5$ with $p_T > 20$ GeV. Furthermore, JVT discriminant is used for jets with $p_T < 60$ GeV and within $|\eta| < 2.5$ to define the hard-scatter jets. fJVT discriminant is used to identify hard-scatter jets, if either of the two leading jets has $p_T < 120$ GeV and $|\eta| > 2.5$. The efficiency to accept hard-scatter jets is 97% for JVT and 93% for fJVT, which also rejects about 58% of pileup jets with $p_T > 50$ GeV. A tighter fJVT requirement is applied to suppress the multijet background for events

with $E_T^{miss} < 200$ GeV, resulting in an efficiency of 70% to 90% to accept hard-scatter jets and suppressing about 80% of pileup jets.

The analysis handles the overlap between the reconstructed physics objects through their separation in (y, ϕ)-space, as shown in Table 7, to avoid double counting of any energy deposit.

Table 7: Overview of the overlap removal procedure applied to different physics objects.

Remove	Keep	Matching criteria
electron	electron	shared ID track, electron with low p_T removed
muon	electron	muon with calorimeter energy deposits and shared ID track
electron	muon	shared ID track
photon	electron	$\Delta R < 0.4$
photon	muon	$\Delta R < 0.4$
jet	electron	$\Delta R < 0.2$
electron	jet	$\Delta R < min(0.4, 0.04 + 10\text{GeV}/p_T^e)$
jet	muon	number of tracks < 3 and $\Delta R < 0.2$
muon	jet	$\Delta R < min(0.4, 0.04 + 10\text{GeV}/p_T^\mu)$
jet	photon	$\Delta R < 0.4$

5.2.1 The VBF signature

The experimental signature of VBF processes in the detector is characterized by a pair of energetic quark-induced jets with a broad gap in the pseudorapidity ($\Delta\eta_{jj}$) and large invariant masses (m_{jj}) of the two jets with the largest transverse momenta (p_T). The two leading jets lie in opposite hemispheres of the detector and are more forward than jets from other processes under comparable conditions. To be distinguished from the multijet background, the two VBF leading jets must not have a back-to-back topology in the transverse plane. VBF processes are characterized by reduced hadronic activity, due to the absence of colour connection between the two quarks. VBF events can have additional jets, originating from initial- and final-state radiation, with $p_T > 25$ GeV. These events are considered, but with further requirements on the centrality (C_i) and the relative invariant mass (m_i^{rel}) of the third and fourth leading jets ($i = j_3, j_4$):

$$C_i = \exp\left(-\frac{4}{(\eta^{j1} - \eta^{j2})^2}(\eta^i - \frac{\eta^{j1} + \eta^{j2}}{2})^2\right) \tag{67}$$

$$m_i^{rel} = \frac{min\{m_{j1,i}, m_{j2,i}\}}{m_{jj}} \tag{68}$$

Requiring small values of the C_i allows the consideration of sub-leading jets from final-state radiation, and suppression of QCD contribution, where the sub-leading jets are emitted close to the midpoint of the rapidity gap ($C_i \approx 1$). The m_i^{rel} test checks the possibility that a third or fourth sub-leading jet radiated from one of the VBF leading jets is the smaller of

the invariant mass relative to m_{jj}. Small values of m_i^{rel} indicate that the additional jet is compatible with final-state radiation.

A complete list of selections to accept events in the signal region is provided in Table 8. Following these selections, 90% of te events entering the SR are from the VBF process, with

Table 8: Event selection criteria for the VBF signal region.

Quantity	Requirement
N_ℓ	0
N_γ	0
N_{jet}	2-4 (with $p_{\text{T}} > 25$ GeVand JVT requirement if $\|\eta\| < 2.5$)
N_b	< 2
$j_1(j_2)$ p_{T}	$> 80(50)$ GeV(with fJVT requirement if $\|\eta\| > 2.5$ and $p_T < 120$ GeV)
$E_{\text{T}}^{\text{miss}}$	> 160 GeV
$E_{\text{T}}^{\text{miss}}$ soft term	< 20 GeV
$p_T^{\text{all-jets}}$	> 140 GeV
$\Delta\phi_{jj}$	< 2.0
$\Delta\eta_{jj}$	> 3.8
$\eta^{j_1} \cdot \eta^{j_2}$	< 0
m_{jj}	> 0.8 TeV
If 3 or 4 jets ($i = j_3, j_4$)...	
centrality C_i	< 0.6
m_i^{rel}	< 0.05

a selection efficiency for an invisible Higgs boson of about 1.1%.

To increase sensitivity, the signal region is then split into sixteen orthogonal bins. Three 'multijet' bins are defined for events with three or four jets (that pass the proper criteria, as shown in Table 8) using m_{jj} binning. Three additional low E_T^{miss} bins are defined in the region of $160 < E_T^{miss} < 200$ GeV using similar m_{jj} binning in the previous 'multijet' bins. The remaining events with exactly two jets are binned in the $(m_{jj}, \Delta\phi_{jj})$ plane into five m_{jj} and two $\Delta\phi_{jj}$ regions for a total of ten bins. The binning scheme is illustrated in Figure 31.

5.3 Background estimation

Principal backgrounds contributing to this analysis are V+jets and QCD multijet. The multiboson (VVV), diboson (VV) and $t\bar{t}$ are minor backgrounds predicted from the Monte Carlo (MC) simulation.

5.3.1 V+jets backgrounds

The V+jets events represent the dominant background $\sim 95\%$ in the SR. To constrain this contribution, the analysis uses a data driven technique that uses W($\to \ell\nu$) and Z($\to \ell\ell$) CR that are divided into 16 bins similarly to the SR in Figure 31.

Identical selections to the ones in Table 8 are used for the Z and W CRs. The lepton veto is replaced by the requirement of exactly the same flavor and opposite charge, and

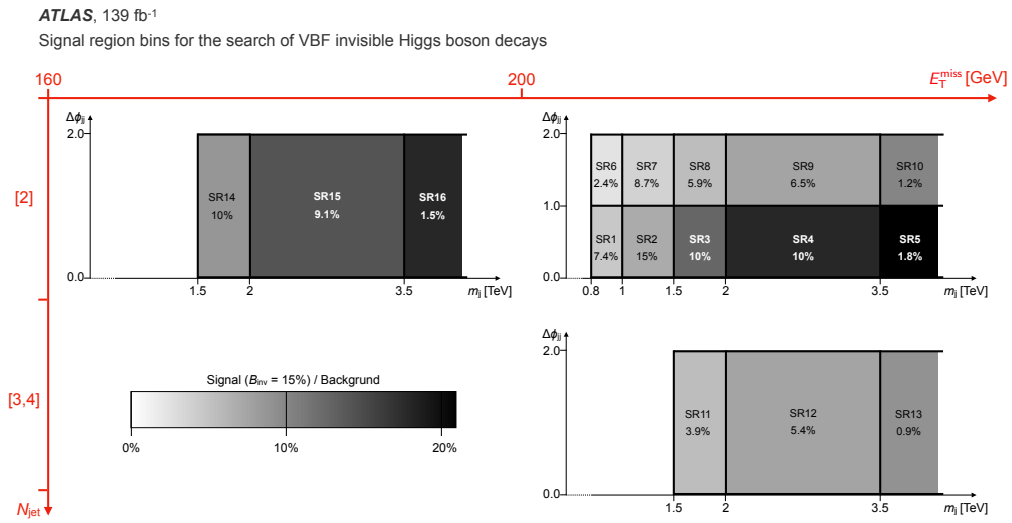

Figure 31: Signal region binning scheme for VBF analysis. Ten analysis bins are defined in the m_{jj} vs. $|\Delta\phi_{jj}|$ plane, with 5 total m_{jj} bins and two $|\Delta\phi_{jj}|$ bins for events requiring exactly two jets. Additional three 'multijet' bins and three low E_T^{miss} bins defined in the m_{jj} axis for events with 3 or 4 jets. Percentages indicate the fraction of signal in each bin relative to the total signal yield in the inclusive SR, and the gray scale saturation reflects the S/B of the bin, where darker bins have larger S/B values [2].

$|m_{\ell\ell} - m_Z| < 25$ GeV for $Z_{\ell\ell}$ CR. The leading lepton must have a $p_T > 30$ GeV, and the $E_T^{miss} < 70$ GeV (leptons included) to suppress backgrounds from VV and VVV production, VBF $H \to W^*W$ and $H \to \tau\tau$. A comparison of the observed and expected yields in the $Z_{\ell\ell}$ CR and the expectation from simulation is shown in Figure 32.

The $W_{\ell\nu}$ CR events must have a 'signal lepton' with $p_T > 30$ GeV, and then events are split according to the lepton flavor. $W_{e\nu}$ can have a small contribution from events with fake electron originating from misidentified multijet process jet, which is suppressed by additional requirement on the E_T^{miss} significance ($S_{MET} > 4\sqrt{\text{GeV}}$). A further 'fake-e CR' is enriched with events failing the S_{MET} cut, where the fake-e contribution can be extracted in each bin, by subtracting the MC predictions for processes with real electrons from the data. Fake electrons in $W_{e\nu}$ CR are evaluated using a $W_{e\nu}$ anti-ID CR filled with electrons passing only a loose identification requirement (see Figure 35(b)). The fraction of events with high S_{MET} to the number of events with low S_{MET} ($\mathcal{R}_S$) in the data is evaluated after suppression of the relevant background (W, Z, VV, VVV and $t\bar{t}$). Then the fake electron contribution in bin i is defined as $\mathcal{R}_{S,i}.n_{\text{fake-e},i}$, with, $n_{\text{fake-e},i}$ is the data events excess over the expected prompt background in the fake electron CR. Events in $W_{\mu\nu}$ CR can also be polluted with fake muon contribution from a misidetified jet, and this contribution is suppressed by requiring large transverse mass $m_T = \sqrt{2E_T^{\ell}E_T^{miss}(1-\cos\phi(\ell, E_T^{miss}))} > 20$ GeV, and the events that fail this requirement make up the fake-μ CR (see Figure 35(b)). Similarly to the case of electron, a $W_{\mu\nu}$ anti-ID CR enriched with fake muons is defined, and where the W, Z, VV, VVV and $t\bar{t}$ background is subtracted. Fake events in the $W\mu\nu$ CR are estimated using the ratio $\mathcal{R}_M$ of event with high m_T to low m_T. The fake contribution is given by $\mathcal{R}_M.n_{\text{fake-}\mu,i}$, where $n_{\text{fake-}\mu}$ is the excess in the event from data over expected prompt background in the fake-μ CR. The

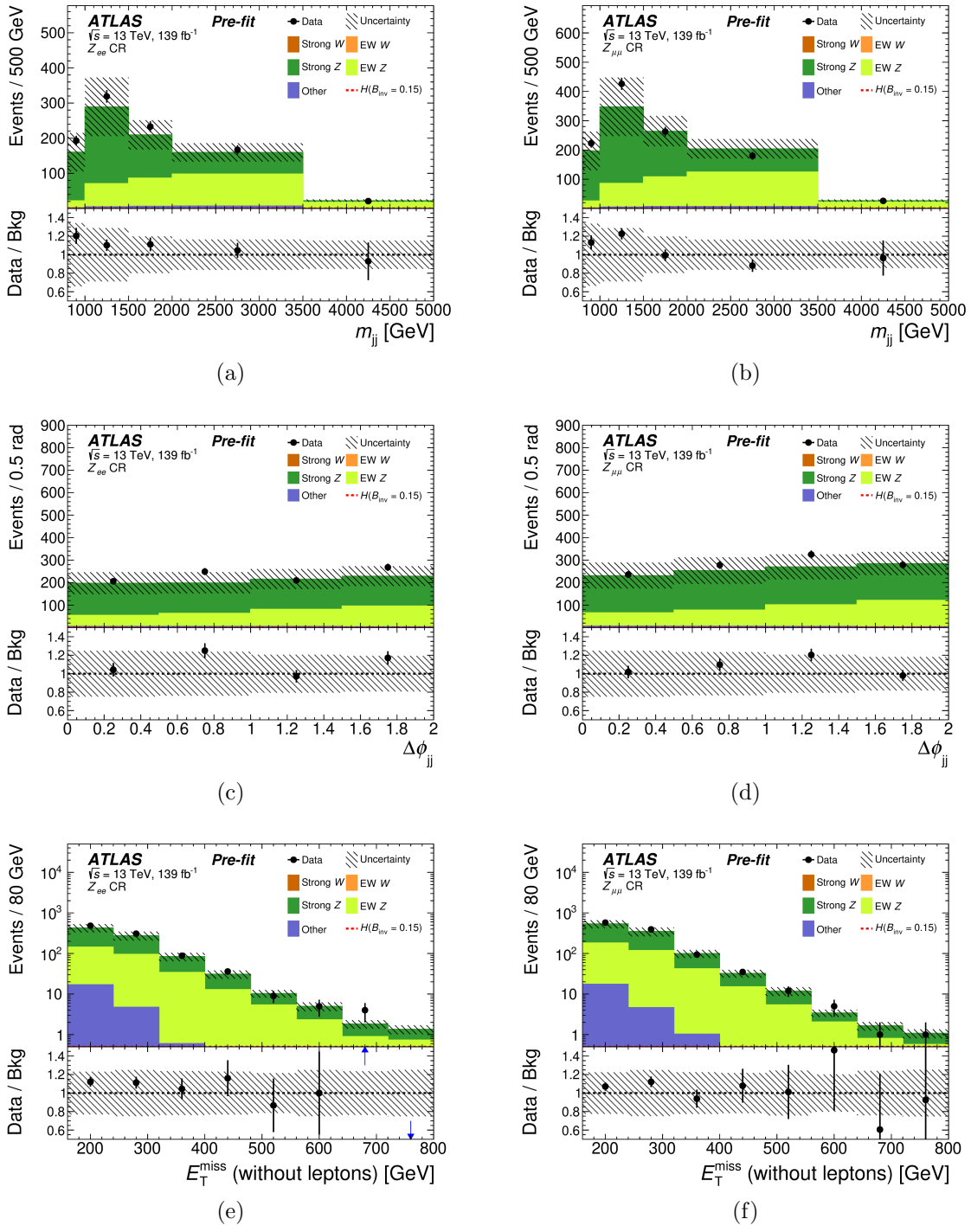

Figure 32: Observed and predicted distributions for m_{jj} in the $Z_{\ell\ell}$ CR, for $Z \to ee$ and $Z \to \mu\mu$. The MC predictions are normalised to cross sections times luminosity and are shown prior to the likelihood fit. Other stands for contributions from $t\bar{t}$, VV, VVV and VBF H with $H \to \tau^+\tau^-$. The combined uncertainty from MC sample sizes and experimental sources are presented with hashed bands [2].

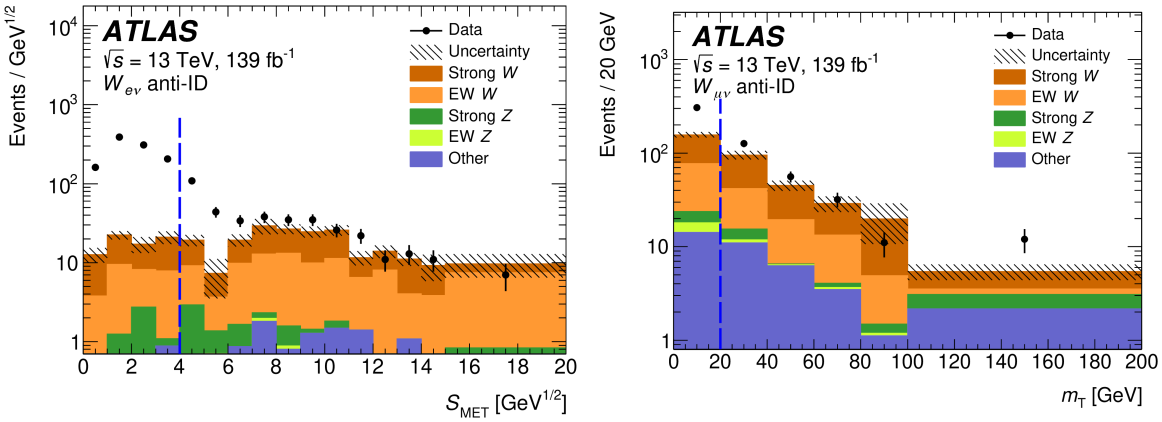

(a) (b)

Figure 33: Figure (a) shows of the comparison of the S_{MET} distribution in data and simulation for the $W_{e\nu}$ anti-ID control region, for which the electron passes a loose identification criterion but not the tight one. Figure (b) shows a comparison of the transverse mass m_T distribution in data and simulation for the $W_{\mu\nu}$ anti-ID control region, for which the muon candidate does not pass the loose identification criterion. Other stands for contributions from $t\bar{t}$, VV, VVV and VBF H with $H \to \tau^+\tau^-$. Excesses are caused by multijet events containing a fake lepton. The combined uncertainty from MC sample sizes and experimental sources are presented with hashed bands [2].

averaged value of $\mathcal{R}_S$ ($\mathcal{R}_M$) on all 16 bins is found to be 0.12 ± 0.01 (0.29 ± 0.15). Observed yields in data are showed in comparison to expected yields from simulation in Figure 34.

To overcome the statistical limitation in the $Z_{\ell\ell}$ CR, that lead to large uncertainties that limits the sensitivity of the analysis, the $W_{\ell\nu}$ CR is used to estimate the $Z_{\nu\nu}$ contribution in the SR. This was motivated by the aim to control the V+jets background at the percent level, where precision measurements with theoretical predictions for the $Z + 2$jets and $W + 2$jets ratio are exploited [95]. $V +$ jets production at NLO QCD and EWK are considered, and the ratio $\mathcal{R}_{TH}^{Z/W}$ is evaluated as a function of the generator-level m_{jj} [95]. The expectations for Z+jets processes are reweighed by $\mathcal{R}_{TH}^{Z/W}/\mathcal{R}_{MC}^{Z/W}$ in all CRs and SRs, where $\mathcal{R}_{MC}^{Z/W}$ is the cross-section ratio in the same VBF-like region as used for the numerator. The correction to the strong V + jets prediction is below 5% across the whole m_{jj} range (Figure 35(a)); however, for the electroweak V + jets prediction it varies between 20% at low m_{jj} values and 5% at large m_{jj} values (Figure 35(b)). These significant corrections at low m_{jj} originate from the fact that simulated event samples are missing NLO s-channel contributions and interference between s- and t-channel processes.

5.3.2 Multijet background

Jets from multijet processes tends to have momentum balance in the transverse plane at generator level, but neutrinos produced in subsequent decays of c- and b-hadrons can give rise to some E_T^{miss}. However, important E_T^{miss} can emerge at reconstruction level, due to some

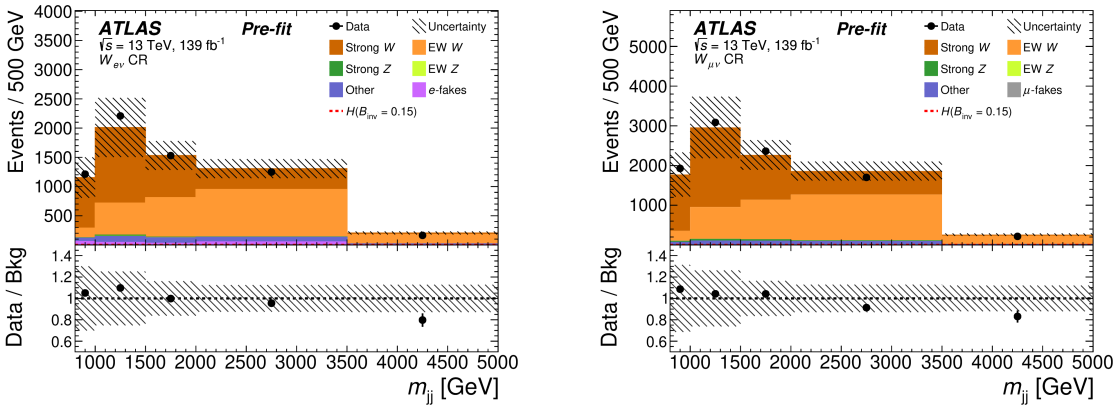

(a)

(b)

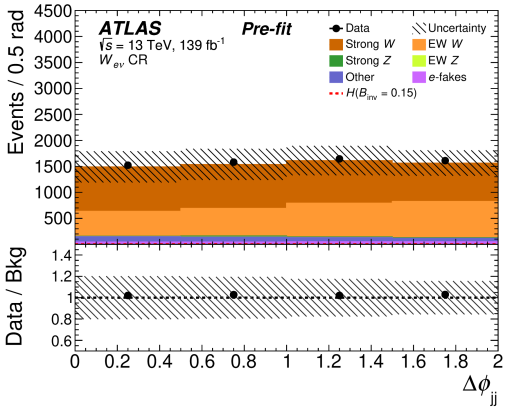

(c)

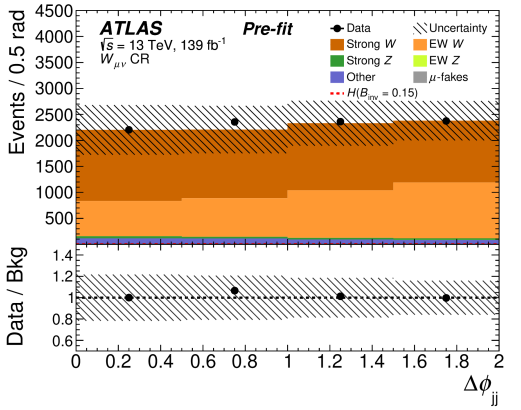

(d)

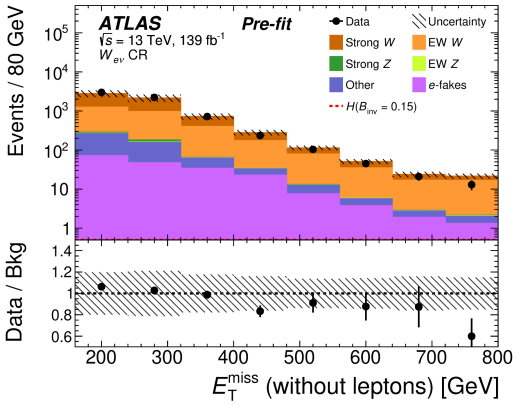

(e)

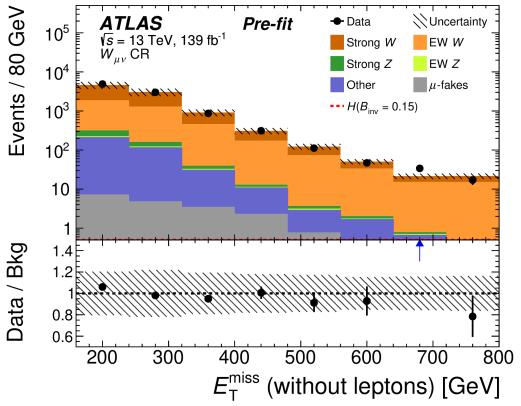

(f)

Figure 34: Observed and predicted distributions for m_{jj}, ϕ and E_T^{miss} in the $W_{\ell\nu}$ CR, for $W \to e\nu$ and $W \to \mu\nu$. The MC predictions are normalised to cross sections times luminosity and are shown prior to the likelihood fit. Other stands for contributions from $t\bar{t}$, VV, VVV and VBF H with $H \to \tau^+\tau^-$. The combined uncertainty from MC sample sizes and experimental sources are presented with hashed bands [2].

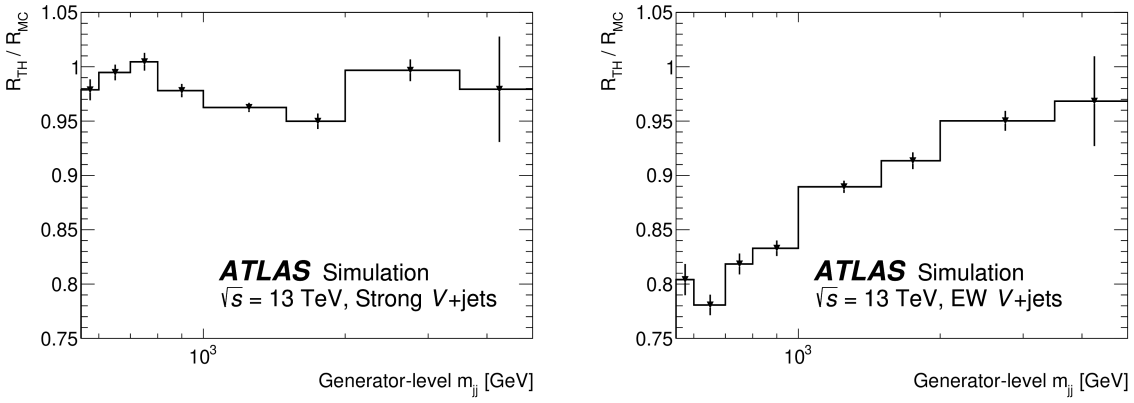

(a) (b)

Figure 35: $\mathcal{R}_{TH}^{Z/W}/\mathcal{R}_{MC}^{Z/W}$ ratio as a function of generator-level m_{jj}, which is used to correct the (a) strong and (b) electroweak V+jets simulation to achieve state-of-the art precision for the ratio of Z+jets to W+jets cross-sections in the kinematic region targeted by the analysis. The error bars show the statistical uncertainty of the simulation [2].

occasionally experimental effects, like fluctuations in the detector's response to jets, quantified by the jet energy resolution (JER), and "punch-through" effect where shower shapes are more elongated, which enhances the chance of a shower particle to exit the calorimeter and not having their energies fully deposited in the calorimeter, as well as misclassification of jets as originating from the hard-scatter or a pileup processes. Signal selections suppress heavily such contributions by requiring large E_T^{miss} and bounding $\Delta\phi_{jj}$ for the leading jets. Even so, in case of important pileup activity, a jet mismeasurement combined with a mistagging of pileup jets can produce signal-like topologies. In such circumstance, the leading jets can be originating from different scattering processes, thus they are uncorrelated and can be separated by small $\Delta\phi_{jj}$. Moreover, The two jets can have separate hadronic system resulting in additional reconstructed jets, which lead to rejection of the related event from the SR. Nevertheless, These events can enter the SR when the additional jets are lost, either by not passing the jet p_T requirement or by misclassification by pileup tagging.

Two methods are used for the suppression of multijet background, a modified version of the 'Rebalance and Smear' (R+S) technique used in [5] and the 'pileup-CR' method, which is a data-driven approach that uses multijet-enriched control regions. The two methods uses independent data sets to estimate the multijet background in each SR bin with associated uncertainties, and the final multijet estimate is carried by the most accurate method or a combination of the estimates from the two methods in some parts of the SR. Table 9 shows control regions used for the multijet background estimation and validation.

'Rebalance and Smear' technique uses separately two sets of inputs: single-jet-triggered data events and simulated multijet events, resulting in two different assumptions and separate predictions. It can be performed through two main steps. First, the construction of a sample of multijet events that exhibit momentum balance in the transverse plane, and then, detector response and event reconstruction is emulated multiple times per event, leading to occasionally

Table 9: Different control regions used for the estimation of multijet background. Only changes relative to the SR selection are given. The third column indicates if a control region is binned in $\Delta\phi_{jj}$ and m_{jj} like the signal region. Except for the MJ CR, which uses single-jet-triggered data, all control regions use E_T^{miss}-triggered data.

Region	Definition	Binned	Purpose
MJ CR	$100\,\text{GeV} < E_\text{T}^\text{miss} < 200\,\text{GeV}$ and $m_\text{jj} > 400\,\text{GeV}$ $N_\text{jet} = 2$, $\Delta\eta_\text{jj} > 2.5$ no requirement on $p_\text{T}^\text{all-jets}$	no	Determine HS-only and HS+PU composition
low-m_jj CR	$150\,\text{GeV} < E_\text{T}^\text{miss} < 200\,\text{GeV}$ $2 \leq N_\text{jet} \leq 4$, $200\,\text{GeV} < m_\text{jj} < 800\,\text{GeV}$ $\Delta\eta_\text{jj} > 2.5$, ($\lvert\eta^{j1}\rvert > 2.4$ or $\lvert\eta^{j2}\rvert > 2.4$) $\Delta\phi_\text{jj} < 1$, no requirement on $p_\text{T}^\text{all-jets}$	no	Multijet (R+S) normalisation Estimate non-closure uncertainty
mid-m_jj CR	$160\,\text{GeV} < E_\text{T}^\text{miss} < 200\,\text{GeV}$ $N_\text{jet} = 2$, $800\,\text{GeV} < m_\text{jj} < 1500\,\text{GeV}$ $\Delta\phi_\text{jj} < 1$, no requirement on $p_\text{T}^\text{all-jets}$	no	Same as low-m_jj CR
pile-up CR	$\lvert\eta^{j1}\rvert > 2.4$ and j1 is PU tagged no pile-up-tagging requirement for j2 $2 \leq N_\text{jet} \leq 4$ no m_i^rel requirement for $1 < \Delta\phi_\text{jj} < 2$	yes	Scaled by R_MJ to obtain multijet yield in SR
low-MET CR	$100\,\text{GeV} < E_\text{T}^\text{miss} < 160\,\text{GeV}$	yes	Numerator of R_MJ
low-MET PU-CR	same as pile-up CR, but $100\,\text{GeV} < E_\text{T}^\text{miss} < 160\,\text{GeV}$	yes	Denominator of R_MJ
low-MET VR	$110\,\text{GeV} < E_\text{T}^\text{miss} < 150\,\text{GeV}$ loose fJVT requirement no requirement on $p_\text{T}^\text{all-jets}$	no	Performance check of pile-up CR method

producing events that enter the SR. Simulated events must satisfy the requirement of having a transverse momentum imbalance less than 30 GeV. Next, they are divided based on the nature of the jet, being a HS jet if it matches to a generator-level jet with $\Delta R < 0.1$, or a pileup (PU) jet if it not matches to any truth jet. HS-only samples are made of events with two or more HS jets, but no PU jet with $p_T > 50$ GeV. The existence of at least one PU jet alongside two or more HS jets define the HS+PU samples. In the case of data events, a pileup tagging is used to separate HS jets from PU jets. Which are identified as stemming from the same scattering process, if two pileup-tagged jets with $p_T > 15$ GeV and exhibiting a back-to-back ($\Delta\phi > 2.7$) topology are present in the event. HS-only samples contain events with no PU jets of $p_T > 25$ GeV, and HS+PU samples contain events with at least two PU jets. Each of the input present advantages and disadvantages. Using simulated events results in a clean separation of HS and PU jets, while using data events relies on pileup-tagging, which is less efficient but results in more accurate estimation.

The 'rebalance' of jets consists of adjustment of their momenta within the experimental resolution in a way that the transverse momentum balance is conserved. PU jets remain unchanged if the simulated events are used, while the two back-to-back PU jets are rebalanced if data events are used. The expected jet response is evaluated using simulated events and uses as parameters the jet energy and η separately for light- and heavy-flavour jets, and it is used to 'smear' the 'rebalanced' jets. After the smearing, it is necessary to re-evaluate the pileup jet tagging, since the selection efficiency depends on the jet momentum that is adjusted. The events are smeared up to 8000 times with appropriately reduced event weights to account for enormous event weights resulting from huge cross sections for some simulated processes or large prescale factors for single-jet triggers. The tails of the jet response function are sampled with increased probability for the three leading jets since significant oscillations in the jet response are the principal source of E_T^{miss} in multijet events. The HS and PU components of each event are rotated relative to each other by a random azimuthal angle numerous times to increase the size of the HS+PU sample. At this stage, the event selection is then performed to populate the SR and CR bins.

Samples of HS-only and HS+PU events are normalized according to a fit of $\Delta\phi_{jj}$ distribution in loose multijet CR in Table 9, using single-jet-triggered data. HS-only and HS+PU events exhibit a useful characteristic, while the first accumulates at large $\Delta\phi_{jj}$, the second type accumulates at low $\Delta\phi_{jj}$. This make the $\Delta\phi_{jj}$ distribution the most suitable for the normalisation. Figure 36 shows the m_{jj} and $\Delta\phi_{jj}$ distributions for HS-only and HS+PU samples derived from simulated events.

Furthermore, to account for the inefficiency of the E_T^{miss} trigger used for Data collection in SR bins uses the E_T^{miss} triggers which are not fully efficient and require corrections to be applied. These corrections are small compared to uncertainties in the region of $E_T^{miss} > 160$ GeV since the E_T^{miss} triggers are more efficient there. Lastly, to account for different pileup and trigger conditions, the multijet estimation is performed separately for the three data taking periods (2015-2016, 2017 and 2018).

Two dedicated control regions are used to test the method, low-m_{jj} CR and the mid-m_{jj} CR defined as shown in Table 9. Both CR use similar selection as the one for the SR, they have no requirement on the $p_T^{all-jets}$, but events have to fulfill $\Delta\phi < 1$ to increase each sample

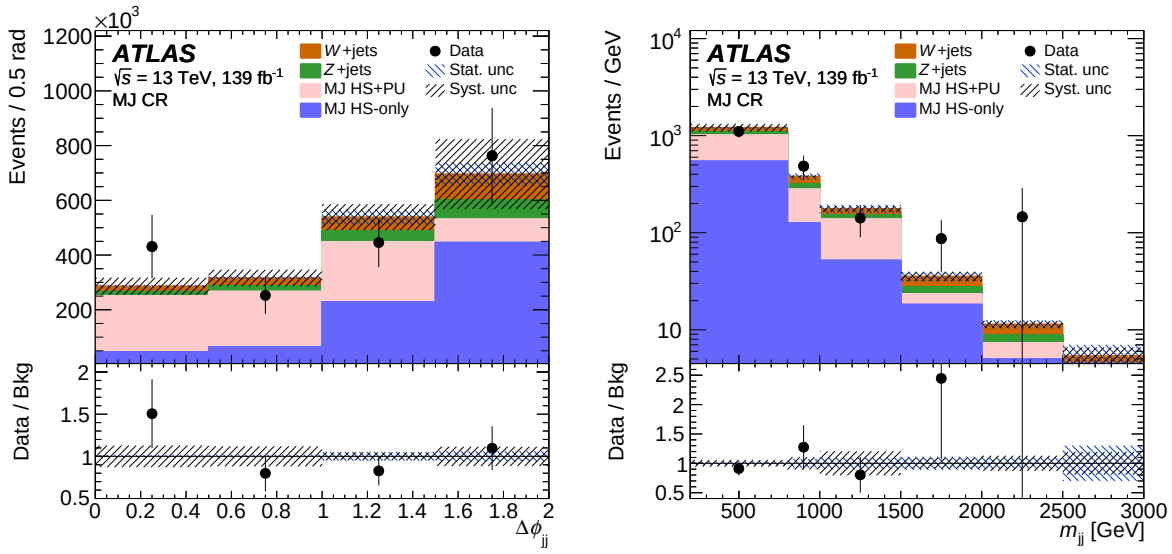

(a) (b)

Figure 36: Distributions of (a) $\Delta\phi_{jj}$ and (b) m_{jj} are shown in the multijet CR. The shapes of the multijet background components (HS-only and PU+HS) are estimated by the 'Rebalance and Smear' technique using simulated events as input. The components are normalized using a fit to the observed $\Delta\phi_{jj}$ distribution (a). The hatched bands indicate the statistical and the systematic uncertainties separately [2].

purity in multijet events. The data is collected using E_T^{miss} triggers, while multijets uses single-jet triggers. The observed data is used for the normalisation of the multijet prediction. The average normalisation factor from the two multijet CRs is used for the nominal multijet prediction, while half of the difference between the two normalisation factors is assigned as a 'non-closure' uncertainty of the method.

Three additional sources of systematic uncertainties in the 'Rebalance and Smear' method are known to have impact on the predictions: core and tail jet energy response and the ones rising from the difference between data and simulated events. To account for any differences between data and simulation, the smearing is repeated using systematically altered jet energy response distributions. The jet energy response is subjected to two uncertainty variations: a 15% widening of the 'core' part, which is simulated by a Gaussian distribution, and a 50% increase in the non-Gaussian tails. Finely binned data–MC comparisons of the widths and non-Gaussian tails of the dijet p_T asymmetry, which is intimately related to the calorimeter's response to jets [96], have led to these uncertainties. Differences from the nominal prediction are utilized to add a layer of systematic uncertainty to the equation. Seed events from simulation and data are utilized to anticipate the multijet background, and the difference is used as an additional systematic uncertainty. The inclusive multijet predictions and assigned systematic uncertainty are summarized in Table 10.

The pileup-CR method is an independent and innovative approach for the prediction of the multijet background, where a CR (PU-CR) enriched with multijet events is defined using the fJVT requirement inverted for the leading jet, i.e., demanding that the leading jet in p_T be

Table 10: Predicted multijet background, before the likelihood fit, entering the signal region bins with $N_{jet} = 2$ with associated uncertainties from the Rebalance and Smear method and the pileup CR method. The quoted uncertainty in the inclusive prediction is estimated by summing uncertainties from all sources in quadrature over the SR bins. The individual sources of uncertainty are given for the inclusive SR but also as a range for the individual SR bins

	Rebalance and Smear			Pile-up-CR method	
Multijet pred. (SR incl.)	840 ± 367			761 ± 186	
	Uncertainties [%]				
Source	inclusive	per bin	Source	inclusive	per bin
Statistical	9	6–46	Stat.	8.6	16–49 (bins 1–5 only)
Non-closure	40	37–43	Syst.	20	20–27
Jet energy response (core)	4.8	1–41			
Jet energy response (tail)	5.7	1–53			
Data vs simulation	4.9	2–30			

classified as a forward pileup jet. Also, no requirement on the fJVT value of the sub-leading jet is made. This ensures that the PU-CR contains both events with leading jets coming from various contacts and events with leading jets originating from the same scattering process. The multijet events make up to 92% of events in the PU-CR for 160 GeV $< E_T^{miss} <$ 200 GeV, while this contribution goes up to 95% for $E_T^{miss} >$ 200 GeV. PU-CR is then binned similarly to SR(Figure 31). A normalisation factor $R_{MJ,i}$ is used to scale the event yield N_i^{PU-CR} in the bin i of the PU-CR to the expected multijet background in the corresponding SR bin, which is measured at lower E_T^{miss} where the multijet background makes a major contribution. If only events with two jets are considered, the yields in the pileup CRs are biased to lower values in E_T^{miss} compared to the SR because forward pileup jets are only identified up to p_T values of 120 GeV. To validate the normalisation factor in the range of E_T^{miss}, the pileup CR event selection allows up to four jets, following requirements on third and fourth jets C_i and m_i^{rel} as stated in Section 5.2. The latest requirement (m_i^{rel}) for the third and fourth jets is dropped for the region $1 < \Delta\phi < 2$ of bins in the pileup CR, due to limitation in statistics. The event yields $N_i^{low-MET}$ and N_i^{PU-CR},low-MET at low E_T^{miss} between 100 GeV and 160 GeV are used to construct the normalisation factor $R_{MJ,i}$, with the remaining selection criteria being the same as the SR and pile-up CR bin definitions, respectively:

$$R_{MJ,i} = \frac{N_i^{\text{low-MET}} - B_{\text{non-MJ,i}}^{\text{low-MET}}}{N_i^{\text{PU-CR,low-MET}} - B_{\text{non-MJ,i}}^{\text{PU-CR,low-MET}}} \tag{69}$$

where $B_{\text{non-MJ},i}^{\text{low-MET}}$ and $B_{\text{non-MJ},i}^{\text{PU-CR,low-MET}}$ represent contributions from non-multijet processes in bin i. After subtracting the non-multijet backgrounds, the normalisation factor is applied to the event yield in the pileup CR to obtain a prediction of the multijet yield in the SR:

$$B_{MJ.i}^{SR} = R_{MJ,i}.(N_i^{\text{PU-CR}} - B_{\text{non-MJ},i}^{\text{PU-CR}}) \tag{70}$$

Where $B_{non-MJ,i}$ is the non-multijet backgrounds produced through simulation but normalised to the data. The ratio $R_{MJ,i}$ and the pileup CRs for 14, 15 and 16 SR bins (region of 160 GeV $< E_T^{miss} <$ 200 GeV) apply a tighter fJVT criteria than the remaining SR bins as mentioned in Section 5.2. The validation of the stability of $R_{MJ,i}$ according to E_T^{miss} is performed in bins of E_T^{miss} with a width of 10 GeV between values of 100 GeV and 160 GeV for the SR bins with 160 GeV $< E_T^{miss} <$ 200 GeV and between values of 100 GeV and 200 GeV for SR bins with $E_T^{miss} >$ 200 GeV. The bins 1–5, 6–10, and 14–16 are merged, in order to improve the statistical precision of this test. There is no statistically significant dependence on E_T^{miss}, and this effect is given a 20% uncertainty, which corresponds to the test's statistical precision. The statistical uncertainty of the observed $R_{MJ,i}$ is added in quadrature to this value for the individual bins, resulting in a normalisation factor uncertainty of 20% to 27%. This second approach is validated using a low-MET VR, enriched in multijet events with lower E_T^{miss} requirement (110 GeV $< E_T^{miss} <$ 150 GeV), no requirement on all-jets p_T, and the same loose fJVT requirement as the SR bins with $E_T^{miss} >$ 200 GeV. Figure 37 shows that data agree to background prediction within the uncertainties.

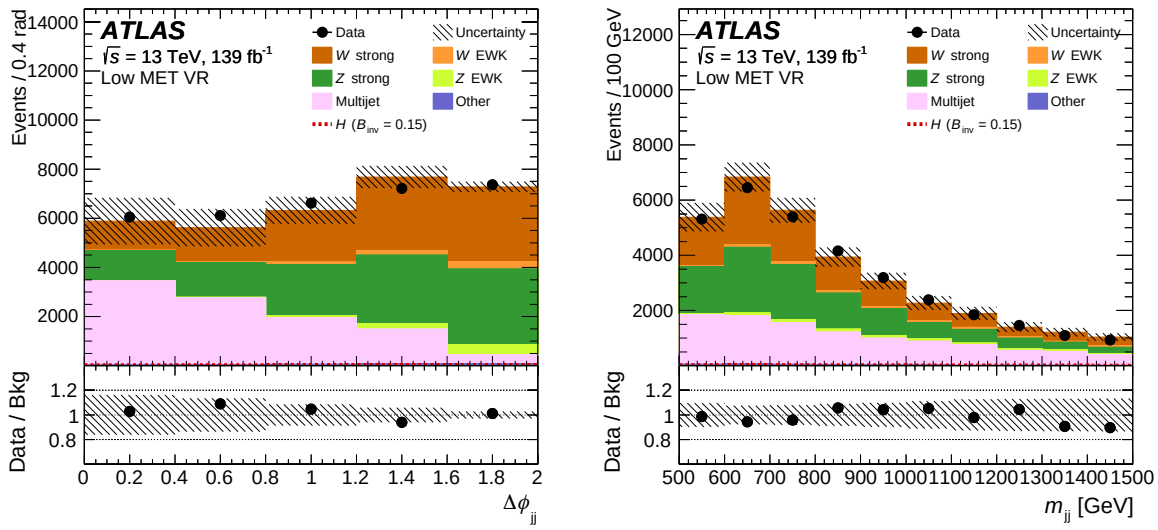

(a) (b)

Figure 37: The distribution of (a) $\Delta\phi_{jj}$ and (b) m_{jj} in the low-E_T^{miss} validation region. The multijet background is predicted by the pileup-CR method. Minor contributions from $t\bar{t}$, VV, VVV, and VBF H with $H \to \tau^+\tau^-$ or $H \to W^*W$ are combined and labelled 'other'. The hatched band indicates the statistical and systematic uncertainties of the backgrounds [2].

As mentioned before, Table 10 summarizes the predicted yields and their corresponding uncertainties for SR bins with exactly two jets ($N_{jets} = 2$). Because of leak of prediction from pileup CR method for SR bins with more than 2 jets ($N_{jets} = 3, 4$), these bins are removed from this comparison. The two methods are found to be in agreement within uncertainties for predictions in the inclusive SR. The uncertainties in the expected yields of SR bins with 160 GeV $< E_T^{miss} <$ 200 GeV and $\Delta\phi_{jj} < 1$ using pileup-CR method are smaller compared to the 'Rebalance and Smear' method, thus the predictions from the first method are considered.

The prediction in bins 6-10 ($1 < \Delta\phi_{jj} < 2$) are performed using pileup-CR method but inclusively due to limit in statistics. In order to avoid employing the same pileup-CR bins as for SR bins with $N_{jet} = 2$, the multijet prediction from the 'Rebalance and Smear' method is employed for the SR bins with $3 \leq N_{jet} \leq 4$.

5.4 Systematic uncertainties

Improving the analysis sensitivity requires a better control of both theoretical and experimental uncertainties.

Theoretical uncertainties originate principally from the limited order in which the matrix elements are calculated, the matching of those calculations to parton showers, and the uncertainty of the proton PDFs. These theoretical uncertainties affect both the signal and background processes, and they have been found to be negligible for the minor backgrounds from $t\bar{t}$, VV, VVV, and VBF H production.

Experimental uncertainties that have impact on analysis sensitivity are principally related to luminosity, trigger efficiencies and physics objects used in the analysis.

5.4.1 V+jets theoretical uncertainties

During event generation, there are four scales fixed: the renormalisation (μ_r), factorisation (μ_f), resummation (sometimes denoted 'qsf'), and CKKW matching scales. Variations of these four scales are used to assess the higher-order matrix-element effects and parton shower matching uncertainties.

To estimate the uncertainties associated with these choices, events are generated with the renormalisation and the factorisation scales varied upwards and downwards by a factor of 2, using on-the-fly varied event weights in the Sherpa MC simulation. The CKKW matching scale is an exception; its nominal value is 20 GeV and is varied to 15 and 30 GeV. For the factorization and renormalization scales, these uncertainties can be calculated using on-the-fly varied event weights in the reconstructed Sherpa Monte Carlo. This results in full statistical correlation between the varied and nominal samples. The corresponding uncertainties are calculated by taking an envelope of the 7-point factorisation/renormalisation scale variations (the central value, each scale independently varied up/down, and both scales coherently varied up/down). For the strong V+jets background, the effect of the seven-point scale variations on the expected yield in bins of m_{jj} are $^{+27\%}_{-18\%}$ at low m_{jj}, increasing to $^{+43\%}_{-26\%}$ at high m_{jj}. The corresponding values for the electroweak V+ jets background are $2\% - 14\%$ for Z+jets and 1%–8% for W+jets.

For the resummation and CKKW merging scales, separate varied samples need to be generated. Due to computing resource limitations, these cannot be reconstructed. So, the effect of the variations is determined at truth level and used to define a reweighting factors calculated with Sherpa 2.1, which is then applied to the fully-reconstructed nominal sample. The reweighting factors are binned in p_T^V, the transverse momentum of the produced vector boson, and the number of generator-level jets in the event. These are defined as half the difference between the up- and down-varied yields at truth-level, r_{up} and r_{down}, as follows:

$$\text{rel unc} = \frac{r_{up} - r_{down}}{r_{up} + r_{down}} \tag{71}$$

in each analysis bin. As such, they are symmetrized, unlike the factorization/renormalization scale variations. Due to statistical limitations, the statistical uncertainty on the size of these variations is sometimes larger than the variation itself. For this reason, a relaxed selection is applied to obtain the uncertainties associated with the resummation and CKKW variations as shown in Table 11

Table 11: Selections applied to obtain ckkw and resummation (qsf) uncertainties for different bins of the analysis.

Bins	Selections
Bin 1-10	$m_{jj} > 800$[GeV], $\Delta\eta_{jj} > 2.5$, $E^{miss}_{T,\text{nolep}} > 150$, $p^{jet}_T > 50, 50$[GeV]
Bin 11-13	$m_{jj} > 800$[GeV], $\Delta\eta_{jj} > 2.5$, $E^{miss}_{T,\text{nolep}} > 150$, $p^{jet}_T > 50, 50$[GeV], $N_{jet} \geq 2$
Bin 14-16	$m_{jj} > 800$[GeV], $\Delta\eta_{jj} > 2.5$, $160 < E^{miss}_{T,\text{nolep}} < 200$, $p^{jet}_T > 50, 50$[GeV]

These relative uncertainties are evaluated for all W+ jets and Z+ jets in all SR and all CRs bins. The relative uncertainties over m_{jj} are shown for $Z \to \nu\nu$ in the SR, $Z \to \ell\ell$ in CRZ, $W \to \ell\nu$ in CRW in Figures 38 for CKKW and resummation scales, respectively. The result of the variations for the factorisation/renormalisation, resummation, and CKKW scales are given in Table 12.

Table 12: The relative uncertainty over m_{jj} is shown for $Z_{\nu\nu}$ in the SR, $Z_{\ell\ell}$ in CRZ, $W_{ell\nu}$ in CRW in Figures for CKKW and resummation scales, respectively.

	Bin1	Bin2	Bin3	Bin4	Bin5	Bin6	Bin7	Bin8	Bin9	Bin10	Bin11	Bin12	Bin13	Bin14	Bin15	Bin16
								ckkw								
SRW %	2.96	2.65	2.21	1.31	-0.03	2.96	2.65	2.21	1.31	-0.03	2.21	1.31	-0.03	1.43	1.74	2.21
CRW %	3.62	3.38	3.04	2.36	1.34	3.62	3.38	3.04	2.36	1.34	3.04	2.36	1.34	2.59	2.25	1.75
TF %	0.63	0.71	0.81	1.03	1.35	0.63	0.71	0.81	1.03	1.35	0.81	1.03	1.35	1.13	0.5	0.46
SRZ %	7.64	7.69	7.76	7.91	8.13	7.64	7.69	7.76	7.91	8.13	7.76	7.91	8.13	6.99	7.34	7.84
CRZ %	7.8	7.72	7.59	7.35	6.99	7.8	7.72	7.596	7.35	6.99	7.6	7.35	6.99	9.79	11.44	13.91
TF %	0.15	0.03	0.15	0.51	1.06	0.15	0.03	0.15	0.51	1.03	0.15	0.51	1.06	2.55	3.69	5.33
								qsf								
SRW %	7.31	7.17	6.96	6.55	5.94	7.31	7.17	6.96	6.55	5.94	6.96	6.55	5.94	7.6	7.7	7.84
CRW %	9.46	8.85	7.97	6.22	3.58	9.46	8.85	7.97	6.22	3.58	7.97	6.22	3.58	9.36	8.25	6.58
TF %	1.97	1.55	0.94	0.32	2.28	1.97	1.55	0.94	0.32	2.28	0.94	0.32	2.28	1.61	0.5	1.18
SRZ %	7.58	7.02	6.21	4.59	2.16	7.59	7.02	6.21	4.59	2.16	6.21	4.59	2.16	7.36	7.36	7.36
CRZ %	2.65	2.75	2.9	3.2	3.64	2.6	2.75	2.9	3.2	3.64	2.9	3.2	3.64	1.24	1.24	1.24
TF %	4.81	4.15	3.22	1.35	1.43	4.81	4.15	3.22	1.35	1.43	3.22	1.35	1.43	6.04	6.04	6.04

The relative error, calculated as the average of the relative effects of the upwards and downwards variations, ranges from 4% to 8% for the resummation scale and from 4% to 6% for the CKKW scale.

The effects of the PDF uncertainties on the W+jets and Z+jets backgrounds are evaluated separately for each bin as the standard deviation of the yields obtained by using the different PDF replicas of the NNPDF set. This results in uncertainties ranging from 1% to 2%.

All theoretical uncertainties are treated as uncorrelated between strong and electroweak processes; however, uncertainty sources affecting W+jets and Z+jets events resulting from

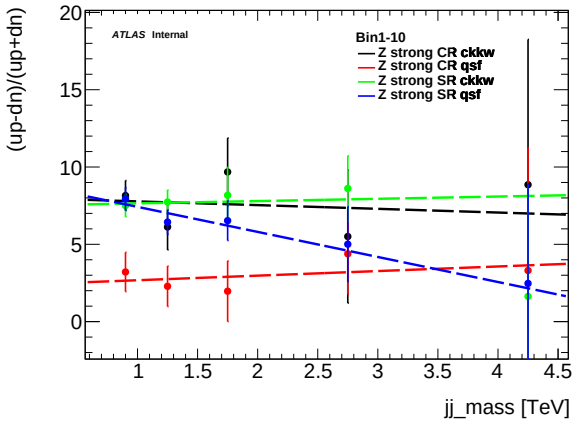

(a)

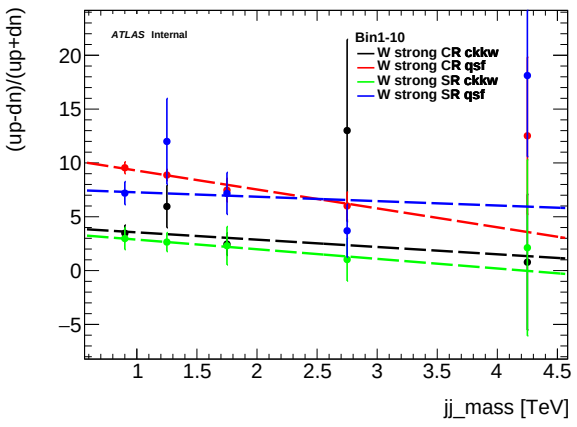

(b)

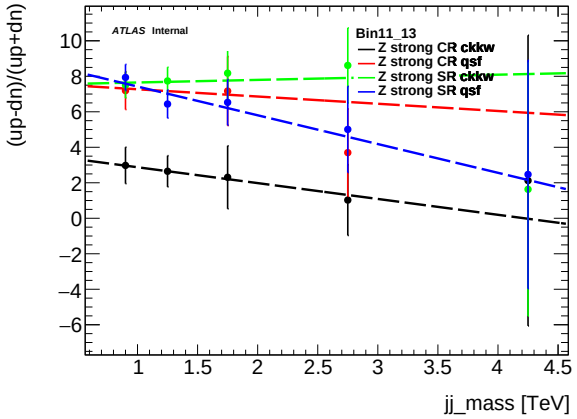

(c)

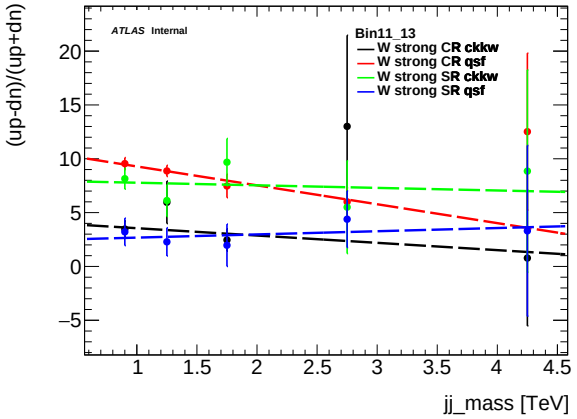

(d)

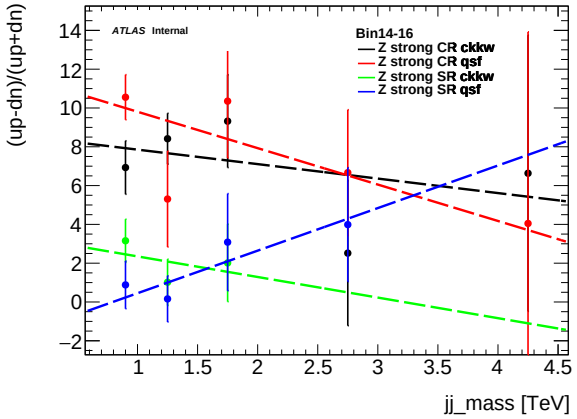

(e)

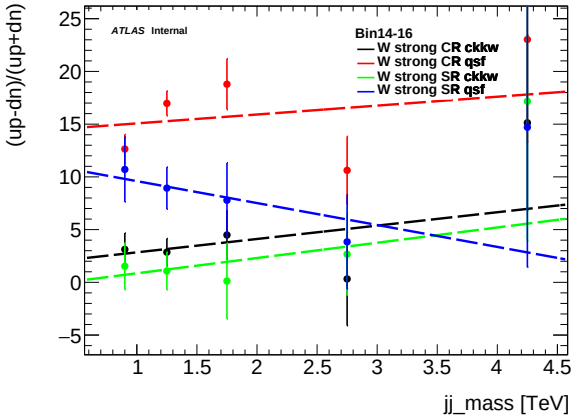

(f)

Figure 38: Theoretical uncertainties due to ckkw and qsf scale variations over the m_{jj} range for SR, CRZ and CRW, for all analysis bins

the same type of process are considered as correlated. In other words, an uncertainty variation that raises the strong Z+jets background in the SR likewise raises the strong Z+jets background in the SR and the corresponding backgrounds in the Z and W CRs. As a result, the total background yield's uncertainty in each signal region bin is significantly reduced. To measure how well the effects of these uncertainties cancel out, the variation of the ratio of each V+jets background in the SR to that in the corresponding CR is evaluated. The uncertainty in the value of each ratio is $1\% - 3\%$ and is dominated by the statistical uncertainties of the samples used.

The V+jets prediction is modeled by the likelihood fit (in Section 5.5) with one normalisation factor per each SR bin, so Z+jets and W+jets backgrounds are assumed to be correlated. Several uncertainties are then assessed by a dedicated NLO QCD and NLO electroweak calculation [95] of the $\mathcal{R}^{Z/W}$ ratio, which is used to refine the MC prediction of the W+jets and Z+jets backgrounds (in Section 5.3.1). The relative size of the impact of the NLO QCD corrections on the $\mathcal{R}^{Z/W}$ ratio is taken as the uncertainty, which amounts to $\sim 2\%$ for both the strong and electroweak processes across m_{jj} bins. The QCD and electroweak corrections are performed either additively or multiplicatively (default), resulting in a difference of less than 1% in all bins, which is designated as an uncertainty. For strong processes, parton shower uncertainties are calculated as the difference between $\mathcal{R}^{Z/W}$ values at NLO with and without parton shower simulation, and are evaluated to be 3% to 5%. For electroweak processes, they are evaluated as the difference between dipole and angular ordering in Herwig, yielding to uncertainties of less than 2%. The dedicated NLO QCD and NLO electroweak calculation does not use the same VBF selection as the analysis, nor does it give an $\mathcal{R}^{Z/W}$ value for each CR and SR bin. Alternately, in the case of strong V+jets production, the $\mathcal{R}^{Z/W}$ differences between the VBF-like region used to define $\mathcal{R}^{Z/W}$ and the individual SR and CR regions are estimated with Sherpa. The principal effect is due to the jet-veto requirement, which is estimated from Sherpa as the variation in $\mathcal{R}^{Z/W}$ when imposing the jet veto. It varies from 2% at low m_{jj} to 13% at high m_{jj} , where the contribution from strong V+jets production is comparatively small. For electroweak V+jets production, the dominant effect is the difference between the $\mathcal{R}^{Z/W}$ values for the inclusive $\Delta\phi_{jj}$ range and the individual generator-level $\Delta\phi_{jj}$ ranges of 0–1, 1–2, and > 2. This can range up to 11% and is estimated using the dedicated NLO QCD and NLO electroweak calculation. The difference between the requirement on $\Delta\phi_{jj}$ for the SR definition ($\Delta\phi_{jj} > 3.8$) and that for the NLO calculation ($\Delta\phi_{jj} > 2.5$) is covered by the assessed uncertainties and has a negligible impact on the final results. A summary of the theoretical uncertainties of $\Delta\phi_{jj}$ is given in Figures 39 for the strong and electroweak V+jets processes.

5.4.2 VBF theoretical uncertainties

The LHC Higgs working group provides the inclusive VBF and ggF Higgs boson production cross sections and uncertainties [97]. The p_T-dependent NLO electroweak correction introduces uncertainty into the VBF process. According to HAWK, this is expected to be 2%. The LHC Higgs working group computed the m_{jj}-dependent impacts of the renormalisation and factorisation scale uncertainties, as well as their correlations, for the Powheg+Pythia signal sample [97]. The factorization and renormalization scales are adjusted separately. To calculate the uncertainty related to the jet veto, the Stewart–Tackmann technique [98] is

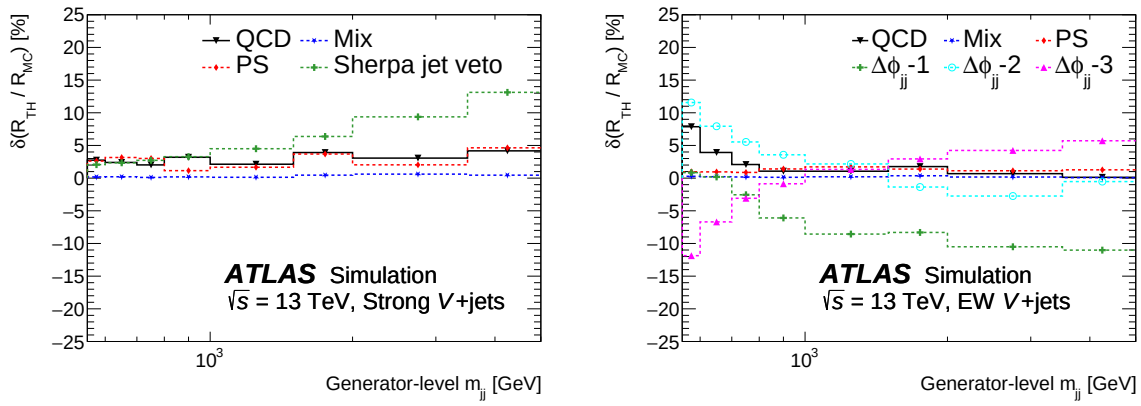

(a) (b)

Figure 39: Fractional uncertainties of the double ratio $\mathcal{R}_{TH}^{Z/W}/\mathcal{R}_{MC}^{Z/W}$. 'QCD' refers to the change in the ratio induced by the NLO QCD corrections, 'Mix' shows the difference between additive and multiplicative application of the NLO QCD and NLO electroweak corrections, and 'PS' stands for the uncertainties attributed to the parton shower. For the strong V+jets processes (a), 'Sherpa jet veto' denotes the difference between the ratios with and without a jet veto being applied. For the electroweak V+jets processes (b), the three '$\Delta\phi_{jj}$-[1,2,3]' uncertainty components quantify the impact of the $\Delta\phi_{jj}$ dependence on the correction and are evaluated in the ranges 0-1, 1-2, and > 2 [2].

deployed. The range of these uncertainties is between 1% to 3%. Parton shower uncertainties are expected to have a 2%–4% effect on the VBF signal when compared to a Powheg+Herwig 7 sample. The VBF signal is impacted by 1–2% by PDF uncertainties computed from the NNPDF collection.

5.4.3 ggF theoretical uncertainties

The Higgs boson production mechanism in gluon-gluon fusion (ggF) is sensitive to scale variations. Furthermore, the fraction of the events in ggF+2 jets is sensitive to jet bin migrations. We estimate the jet bin uncertainty on the ggF+2 jets using the Steward-Tackmann(ST) procedure [98]. This procedure produces uncertainties larger than the spread of scale variation in each jet bin, and it also gives a better estimate of the jet bin uncertainties for the process where the higher order corrections are sizable (e.g. the ggF process for example).

The factorisation (μ_f) and renormalisation (μ_r) scales independently are varied upward and downward for nine scale settings: the central scale ($\mu_f = \mu_r = m_H$) and 8 independent variations of μ_f and μ_r around the central scale. We applied the signal region selection discussed in Section 5.2.1. Kinematic selections on ggF Powheg+Pythia8 signal samples are done at truth level. The ST procedure consists of:

- **Jet veto uncertainty**: Evaluated the uncertainty on exclusive 2 jets cross section at the level of the jet selection. This is done by calculating the inclusive 2-jet cross section

Table 13: The fourth column shows the inclusive 2-jet cross section with the 3-jet cross section subtracted, with jet selection cuts. The last columns shows the acceptance of all the cuts as a function of scale variation. The uncertainty of each column is obtained as the maximum deviation from the central scale. In the case of exclusive two jets the uncertainties are $\Delta^2_{2jets} = \Delta^2_{\geq 2jets} + \Delta^2_{\geq 3jets}$ which gives $\Delta_{2jets} = \sqrt{(6.1 \times 10^6) \times 0.26^2 + (0.59 \times 10^6) \times 0.26^2} = 1.7 \times 10^6$, which is equivalent to 44% of the two jet bin cross section.
Applying the ST procedure, the jet bin uncertainty $\sqrt{3.1^2 + 44^2} = 44.1\%$ for the 2-jet bin selection on the ggF process.

μ_f, μ_r	inclusive 2jets cross section(arb.unit)	inclusive 3jets cross section	exclusive 2jets bin cross-section	Acceptance
m_H, m_H	6.10×10^6	2.25×10^6	3.86×10^6	1.98×10^{-3}
$0.5 \times m_H, 0.5 \times m_H$	7.72×10^6	2.84×10^6	4.89×10^6	1.97×10^{-3}
$1.0 \times m_H, 0.5 \times m_H$	6.23×10^6	2.30×10^6	3.93×10^6	2.01×10^{-3}
$2.0 \times m_H, 0.5 \times m_H$	5.17×10^6	1.91×10^6	3.26×10^6	2.03×10^{-3}
$0.5 \times m_H, 1.0 \times m_H$	7.62×10^6	2.70×10^6	4.83×10^6	1.95×10^{-3}
$2.0 \times m_H, 1.0 \times m_H$	5.05×10^6	1.85×10^6	3.19×10^6	1.2×10^{-3}
$0.5 \times m_H, 2.0 \times m_H$	7.55×10^6	2.75×10^6	4.79×10^6	1.92×10^{-3}
$1.0 \times m_H, 2.0 \times m_H$	6.00×10^6	2.20×10^6	3.80×10^6	2.95×10^{-3}
$2.0 \times m_H, 2.0 \times m_H$	4.94×10^6	1.81×10^6	3.12×10^6	1.95×10^{-3}
Uncertainty(%)	26.5	26.4		3.1

and subtracting the inclusive 3-jet cross section. [1]

- **Kinematic acceptance uncertainty**: applying all the selection criteria in Section 5.2.1 and compute the largest spread in the scale variations.

- Finally, adding the two above uncertainties in quadrature.

Table 13 shows the jet selection cross sections and the acceptances of the all cuts as a function of the scale variations. The ST procedure leads to an uncertainty of 45% on the ggF+2 jets in the VBF selection 5.2.1. The 3 or 4-jet category has an uncertainty of 41%. The following table summarizes the result with the corresponding jet selections. Results for total signal region cross-section are summarised for the inclusive 2-jets and exclusive 2-jets. The signal regions are divided based on dijet mass and eta difference between the two leading

Table 14: Jet bin uncertainties for inclusive 3-jets and the exclusive 2-jets.

Signal regions	inclusive 3jets	exclusive 2jets
$m_{jj} < 0.8$, $\Delta\eta > 2.5$	26.7	44.2
$m_{jj} > 0.8$, $\Delta\eta > 3.8$	25.5	44.1
$0.8 < m_{jj} < 1$, $\Delta\eta > 3.8$	26.4	44.0
$1 < m_{jj} < 1.5$, $\Delta\eta > 3.8$	26.6	44.1
$1.5 < m_{jj} < 2$, $\Delta\eta > 3.8$	26.6	44.2
$2 < m_{jj} < 3.5$, $\Delta\eta > 3.8$	26.7	44.2
$m_{jj} > 3.5$, $\Delta\eta > 3.8$	26.8	44.3

jets. Table 14 jet bin uncertainties for ggF signal in the SR. The total signal region and all the sub-signal regions for both cases, inclusive 2-jets and exclusive 2-jets.

To conclude, uncertainties associated with the ggF process are also evaluated by renormalisation and factorisation scale variations. A Stewart–Tackmann procedure is used to estimate

[1] The m_{jj}, $\Delta\phi_{jj}$, $\Delta\eta_{jj}$ and N_{jet} requirements are removed for this calculation.

the jet bin migration uncertainty. This gives a 45% uncertainty in bins with $N_{jet} = 2$ and 41% in the bins with $N_{jet} = 3$ or 4. The smaller PDF and parton shower uncertainties are also included.

5.4.4 Experimental uncertainties

The sensitivity of the analysis is influenced by a number of experimental uncertainties. They fall into three categories: luminosity uncertainties, trigger efficiencies uncertainties, and uncertainty related to the physics objects used, such as electrons, muons, jets, and the E_T^{miss}.

The luminosity uncertainty is 1.7% [99], and it only affects the signal yield because its effect on the dominant V+ jets backgrounds is cancelled out in the selected method (see Section 5.3).

Because the E_T^{miss} triggers are not entirely efficient at values of 160 GeV or 200 GeV, systematic uncertainties must be taken into consideration to allow for potential trigger efficiency discrepancies between data and simulation. This is accomplished by comparing the combined L1+HLT efficiency turn-on curve for simulated signal events with the turn-on curve acquired from data utilizing single-muon triggers. They agree within the statistical uncertainty, which is below 1%. A further systematic uncertainty is obtained from the difference found in simulated samples, which is smaller than 0.5% for all signal region bins, to cover the difference between the trigger efficiencies for W and Z. Scale factors and uncertainties of the respective single-lepton and dilepton triggers are applied to the W and Z control regions.

The uncertainties of the reconstructed objects are considered and propagated into the E_T^{miss} calculation to see how they affect the expected yields. The uncertainty in the E_T^{miss} soft term's magnitude and resolution is also passed on to the overall E_T^{miss} uncertainty.

5.5 Statistical model

The signal yield is extracted from the observed event counts in the signal and control zones using a simultaneous maximum-likelihood fit. The likelihood is defined as the product of terms for the Poisson probabilities to observe each data count of bin i, $N_i^{CR/SR}$, from a signal-plus-background model. It also depends on a set of nuisance parameters θ_j that represent experimental and theoretical uncertainties, as well as a set of parameters indicating yields from multijet processes in the fake-e, fake-μ, and pileup CRs. Because the V+jets CR is enriched in events from V+jets processes. The β_i factors are almost exclusively calculated to match the data counts in V+jets CR bins, and the normalisation constraints are appropriately transferred to the V+ jets prediction in the corresponding SR bin. The signal region yield likelihood is:

$$\mathcal{L}^{\mathrm{SR}} = \prod_i \mathcal{P}(N_i^{\mathrm{SR}} | \beta_i . B_{Z,i}^{\mathrm{SR}} + \beta_i . B_{W,i}^{\mathrm{SR}} + B_{\mathrm{MJ},i}^{\mathrm{SR}} + B_{\mathrm{Other},i}^{\mathrm{SR}} + \mu . S_i^{SR}) \tag{72}$$

Where dependence of B and S on the nuisance parameters are not showed in the equation, to simplify the notation. $B_{W,i}^{SR}$ and $B_{Z,i}^{SR}$ represent the yields from simulation, for W+jets and

Z+jets respectively, and considering the weighted $B_{Z,i}^{SR}$ by the ratio $\mathcal{R}_{TH}^{Z/W}/\mathcal{R}_{MC}^{Z/W}$. Multijet background estimates are represented by $B_{\mathrm{MJ},i}^{\mathrm{SR}}$, and $B_{\mathrm{Other},i}^{\mathrm{SR}}$ stands for estimates from the combined minor background $t\bar{t}$, VV, VVV and VBF H production. μ is the signal strength, and S_i^{SR} is the simulated yield for an invisible Higgs boson decay branching fraction of 100%.

The prediction from multijet backgrounds are performed using pileup-CR and 'Rebalance and Smear' methods. The corresponding likelihood is defined as follows:

$$\mathcal{L}^{PU-CR} = \prod_{i\in[1,5] \text{ or } \{6-10\} \text{ or } [14,16]} \mathcal{P}(N_i^{\text{PU-CR}} | B_{\text{non-MJ},i}^{\text{PU-CR}} + n_{\text{PU-MJ},i}) \tag{73}$$

Where $B_{\text{non-MJ},i}^{\text{PU-CR}}$ is the non-multijet contribution determined from simulation, and {6–10} represents the index of the merged bins. The full multijet estimate considered in the signal region likelihood is as follows:

$$B_{\mathrm{MJ},i}^{\mathrm{SR}} = \begin{cases} n_{\text{PU-MJ},i} \cdot R_{\mathrm{MJ},i} & \text{for } i \in [1,5] \text{ or } [14,16] \\ n_{\text{PU-MJ},\{6-10\}} \cdot R_{\mathrm{MJ},\{6-10\}} \cdot f_{\mathrm{R+S},i} & \text{for } i \in [6,10] \\ B_{\text{MJ-R+S},i}^{\mathrm{SR}} & \text{for } i \in [11,13] \end{cases} .$$

The associated likelihood to the V+jets backgrounds are constrained by dedicated W and Z control regions is:

$$\begin{aligned} \mathcal{L}^{V\text{+jets-CR}} = & \prod_i \mathcal{P}\left(N_i^{Z\mathrm{CR}} \mid \beta_i \cdot B_{Z,i}^{Z\mathrm{CR}} + B_{\text{non-}Z,i}^{Z\mathrm{CR}}\right) \\ & \prod_i \mathcal{P}\left(N_i^{W\mu\nu\mathrm{CR}} \mid \beta_i \cdot B_{W,i}^{W\mu\nu\mathrm{CR}} + B_{\text{non-}W,i}^{W\mu\nu\mathrm{CR}} + R_M \cdot n_{\text{fake-}\mu,i}\right) \\ & \prod_i \mathcal{P}\left(N_i^{We\nu\mathrm{CR}} \mid \beta_i \cdot B_{W,i}^{We\nu\mathrm{CR}} + B_{\text{non-}W,i}^{We\nu\mathrm{CR}} + R_{S,i} \cdot n_{\text{fake-}e,i}\right), \end{aligned}$$

where $B_{V,i}^{VCR}$ are the simulated V+jets yields, separated by the lepton flavor for W+jets and the Z+jets yields in simulation are scaled by the same theoretical model for the ratio of Z/W as in the SR. $B_{\text{non-V},i}^{VCR}$ are the non-V+jets contributions to these control regions. The 'fake' electrons (muons) are modelled with free parameters $n_{\text{fake-}e,i}$ ($n_{\text{fake-}\mu,i}$) multiplied by the $R_{S,i}$ (R_M) scale factors in Section 5.3.1.

Likelihood of yield probabilities in the fake-e and fake-μ control regions is:

$$\begin{aligned} \mathcal{L}^{\text{fake-CR}} = & \prod_i \mathcal{P}\left(N_i^{\text{fake-}\mu\mathrm{CR}} \mid \beta_i \cdot B_{W,i}^{\text{fake-}\mu\mathrm{CR}} + B_{\text{non-}W,i}^{\text{fake-}\mu\mathrm{CR}} + n_{\text{fake-}\mu,i}\right) \\ & \prod_i \mathcal{P}\left(N_i^{\text{fake-}e\mathrm{CR}} \mid \beta_i \cdot B_{W,i}^{\text{fake-}e\mathrm{CR}} + B_{\text{non-}W,i}^{\text{fake-}e\mathrm{CR}} + n_{\text{fake-}e,i}\right), \end{aligned}$$

The following likelihood is considered to constrain the nuisance parameters within their uncertainties, where a Gaussian probability density function $\mathcal{G}$ is used.

Table 15: Observed and expected limits on $\mathcal{B}_{H\to\text{inv}}$ for a Higgs boson with a mass of 125 GeV calculated at the 95% CL for a 139 fb^{-1} data set. The $\pm1\sigma$ and $\pm2\sigma$ variations of the expected limit are also shown.

Observed	Expected	$+1\sigma$	-1σ	$+2\sigma$	-2σ
0.145	0.103	0.144	0.075	0.196	0.055

$$\mathcal{L}^{\text{NP}} = \prod_j \mathcal{G}\left(0|\theta_j\right),$$

The full likelihood expression is the product of all terms:

$$\mathcal{L}(\mu, \vec{\beta}_V, \vec{n}_{\text{PU-MJ/fake-}e\text{/fake-}\mu}, \vec{\theta}) = \mathcal{L}^{\text{SR}} \cdot \mathcal{L}^{\text{PU-CR}} \cdot \mathcal{L}^{V\text{+jets-CR}} \cdot \mathcal{L}^{\text{fake-CR}} \cdot \mathcal{L}^{\text{NP}},$$

To set an upper limit on μ at 95% CL, Asymptotic formulae for the CL_s frequentist approach [100–102] are used, which corresponds to the observed upper limit on the branching fraction of invisible Higgs boson decays.

5.6 Results

Data validation region enriched with events of $2 < \Delta\phi_{jj} < 2.5$ is used to test the background estimation techniques, and the used ratio of the W+jets and Z+jets cross sections and corresponding uncertainties. The VR uses five bins, binned similarly to SR bins 1-5 and 6-10, and they are defined for W+jets, Z+jets, fake-e and fake-μ. The 'Rebalance and Smear' method is used for multijet estimation, and the likelihood function is adjusted to count only for the reduced number of bins. The resulting background expectations are compared with the observed yields as shown in Figure 40. Good agreement between the total background prediction and data yields is obtained across all bins.

The fit strategy shown in Section 5.5 is performed on data, and a good agreement is observed between the predicted and observed yields, within the evaluated uncertainties. The event yields in the sixteen signal selection bins after a background-only likelihood fit, i.e., with the signal strength μ set to zero, are compared with the observed numbers of events in CR and SR bins in Figure 41.

An upper limit of 0.145 is established on the branching fraction of Higgs boson decays into invisible particles at a 95% confidence level since the fit does not demonstrate any considerable signal contribution. This is in agreement with the expected value of $0.103^{+0.041}_{-0.028}$ as shown in Table 15. In comparison with the observed (expected) limit on $\mathcal{B}_{H\to\text{inv}}$ of 0.37 (0.28) from the previous search [5], this analysis shows a significant improvement.

The limit on $\mathcal{B}_{H\to\text{inv}}$ is related to a limit on the spin-independent WIMP–nucleon cross section [103–106]. This allows the result obtained here to be compared with limits from a selection of the most sensitive direct-detection experiments [107–109] in Figure 42. The relation between $\mathcal{B}_{H\to\text{inv}}$ and $\sigma_{\text{WIMP-nucleon}}$ is presented in the effective field theory framework assuming that the new-physics scale is $\mathcal{O}(1)$ TeV, well above the scale probed at the Higgs

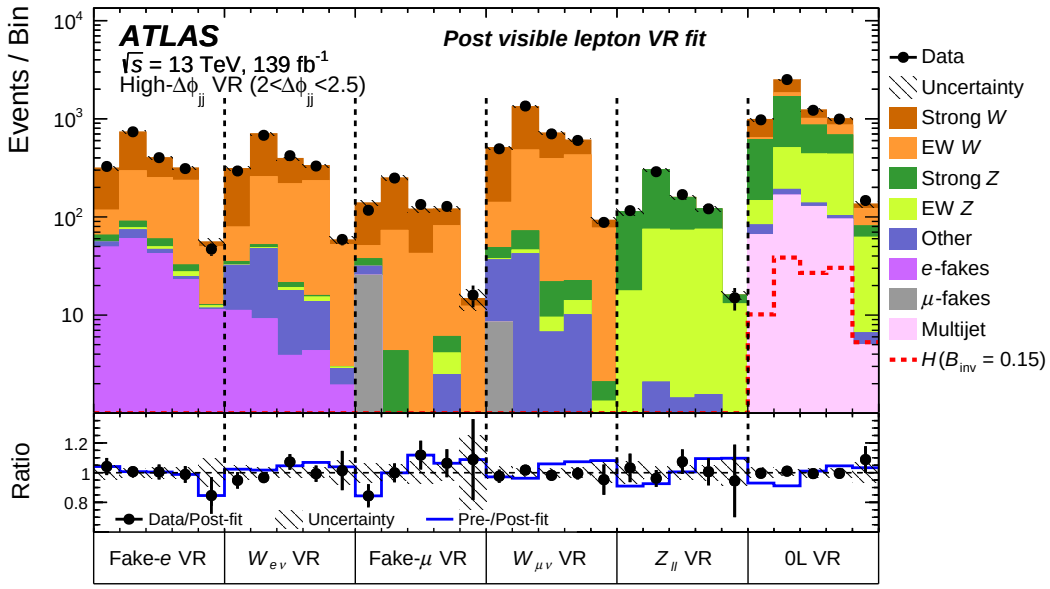

Figure 40: Post-fit yields and their corresponding uncertainties for all validation regions (VR) bins with $2 < \Delta\phi_{jj} < 2.5$ and with μ set to zero. The five bins in each region correspond to the m_{jj} bins of the SR bins 1–5 and 6–10. The fit is performed only in the VR bins with one or two leptons, and the fitted background scaling factors β_i are applied to the corresponding VR bins with zero leptons. Minor contributions from $t\bar{t}$, VV, VVV, and VBF H with $H \to \tau^+\tau^-$ or $H \to W^*W$ are combined and labelled 'other'. The resulting background expectations are compared with the observed yield. The signal is scaled to a branching ratio of 15% for an invisible decay of the Higgs boson. The ratio of the observed yields to the prediction of the model post-fit is shown by the points in the bottom plot and the relative change of the prediction with respect to the pre-fit yields is shown by the blue line [2].

boson mass [104]. To enable comparisons with the 90% CL direct-detection limits, the observed 90% CL upper limit of 12.7% on $\mathcal{B}_{H\to\text{inv}}$ from this analysis is used, the expected limit being 8.7%. For the scalar WIMP interpretation, cross sections exceeding values ranging from $3 \cdot 10^{-43}\,\text{cm}^2$ to $1 \cdot 10^{-45}\,\text{cm}^2$ are excluded for masses between 1 GeV and 60 GeV. For the Majorana fermion WIMP interpretation, cross sections exceeding values ranging from $4 \cdot 10^{-47}\,\text{cm}^2$ to $7 \cdot 10^{-45}\,\text{cm}^2$ are excluded for the same mass range, and for a vector-like WIMP the exclusion limit ranges from $5 \cdot 10^{-51}\,\text{cm}^2$ to $3 \cdot 10^{-46}\,\text{cm}^2$. Adding a renormalisable mechanism for generating the vector-like WIMP masses could modify the above-mentioned correlation substantially [1, 110, 111]. Many UV-complete models predict a new scalar particle that mixes with the Higgs boson. This adds at least two free parameters to the model, for example its mass m_2 and the mixing angle α. The dependence of the exclusion limit for the vector-like WIMP hypothesis on the mass m_2 is shown in Figure 42. The uncertainty band in the plot uses the latest computation of the nucleon form factors [112]. The overlay shows the complementarity in coverage by the direct-detection experiments and the searches at colliders, such as the presented analysis.

Furthermore, the limit is interpreted as a search for invisible decays of heavy scalar

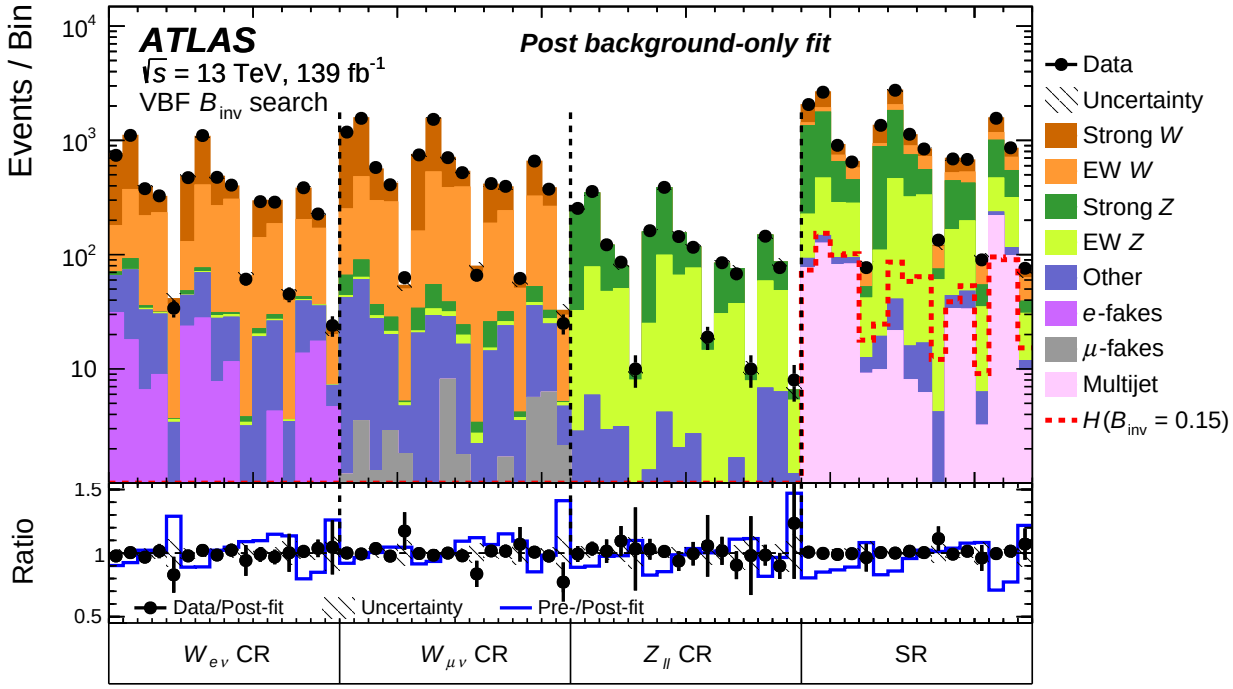

Figure 41: Post-fit results of all signal and control regions bins with μ set to zero. Less important contributions from $t\bar{t}$, VV, VVV, and VBF H with $H \to \tau^+\tau^-$ or $H \to W^*W$ are combined and labelled 'other'. The signal (dashed, red line) is scaled to a branching ratio of 15% for an invisible decay of the Higgs bosons. The 16 bins in the SR and each of the three CRs are defined in Figure 31. The fake-lepton and pile-up CRs, which contain an additional 41 bins that also enter the likelihood fit, are not shown, as this improves the readability. The ratio of the observed yields to the prediction of the model post-fit is shown by the points in the bottom plot and the relative change of the prediction with respect to the pre-fit yields is shown by the blue line [2].

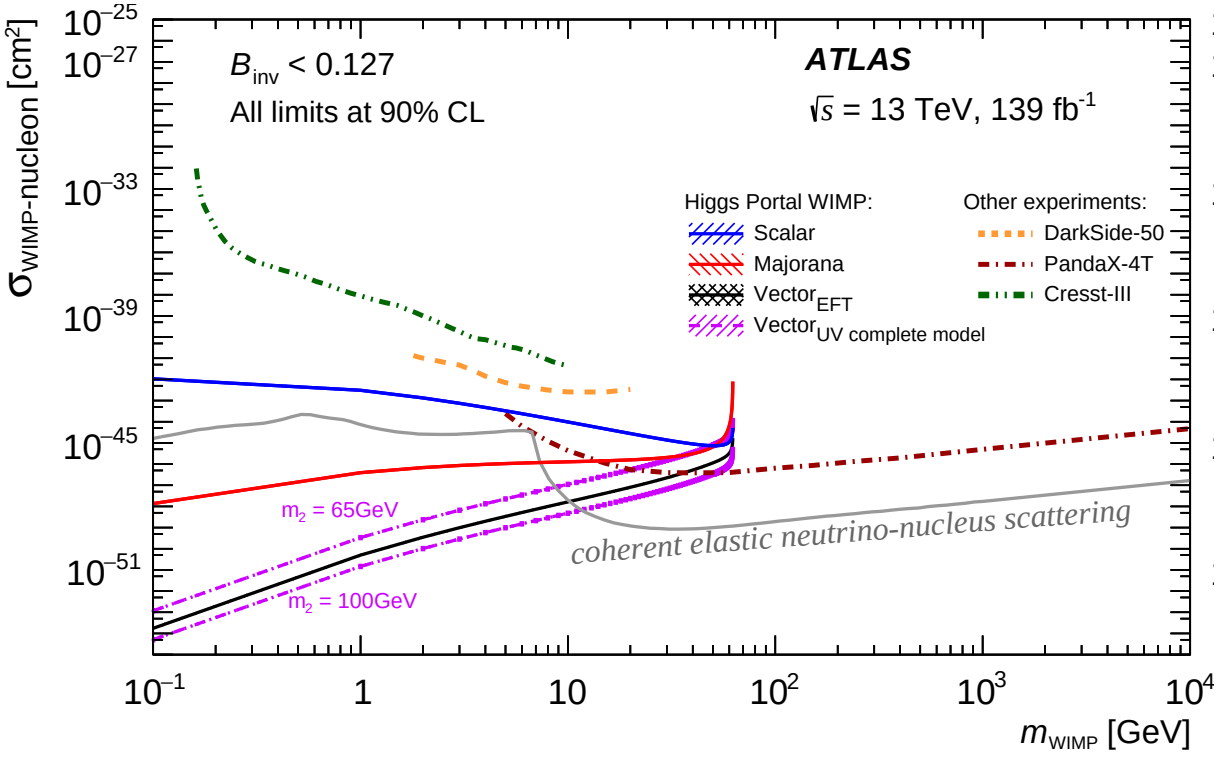

Figure 42: Upper limits on the spin-independent WIMP–nucleon cross section using Higgs portal interpretations of $\mathcal{B}_{H\to\text{inv}}$ at 90% CL vs m_{WIMP}. For the vector-like WIMP hypothesis, the dependence on the mass m_2 of the new scalar particle, which is often predicted by renormalisable models, is shown for three different values covering a wide range taken from Ref. [1] and which is discussed in details in Section 7. For comparison with direct searches for DM, the plot shows results from Refs. [107–109]. The neutrino floor for coherent elastic neutrino–nucleus scattering is taken from Refs. [113, 114] and assumes germanium as the target over the whole WIMP mass range. The dependence on the choice of target nucleus is relatively small, given the large range of cross sections shown [2].

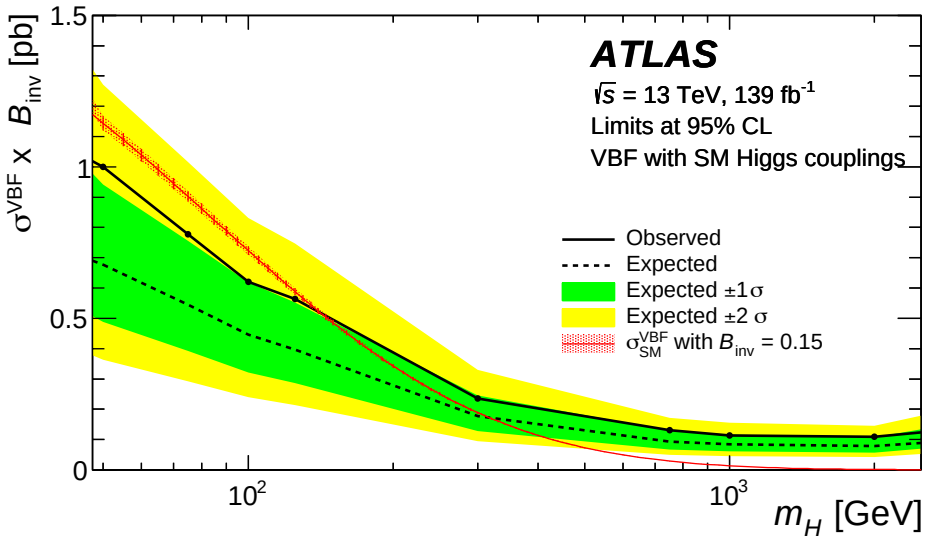

Figure 43: Upper limit on cross section times branching ratio to invisible particles for a scalar mediator as a function of its mass. For comparison the VBF cross section at NLO in QCD, i.e. without the electroweak corrections, for a particle with SM Higgs boson couplings, multiplied by a $\mathcal{B}_{H\to\text{inv}}$ value of 15%, is overlaid [2].

particles acting as mediators to dark matter. The upper limit on the product of cross section and branching ratio to invisible particles ($\sigma^{\text{VBF}} \cdot \mathcal{B}_{\text{inv}}$) is shown in Figure 43, where The heavy scalar mass ranges from 50 GeV to 2 TeV.

5.7 Conclusion

Results of a search for invisible Higgs bosons decays using a luminosity of 139 fb^{-1} of proton–proton collision data with a centre-of-mass energy of $\sqrt{s} = 13$ TeV collected by the ATLAS detector during the run–2 period of the LHC, are presented. The signature targeted is the VBF topology with two energetic jets that are not back-to-back in the azimuthal plane and exhibit a large rapidity separation, in addition to large values of $\Delta\phi_{jj}$ and E_T^{miss}. Since no excess is observed in the signal region , an upper limit of 0.145 is set on the branching fraction $\mathcal{B}_{H\to\text{inv}}$ into invisible particles at 95% CL, with an expected limit of 0.103, assuming the Standard Model cross section for the Higgs boson. This represent a significant improvement of ∼36% compared to the latest result that used 36 fb^{-1} of Run-2 data. The result is interpreted using Higgs portal models to exclude regions in the parameter space of $\sigma_{\text{WIMP-nucleon}}$ and m_{WIMP} for various WIMP models, and furthermore as a search for invisible decays of new scalar particles with masses of up to 2 TeV.

Chapter 6:

Combination of searches for invisible Higgs boson decays

During LHC run–1, many direct searches for invisible Higgs boson decays were conducted using up to 4.7 fb^{-1} and 20.3 fb^{-1} of proton-proton collision at center-of-mass energy $\sqrt{s} = 7$ TeV and 8 TeV in 2011 and 2012 respectively [115]. These searches were statistically combined, and the resulting upper limit on the invisible Higgs branching fraction $\mathcal{B}_{H\to\text{inv}}$ at 95% CL to $0.27^{+0.10}_{-0.08}$ is observed [115]. This chapter presents the result of the statistical combination of the run–2 searches for Higgs bosons decays into invisible particles, using VBF and $t\bar{t}H$ topologies [3, 115, 116]. Both results from 0- and 2-leptons final states are considered for $t\bar{t}H$. These results are then combined with searches from run–1 [115]. This analysis is performed with the assumption of the Standard Model Higgs boson production. Visible decay modes of the Higgs boson are not considered.

6.1 Searches for the invisible decay of the Higgs boson

The channels considered in the combination include: Search for invisible decays of the Higgs boson via VBF [4], search for invisible decays of the Higgs boson in the $t\bar{t}H$ topology in the 0ℓ and 2ℓ channels [3, 116], and run–1 combination [115].

6.1.1 VBF topology

The analysis [4] targets the VBF topology in Section 5 with additional changes on the event selection, background suppression techniques and the binning strategy. Only events with $E_T^{miss} > 200$ GeV are considered in order to suppress the contamination from multijet events. Events with 2, 3 or 4 jets are considered, with the two leading jets fulfilling the VBF requirements and the additional jets are compatible with the hypothesis that they originate from final-state radiation. $Z \to \ell\ell$+2jets and $W \to \ell\nu$+2jets control regions were used to constrain V+jets background in the signal region, and a data-driven method is used for the multijet estimation. The analysis uses eleven bins in the signal and control regions: the first ten bins are exactly similar to the ones in Figure 31 and the eleventh bin for events with more than two jets. An upper limit of $0.13^{+0.05}_{-0.04}$ on the $\mathcal{B}_{H\to\text{inv}}$ at 95% CL is observed.

6.1.2 $t\bar{t}$ topology

The 0ℓ channel of the $t\bar{t}H$ analysis [116] targets a search for a scalar partners of the top quark (top squarks), by considering all hadronic decays of the $t\bar{t}$ system from events collected using $E_{\text{T}}^{\text{miss}}$ trigger. Events should have at least two b-jets with $E_{\text{T}}^{\text{miss}} > 250$ GeV to be considered. To cover the different kinematic regions of the supersymmetric particles considered, four

signal regions are defined. For invisible Higgs interpretation, only two orthogonal signal regions designed to address two-body top-squared decays are considered. These regions are further divided into three parts using the mass of the reclustered large-radius jet ($R = 1.2$) of the sub-leading top quark candidate ($m_2^{R=1.2}$) on points 60 and 120 GeV. The dominant background is Z+heavy-flavour jets, while minor contribution come from W+jets, $t\bar{t}Z$,$t\bar{t}$ and single-top Wt. MC simulation are used to model these background sources.

The 2ℓ channel is used for searches for new physics in events with final state characterized by two opposite-charge leptons (electrons or muons), jets and missing transverse momentum [3]. Events are collected using dilepton triggers, with event selection targeting spin-0 dark matter models, where the SM Higgs boson plays the role of a mediator created in association with $t\bar{t}$ and couples to the DM. To be considered, events must have at least one b-tagged jet and an $E_{\mathrm{T}}^{\mathrm{miss}}$ significance larger than 12. Then, they are split based on having the same or different flavor for the two leptons. In case of same flavor, the requirement on leptons invariant mass ($|m_{\ell\ell} - m_Z| > 20$ GeV) is added to constrain the Z+jets background. The stransverse mass m_{T2}, which is used to bound the individual masses of a pair of particles that are each assumed to have decayed into one visible and one invisible particle, is computed using the two leptons as visible particles. Then, it is used to define six bins, starting from 110 GeV, which enhance the analysis sensitivity. The main backgrounds are modeled using the MC simulation: $t\bar{t}$, $t\bar{t}Z$, single-top in the Wt channel, Z/γ^*+jets, and diboson processes.

The two analyses are individually interpreted as searches for the invisible Higgs boson, and the observed (expected) limits of the $t\bar{t}H$-0ℓ and $t\bar{t}H$-2ℓ channels are 0.94 ($0.64^{+0.29}_{-0.19}$) and 0.37 ($0.42^{+0.19}_{-0.12}$), respectively [3, 116].

6.1.3 run–1 combination

The ATLAS run–1 invisible Higgs searches used 4.7 fb^{-1} of proton-proton collision data at $\sqrt{s} = 7$ TeV and 20.3 fb^{-1} at $\sqrt{s} = 8$ TeV [115]. The combination considered inputs from Higgs boson produced via VBF or in association with a vector boson V decaying either leptonically ($Z \to \ell\ell$) or hadronically ($W/Z \to jj$). The resulting observed (expected) upper limit on the $\mathcal{B}_{H\to\mathrm{inv}}$ is 0.25 ($0.27^{+0.10}_{-0.08}$) at 95% CL [115], where the VBF signature is leading the sensitivity.

6.2 Statistical method

The statistical combination is performed by constructing the product of the analyses likelihoods and maximizing the resulting likelihood ratio:

$$\Lambda(\alpha, \theta) = \frac{L(\alpha, \hat{\hat{\theta}}(\alpha))}{L(\hat{\alpha}, \hat{\theta})} \tag{74}$$

where α is the parameter of interest and θ is the nuisance parameters. The nuisance parameters are set to their profiled values $\hat{\hat{\theta}}(\alpha)$ in the numerator, which maximise the likelihood function for fixed values of the parameter of interest α. While in the denominator, both parameters are set to the values $\hat{\alpha}$ and $\hat{\theta}$, which jointly maximise the likelihood. This is done in accordance with the implementation outlined in [117, 118]

6.3 Results

The best fit values of $\mathcal{B}_{H\to\text{inv}}$, observed upper limits, and expected upper limits from the different channels mentioned above and from the statistical combinations are summarized in Table 16 and Figures 44 and 45. The result is dominated by systematic uncertainties

Table 16: Summary of results from direct searches for invisible decays of the 125 GeV Higgs boson and their statistical combinations. Shown are the best-fit values of $\mathcal{B}_{H\to\text{inv}}$, as well as observed and expected upper limits on $\mathcal{B}_{H\to\text{inv}}$ at the 95% CL [3, 4, 115, 116, 119].

Analysis	Best fit value	observed upper limit	expected upper limit
$t\bar{t}H$-0ℓ	0.39 ± 0.30	0.94	$0.64^{+0.29}_{-0.19}$
$t\bar{t}H$-2ℓ	$-0.09^{0.22}_{-0.21}$	0.37	$0.42^{+0.19}_{-0.12}$
VBF	$0.00^{+0.07}_{-0.07}$	0.13	$0.13^{+0.05}_{-0.04}$
run–1 comb.	$-0.02^{+0.14}_{-0.13}$	0.25	$0.27^{+0.10}_{-0.08}$
run–2 comb.	$0.00^{+0.06}_{-0.07}$	0.13	$0.12^{+0.05}_{-0.04}$
run–1 + run–2 comb.	$0.00^{+0.06}_{-0.06}$	0.11	$0.11^{+0.04}_{-0.03}$

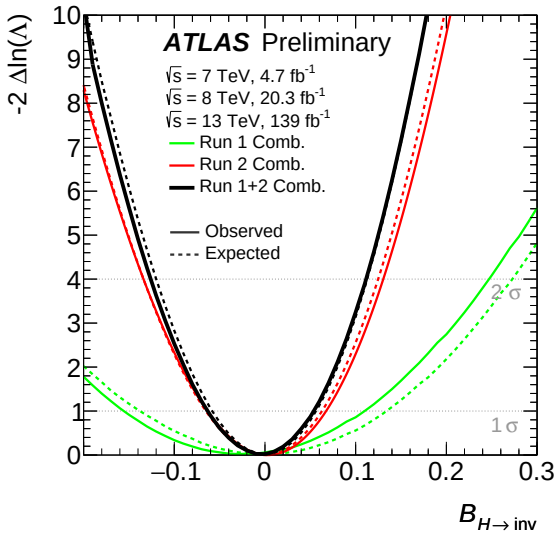

Figure 44: The expected and observed negative logarithmic profile likelihood ratios $-2\Delta\ln(\Lambda)$ as a function of $\mathcal{B}_{H\to\text{inv}}$ for the combined results using Run-1, Run-2, and their combination [119].

related to the number of simulated MC events, the reconstruction and identification of physics objects and the modeling of the background processes.

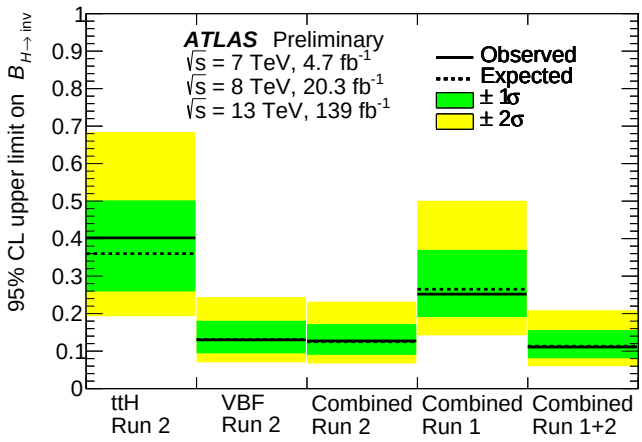

Figure 45: The observed and expected upper limits on $\mathcal{B}_{H\to\text{inv}}$ at the 95% CL from direct searches for invisible decays of the 125 GeV Higgs boson and their statistical combinations using run–1 and run–2 datasets. The (1σ) and (2σ) uncertainty bands on the expected limits are shown as green and yellow, respectively [119].

6.4 Interpretation

The results of the Higgs decays into invisible particles were translated into a (WIMP)–nucleon scattering cross section σ^{SI}(WIMP-N) which relies on models described in [103, 104, 120, 121]. These models assume that the WIMP interacts with the SM exclusively through its coupling to the Higgs boson. It also assumes that the process of Higgs decaying to WIMPs accounts for almost the entirety of $\mathcal{B}_{H\to\text{inv}}$ or $\Gamma^{\text{H}}_{\text{inv}}$ since the SM invisible Higgs ($H \to ZZ^* \to 4\nu$) has BR $\sim 0.1\%$ which is very small. Therefore, those models are sensitive for WIMPs which have a mass of $m_{\text{WIMP}} < m_H/2$.

A simple correlation between $\mathcal{B}_{H\to\text{inv}}$ and σ^{SI}(WIMP-N) is possible through an effective field theory (EFT) approach that assumes new physics rests at the $\mathcal{O}$(1TeV) scale, and could be modified if a renormalisable mechanism for fermionic WIMP masses is included [122, 123]. Differing spin scenarios for the WIMP (scalar and Majorana) are considered separately, as the spin impacts the Higgs boson invisible partial decay width.

The result presented here is compared to direct detection DM experiments interpreted for the Higgs-portal model outlined above, where 90% CL limit is used for direct comparison [108, 124–128]; as shown in Figure 46. These are spin-independent results obtained directly from searches for nuclei recoils from elastic scattering of WIMPs, rather than being inferred indirectly through Higgs boson exchange in the Higgs portal model [119]. The 90% CL upper limit on $\mathcal{B}_{H\to\text{inv}}$ of 0.09 is transformed to 90% CL upper limit on σ^{SI}(WIMP-N) as a function of m_{WIMP}. The hashed error bands on the Higgs Portal contributions arise from the systematic variation of the nuclear form factor which value is taken to be $f_{\text{N}} = 0.308(18)$ [112].

Beyond the scalar and Majorana fermion interpretations for WIMP candidates, various theoretical models introduce WIMPs to be a vectorial DM state. The EFT approach [104, 129] used for scalar and fermion also includes an interpretation for vector DM, which then was put aside due to some concerns about non-renormalisability and unitarity violation issue.

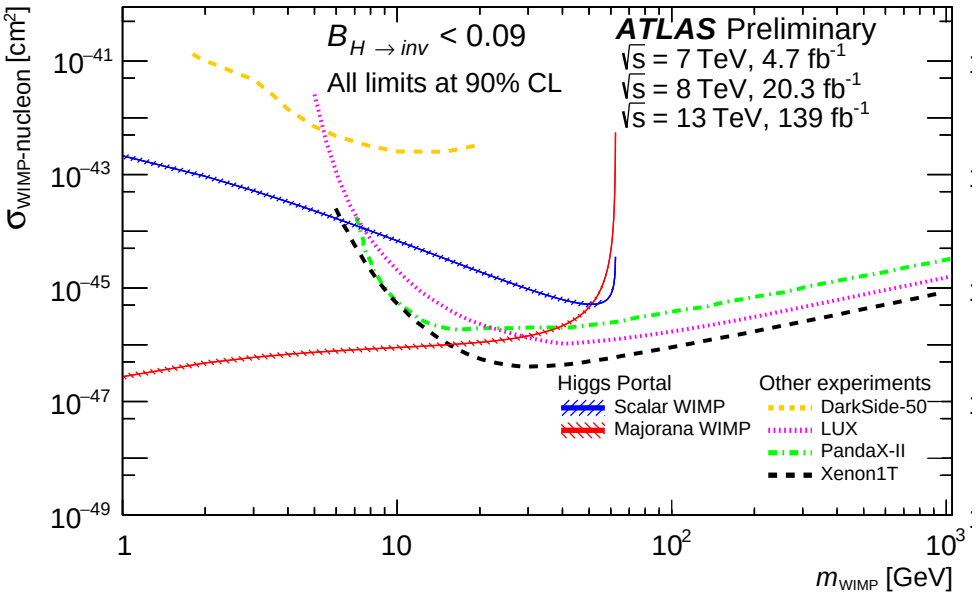

Figure 46: The combined invisible Higgs result at the 90% CL on the WIMP–nucleon scattering cross section in a Higgs portal model as a function of the mass of the dark-matter particle, shown separately for a scalar and Majorana fermion. Excluded and allowed regions from direct detection experiments at the confidence levels indicated are also shown [108, 124–126, 128].

However, this was refuted as shown in the following chapter and which is published in [119].

Chapter 7:

Higgs portal vector dark matter interpretation

At the LHC, experiments have explored Higgs portal scenarios in which the 125 GeV Higgs boson has substantial coupling with WIMP candidates (such as singlet scalar S, vector V, fermion χ) to induce interaction between WIMP and nucleon; the WIMP could be invisible decay products of the Higgs boson [103, 104, 129–140]. Therefore, limits on the branching ratio ($\mathcal{B}_{H\to\text{inv}}$) from invisible Higgs decay can be used to set upper bounds on spin-independent DM-nucleon scattering cross section σ^{SI}(WIMP-N). LHC interpretations complement direct and indirect detection results. [108, 124–126, 141, 142].

The Effective Field Theory (EFT) approach is based on a description of unknown DM-Standard Model interactions in a very economical way. This has attracted significant attention, especially because of its simplicity and flexibility, which allows it to be used in vastly different search contexts. For the scalar and Majorana fermion WIMP candidates, the EFT approach [104, 129] can be safely used. Hence, the EFT approach [104] is used in LHC Run–1 papers [143, 144]. Unfortunately, the validity of this approach for the vector-DM case has been questioned and its limitations recognized by the theoretical and experimental communities [110]. Recent efforts to develop more model-independent approaches to DM searches stimulated this study [111], where the EFT approach is shown to result from a valid ultraviolet (UV) model ; therefore, EFT is viable for vector-DM interpretations. The UV completion models have been investigated in two scenarios: along with the EFT approaches and in a separate model with additional fermions [145].

This note is organized as follows: common notations used in the analyses are presented in Section 7.1.1. EFT approaches and UV complete models are described and discussed in Sections 7.1.2, 7.1.3, 7.1.4 and 7.1.5. In Section 7.2, we discuss the cases of vector dark matter (VDM)-nucleon interactions. Dark matter in the sub-GeV mass range is presented in Section 7.3. The note is summarized in Section 7.4.

7.1 Analysis

7.1.1 Common convention

Throughout the paper, the following conventions are utilized frequently:

1. H: 125 GeV Higgs boson.
2. $v = 246$ GeV: Higgs field's vacuum expectation value.
3. $m_{\text{N}} = 0.938$ GeV: proton-nucleon mass.
4. m_{V} : vector boson mass.

5. $m_H = 125$ GeV: Higgs boson mass.
6. $\beta_V = \sqrt{1 - 4\frac{m_V^2}{m_H^2}}$
7. $\beta_{\mathrm{VH}} = \sqrt{1 - 4\frac{m_V^2}{m_H^2}}\left(1 - 4\frac{m_V^2}{m_H^2} + 12\frac{m_V^4}{m_H^4}\right)$
8. $\mu_{VN}^2 = \frac{m_V^2 m_N^2}{m_V^2 + m_N^2}$: vector DM reduced mass.
9. $\mathcal{B}_{H\to\mathrm{inv}}$: Branching ratio of $H \to$ invisible, upper limit at 90% CL of 11% is used as the result from the recently published VBF+MET analysis [4].
10. $\Gamma^{inv}(H \to VV) = \Gamma^{\mathrm{H}}_{\mathrm{inv}} = \mathcal{B}_{H\to\mathrm{inv}}\Gamma_H^{tot} = \frac{\mathcal{B}_{H\to\mathrm{inv}}}{1-\mathcal{B}_{H\to\mathrm{inv}}}\Gamma_H^{SM}$
11. $\Gamma_H^{SM} = 0.00407$ GeV: Higgs width at $m_H = 125$ GeV
12. $\hbar c = 1.97327\mathrm{e}^{-14}$ GeV $\times\, cm$
13. $f_N = 0.308(18)$: Higgs-nucleon form factor [112]

7.1.2 Effective Field Theory approach

In LHC Run–1 papers [143, 144] where $H \to$ invisible combination was done, the 90% CL upper limit on $\mathcal{B}_{H\to\mathrm{inv}}$ was converted into 90% CL upper limit on σ^{SI}(WIMP-N) with WIMP being either a scalar, a fermion or a vector boson by using the EFT approach [104]. In the scope of this note, only the VDM interpretation is discussed.

This approach suggests a model-independent Lagrangian for HVV coupling as the following (Equation 1 of Ref. [104]):

$$\mathcal{L}_V = \frac{1}{2}m_{\mathrm{V}}^2 V_\mu V^\mu + \frac{1}{4}\lambda_V (V_\mu V^\mu)^2 + \frac{\lambda_{\mathrm{hVV}}}{4} H^\dagger H V_\mu V^\mu. \tag{75}$$

The second term in Eq. 75 is for self–interaction and it is ignored; λ_V is the self interaction coupling for the vector. The Lagrangian has only two free parameters: HVV coupling λ_{hVV} and vector mass m_{V}. Using this Lagrangian, σ^{SI}(V-N) together with Higgs invisible decay width $\Gamma^{\mathrm{H}}_{\mathrm{inv}}$ are derived as functions of m_{V} and λ_{VH} as follow (Equations 4 and 5 of Ref. [104]):

$$\Gamma^{inv}(H \to VV) = \lambda_{HVV}^2 \frac{v^2 \beta_{VH} m_H^3}{512\pi m_V^4} \tag{76}$$

$$\sigma^{\mathrm{SI}}(\text{V-N})_{EFT} = \lambda_{HVV}^2 \frac{m_N^2 f_N^2}{16\pi m_H^4 (m_V + m_N)^2} \tag{77}$$

Extracting the coupling λ_{HVV} from Equation 76 and substitute into Equation 77, one can find a direct relation between σ^{SI}(V-N) and $\Gamma^{\mathrm{H}}_{\mathrm{inv}}$:

$$\lambda_{HVV}^2 = \Gamma^{inv}(H \to VV) \frac{512\pi m_V^4}{v^2 \beta_{VH} m_H^3} \tag{78}$$

$$\sigma^{\mathrm{SI}}(\text{V-N})_{EFT} = \Gamma^{inv}(H \to VV)\frac{512\pi m_V^4}{v^2\beta_{VH}m_H^3} \times \frac{m_N^2 f_N^2}{16\pi m_H^4(m_V+m_N)^2}$$

$$\sigma^{\mathrm{SI}}(\text{V-N})_{EFT} = \Gamma^{inv}(H \to VV)\frac{32 m_V^4 m_N^2 f_N^2}{v^2\beta_{VH}m_H^7(m_V+m_N)^2}$$

$$\sigma^{\mathrm{SI}}(\text{V-N})_{EFT} = 32\mu_{VN}^2\Gamma^{\mathrm{H}}_{\mathrm{inv}}\frac{m_{\mathrm{V}}^2 m_{\mathrm{N}}^2 f_{\mathrm{N}}^2}{v^2\beta_{VH}m_H^7} \tag{79}$$

Using Equation 79 one can transform the limit on $\mathcal{B}_{H\to\mathrm{inv}}$ into the vector line interpretation as in the green hashed band in Figure 9 of Ref. [143]. That figure shows the ATLAS Run–1 upper limit at the 90% CL on the WIMP–nucleon scattering cross section in a Higgs portal model as a function of the mass of the dark-matter particle, for a scalar, Majorana fermion, or vector-boson WIMP. LHC interpreted VDM limit in EFT was claimed to be model-independent and better than limits from direct detection in the regime of $m_{\mathrm{V}} < \frac{m_H}{2}$. However, it drew controversial attention, which will be discussed in Section 7.1.3.

7.1.3 Objection on EFT, first UV model

In the EFT approach used in LHC Run–1 [143], the mass of the VDM was entered arbitrarily, which leads to a non-renormalisable Lagrangian and violation of unitarity [110]. For this reason, it is safer to consider a better framework, i.e., a simple UV completion with a dark Higgs sector that gives mass to the vector DM via spontaneous electroweak symmetry breaking (EWSB). The simplest renormalisable Lagrangian for the Higgs portal VDM in such a UV model is given by Ref.[110]:

$$\mathcal{L}_{VDM} = -\frac{1}{4}V_{\mu\nu}V^{\mu\nu} + D_\mu\Phi^\dagger D^\mu\Phi - \lambda_\Phi(\Phi^\dagger\Phi - \frac{\nu_\Phi^2}{2})^2 - \lambda_{\Phi H}(\Phi^\dagger\Phi - \frac{\nu_\Phi^2}{2})(H^\dagger H - \frac{\nu_H^2}{2}), \tag{80}$$

where Φ is the dark Higgs field which generates a nonzero mass for the VDM through spontaneous $U(1)'$ breaking; $D_\mu\Phi = (\partial_u + ig_X Q_\Phi V_\mu)\Phi$ and g_X is the coupling constant.

From the Lagrangian, one can derive the invisible branching fraction of the Higgs decay [110]:

$$\Gamma^{\mathrm{H}}_{\mathrm{inv}} = \frac{g_X^2}{32\pi}\frac{m_H^3}{m_V^2}(1 - 4\frac{m_V^2}{m_H^2} + 12\frac{m_V^4}{m_H^4})(1 - 4\frac{m_V^2}{m_H^2})^{1/2}, \tag{81}$$

And then, the spin independent cross section of dark matter particles scattering, can be expressed as follows [110]:

$$\sigma^{\mathrm{SI}}(\text{V-N}) = cos^4(\theta)m_H^4 F(m_V, m_i, \nu) \times \sigma^{\mathrm{SI}}(\text{V-N})_{EFT}, \tag{82}$$

$$\simeq cos^4(\theta)(1 - \frac{m_H^2}{m_2^2}) \times \sigma^{\mathrm{SI}}(\text{V-N})_{EFT}, \tag{83}$$

Where θ is the mixing angle and m_2 is the mass of the dark Higgs boson. $\sigma^{\mathrm{SI}}(\text{V-N})_{EFT}$ is the spin independent cross section for vector DM particles from the EFT approach used in LHC Run–1 [143]. We can see that in the case of a UV completion model, the cross section has at least two additional parameters, the mass of the dark Higgs boson which is mostly singlet-like, and the mixing angle θ between the SM Higgs and the dark Higgs boson.

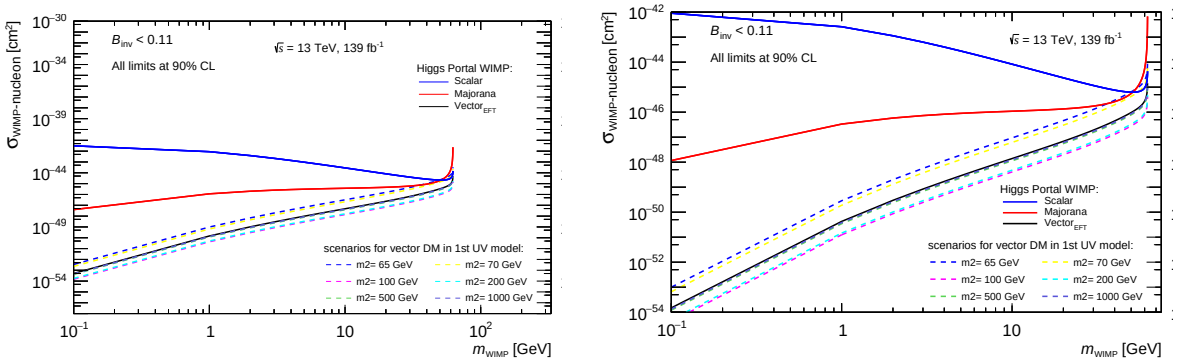

(a) (b)

Figure 47: Spin independent cross section as function of the dark matter WIMP mass, displayed for Scalar, Majorana and vector Higgs portal models using EFT approach. The vector DM state case using the first UV model is shown in Figure 47(a), for the mixing angle $\theta = 0.2$, and for the dark Higgs mass: 65, 70, 100, 200, 500, 1000 GeV for dashed lines. A zoom around the vector EFT line is shown in Figure 1b to highlight the comparison between different scenarios of dark Higgs mass and the EFT approach.

We investigated how the cross section evolves for the choice of small mixing and for different scenarios of the dark Higgs mass m_2 in the range $[65, 1000]$ GeV(see Figure 47). The resulting bound on σ^{SI}(V-N) becomes weaker than the one based on EFT if the dark Higgs mass is lighter than the SM Higgs boson ($m_2 = 65$, 70, 100 GeV), and stronger if it is heavier than the SM Higgs boson ($m_2 = 200$, 500, 1000 GeV). In addition, The UV model tends to coincide with EFT as the dark Higgs mass m_2 get larger (see Figure 47). The usual EFT approach applies only in the case of $m_2 = m_H cos(\theta)/\sqrt{1 + cos^2(\theta)}$ or $m_2 \to \infty$ and $\theta \to 0$. and therefore the bounds on the σ_p^{SI} should be taken with caution.

7.1.4 Reanalyse EFT, second UV model

In Ref.[111], theorists reanalyse the possibility that a Higgs-portal with a vectorial dark matter state could represent a consistent EFT of its UV completion. A dark Higgs sector was introduced to reproduce the vector mass via spontaneous electroweak symmetry breaking. Therefore the complete Lagrangian for dark matter phenomenology is [111]:

$$\mathcal{L} = \frac{1}{2}\tilde{g}M_V(H_2 cos(\theta) - H sin(\theta))V_\mu V^\mu + \frac{1}{8}\tilde{g}^2(H^2 sin^2(\theta) - 2HH_2 sin(\theta)cos(\theta)) + H_2^2 cos^2(\theta)V_\mu V^\mu, \quad (84)$$

where H is the 125 GeV SM-like Higgs boson, H_2 is the dark Higgs boson and $\tilde{g}$ the new gauge coupling.

From the Lagrangian, one can derive the expression for Γ_{inv} and the spin independent cross section [111].

$$(\Gamma^{\rm H}_{\rm inv})_{U(1)} = \frac{\tilde{g}^2 sin^2(\theta)}{32\pi}\frac{m_H^3}{m_V^2}\beta_{VH}, \tag{85}$$

$$\sigma^{\rm SI}(\text{V-N}) = 32cos^2(\theta)\mu^2_{VN}\frac{m_V^2}{m_H^3}\frac{BR(H\to VV)\Gamma^{tot}_H}{\beta_{VH}} \times (\frac{1}{m_2^2}-\frac{1}{m_H^2})^2\frac{m_{N^2}}{v^2}|f_N^2|, \tag{86}$$

Where β_{VH}, $BR(H\to VV)\equiv\Gamma(H\to VV)/\Gamma^{tot}_H$, μ_{V_p} are the same as in Section 7.1 and m_2 is the dark Higgs mass. The $\sigma^{\rm SI}$(V-N) is different from the formula in Ref.[111]. The scale was corrected from 8 to 32 after discussions with the authors of Ref.[111]. The prediction for VDM using EFT approach can be obtained in the limit $cos^2(\theta)m_H^4(1/m_2^2-1/m_H^2)^2\approx 1$ where $sin(\theta)<<1$ and $m_2>>m_H$.

Similarly to the first UV model, We investigated the cross section for small mixing angles and various tuning values of the dark Higgs boson m_2 in the range $[65, 1000]$ GeV(see Figure 48).

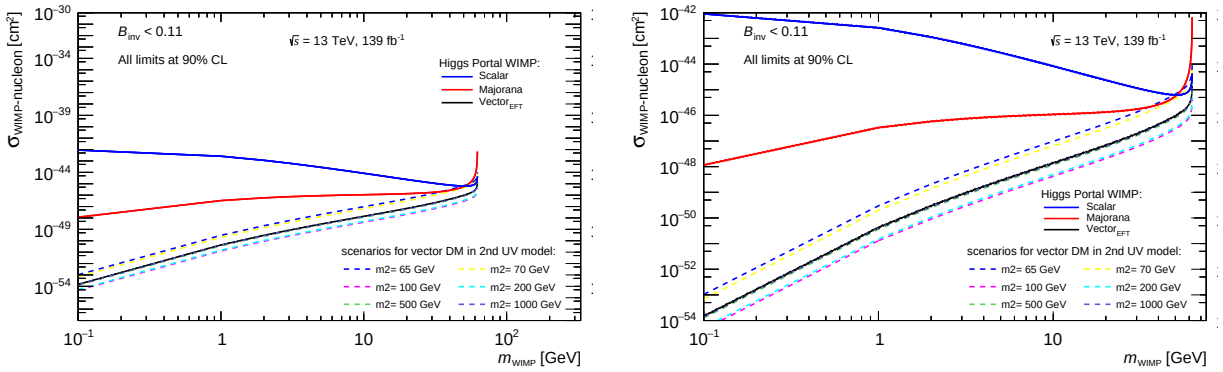

(a) (b)

Figure 48: Spin independent cross section as function of the dark matter WIMP mass, displayed for Scalar, Majorana and vector Higgs portal models using EFT approach. The vector DM state case using the second UV model is shown in Figure 47(a), for the mixing angle $\theta = 0.2$, and for the dark Higgs mass: 65, 70, 100, 200, 500, 1000 GeV for dashed lines. A zoom around the vector EFT line is shown in Figure 1b to highlight the comparison between different scenarios of dark Higgs mass and the EFT approach [146].

This exercise is extremely important not only because it shows the difference between the EFT and its UV completion according to values of (θ, m_2), but also because it demonstrates that EFT approach could be a viable limit of the renormalisable model in a large region of its parameter space.

We have checked that the models introduced in Sections 7.1.3 and 7.1.4 are equivalent and agree when the parameters are chosen consistently.

7.1.5 Radiative Higgs portal, third UV model

7.1.5.1 Lagrangian

This UV model [145] uses the same approach as introduced in other UV models mentioned in Sections 7.1.3 and 7.1.4. The vector DM is introduced as a gauge field of a $U(1)'$ group which extends the SM symmetry; a Dark Higgs sector is added in to produce the vector boson mass via the Higgs spontaneous symmetry breaking mechanism. The Lagrangian of the vector part is as the following :

$$\mathcal{L} \supset -\frac{1}{4}V_{\mu\nu}V^{\mu\nu} + (D_\mu\Phi)^\dagger(D^\mu\Phi) - V(\Phi) + \lambda_P|H|^2|\Phi|^2 \tag{87}$$

where λ_P is the mixing parameter between the SM Higgs boson and the dark Higgs mode of the field Φ (Equation 2 of Ref. [145]). This model has a distinctive feature in generating the HVV coupling, and the fermions charged under SM$\times U(1)'$ are added in, as shown below for the fermionic part of the Lagrangian :

$$\begin{aligned}\mathcal{L} \supset -m\epsilon^{ab}(\psi_{1a}\chi_{1b} + \psi_{2a}\chi_{2b}) - m_n n_1 n_2 - \; & y_\psi\epsilon^{ab}(\psi_{1a}H_b n_1 + \psi_{2a}H_b n_2) \\ & - y_\chi(\chi_1 H^* n_2 + \chi_2 H^* n_1) + h.c.\end{aligned} \tag{88}$$

where ψ, χ, n are different fermion fields, a and b are $SU(2)_W$ indices, and H is the SM 125 GeV Higgs boson (Equation 4 of Ref. [145]). Fermions lead to loop induced HVV interaction as shown in Figure 49.

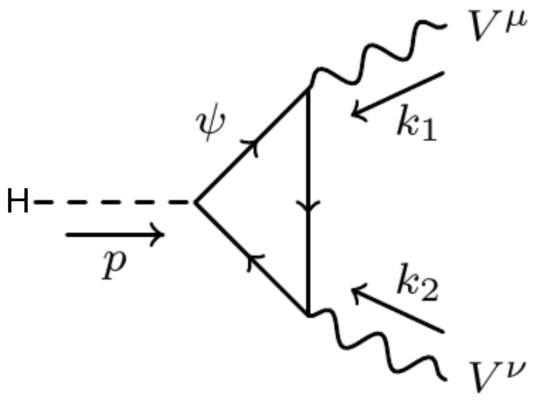

Figure 49: Fermion loop induced for HVV interaction. Figure 1 of Ref. [145].

7.1.5.2 Finding relation between $\sigma^{\mathbf{SI}}$(V-N) and $\Gamma^{\mathbf{H}}_{\mathbf{inv}}$

There are many different scenarios for this UV model; the studied scenario in this note is the simplified case where the Higgs mixing parameter $\lambda_P \ll 1$, the charged fermions and the two heavier neutral states' masses are much heavier than the lightest neutral state mass, thus decouple from the Lagrangian. The minimal parameter space to be explored includes the vector mass m_{V}, the fermion mass m_{f}, the U(1)$'$ coupling g and the Yukawa coupling y of the added fermion to the SM Higgs.

This model has no direct analytical relation between $\Gamma^{\rm H}_{\rm inv}$ and $\sigma^{\rm SI}$(V-N), and their computations are extensive. To obtain upper limit of $\sigma^{\rm SI}$(V-N) versus $m_{\rm V}$ based on the upper limit on $\mathcal{B}_{H\to\rm inv}$, one has to find values of ($m_{\rm f}$, g, y) which satisfy the $\mathcal{B}_{H\to\rm inv}$ upper limit within a certain precision, then calculate $\sigma^{\rm SI}$(V-N). In our calculation, the $\mathcal{B}_{H\to\rm inv}$ limit used is 11% at 90% CL from the recently published LHC analysis [4].

Explicitly, the task requires a scan through the set ($m_{\rm f}$, g, y) for each $m_{\rm V}$ point to find values of $\Gamma^{\rm H}_{\rm inv}$ corresponding to $\mathcal{B}_{H\to\rm inv}$ of 11% [4] within a relative precision of 0.1-1.0%. The choice of 0.1-1.0% precision is arbitrary; they are shown to have negligible impact on the results. Therefore, the more stringent precision of 0.1% was considered. Some parts of the phase space can be left out of the scan since there are other constraints on those parameters:

- $m_{\rm V} < \frac{m_H}{2}$, as for V being on-shell decay products of the Higgs boson.
- $m_{\rm f} > \frac{m_H}{2}$, to forbid the SM Higgs to decay to the additional fermions.
- $0 < g, y < 4\pi$, as rule of thumb for dimensionless couplings satisfying perturbation.
- $0 < g^2 y < 40$, a model constraint [145].

All ($m_{\rm f}$, g, y) sets that satisfy the corresponding 11% of the $\mathcal{B}_{H\to\rm inv}$ are used to construct a band of $\sigma^{\rm SI}$(V-N) versus $m_{\rm V}$. Different coarse to fine scanning steps of 0.1 to 0.01 on (g, y) are performed while keeping the same step of 1 GeV for $m_{\rm V}$ and 5 GeV for $m_{\rm f}$, as shown in Table 17.

Table 17: Scanning configurations for $m_{\rm V}$ and $m_{\rm f}$, in context of the UV model in Ref. [145]

Variable	First bin	Last bin	Step
$m_{\rm V}$ (GeV)	1	62	1
$m_{\rm f}$ (GeV)	64	499	5

Coarse scan

Scanning steps of 0.1 on (g, y) are performed while keeping the same step of 1 GeV for $m_{\rm V}$ and 5 GeV for $m_{\rm f}$ as shown in Table 17. Detailed configurations for this scan can be found in Table 18. A relative precision of 0.1% on $\Gamma^{\rm H}_{\rm inv}$ is required.

Table 18: Scanning configurations in the coarse scan for g and y in the context of UV model in Ref. [145].

Variable	First bin	Last bin	Step
g	0	12	0.1
y	0	12	0.1

Fine scan

Scanning steps of 0.01 on (g, y) are performed while keeping the same step of 1 GeV for $m_{\rm V}$ and 5 GeV for $m_{\rm f}$ as shown in Table 17. Detailed configurations for this scan can be found in Table 19. A relative precision of 1% on $\Gamma^{\rm H}_{\rm inv}$ is required.

Table 19: Scanning configurations in the fine scan for g and y in the context of the UV model in Ref. [145].

Variable	First bin	Last bin	Step
g	0	12	0.01
y	0	12	0.01

For both scans, all the found ($m_{\rm f}$, g, y) for each $m_{\rm V}$ point are used to calculate $\sigma^{\rm SI}$(V-N). The cross section values are then sorted from lowest to highest for each $m_{\rm V}$ point and plotted in Figure 50. Discussion about the plots is presented in the next section.

7.1.5.3 Results

Figures 50 and 51 show that the precision on $\Gamma^{\rm H}_{\rm inv}$ does not affect the upper bound on the $\sigma^{\rm SI}$(V-N) as the dashed lines remain the same for all cases, and stay very close to the EFT limit. However, as seen in the second and third plots of Figure 50, the fine scanning of (g, y) extends the lower bound of the green bands meaning that going finer in (g, y) one can achieve much better limits on $\sigma^{\rm SI}$(V-N) compared to EFT limit.

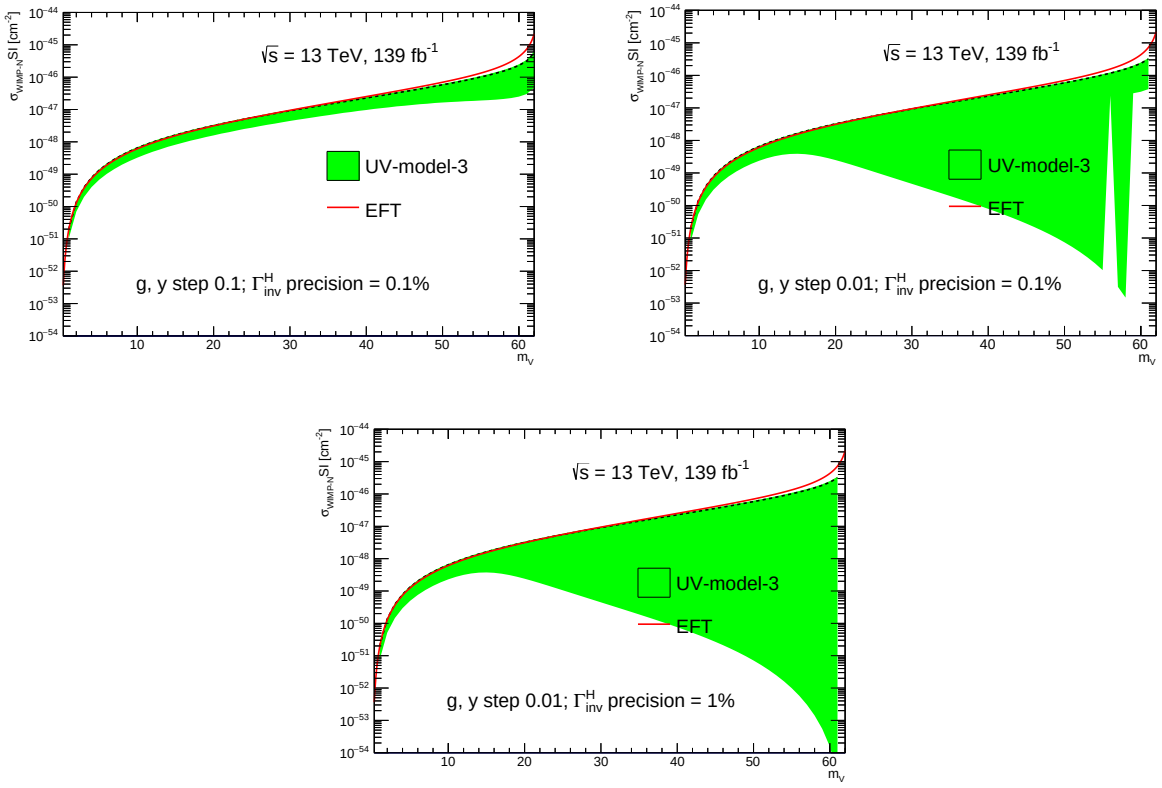

Figure 50: Green bands of upper limit on σ^{SI}(V-N) from coarse scan in Table 18 (upper left canvas), fine scan from Table 19 (upper right) and fine scan from Table 19 with looser precision of $\Gamma^{\mathrm{H}}_{\mathrm{inv}}$ (down canvas) are shown in comparison with EFT red line, for the UV model in Ref. [145].

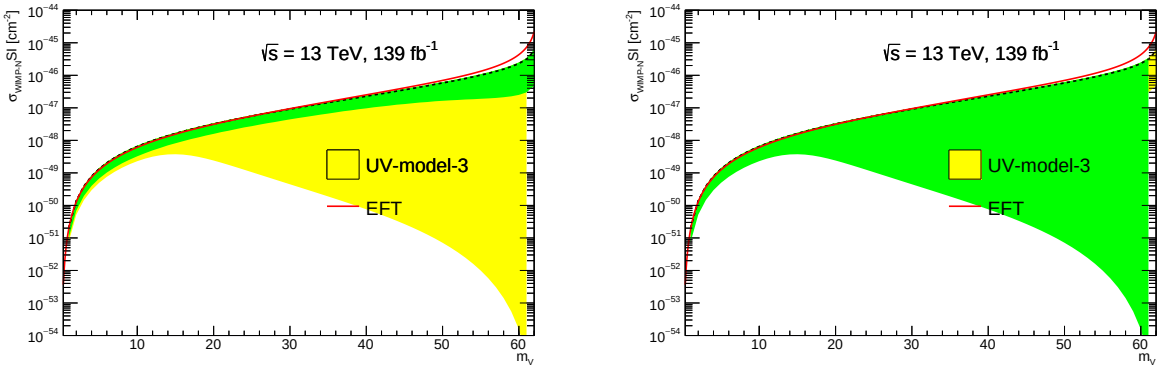

Figure 51: Superimposition of the interpretations for a coarse scan on top of a fine scan (left canvas) and vice versa (right canvas), for the UV model in Ref. [145].

7.2 Proposal

In this section, we present our proposal of the Higgs portal VDM interpretation of the spin-independent dark-matter nucleon elastic scattering cross section using the invisible Higgs decay width. We propose to re-introduce the VDM limits in the LHC Higgs portal DM interpretation plots. This proposal is motivated by the results presented in Section 7.1 and could be split in three parts.

Firstly, The limitations of EFT approach as violation of unitarity and non-renormalisable Lagrangian (claimed in Section 7.1.3) is refuted by the recent review which derived the EFT Lagrangian from a certain UV model as shown in Section 7.1.4. This shows that the EFT approach is viable in the limit of a heavy additional scalar and small mixing angle.

Secondly, we propose to show the worst and best case scenarios of the models described in Sections 2.3 and 2.4.

Thirdly, we propose to display the upper bound line of the UV-Model-3 discussed in Section 2.5, as shown with cyan in Figure 6.

Our full proposal is shown in Figure 52, where the interpretation of the radiative Higgs portal (third UV model) compared with EFT limit and with best and worst limit from the first UV model in m_2 range range of $[65, 1000]$ GeV. Also the most stringent limits currently available from direct detection experiments are shown for comparison [107, 109, 147]. The neutrino floor for coherent elastic neutrino-nucleus scattering of astrophysical neutrino is added in [148–150].

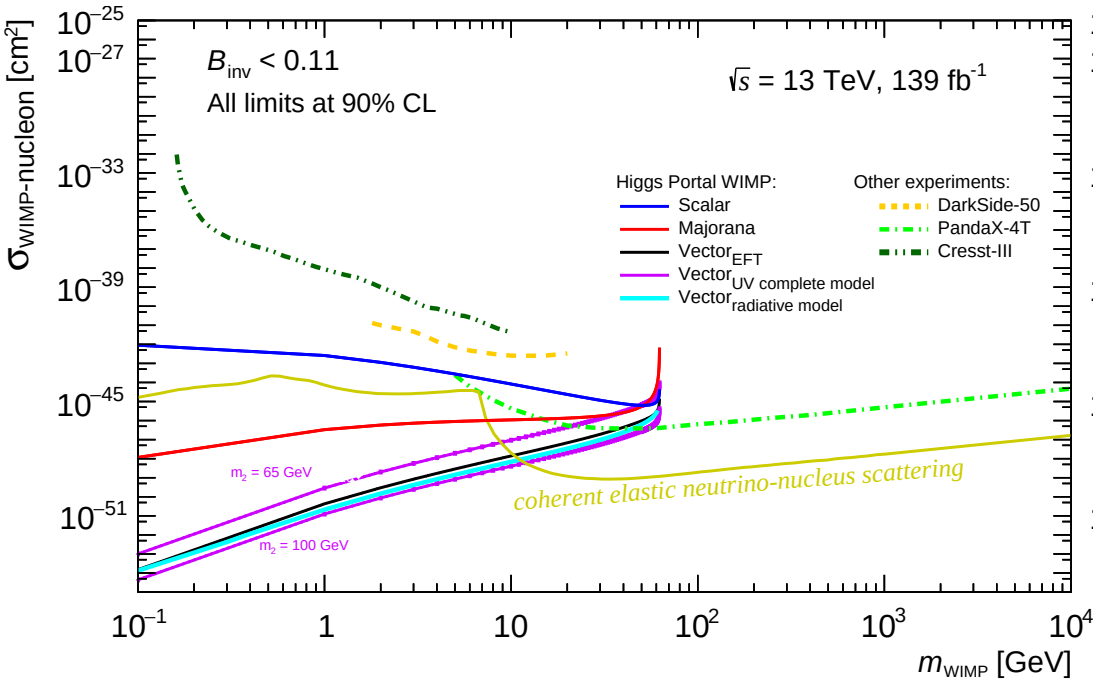

Figure 52: Upper limits on spin-independent WIMP-nucleon cross section using Higgs portal interpretations of B_{inv} at 90% CL as a function of the WIMP mass for scalar, majorana and vector states. For the vector hypothesis, the interpretation from EFT, UV complete and radiative models are presented respectively in black, magenta and cyan colours. Two scenarios are displayed for the UV complete model corresponding to the best and worst limits giving the mass of the dark Higgs in the range [65,1000] GeV. Results from direct detection experiments and the neutrino floor for coherent elastic neutrino-nucleus scattering are added for comparison [107, 109, 147, 150].

7.3 Sub-GeV WIMP mass

The LHC Higgs-portal DM interpretation of σ^{SI}(WIMP-N) has been so far shown for m_{V} ranging from 1 GeV to $\frac{m_H}{2}$. The upper edge at $\frac{m_H}{2}$ is for WIMP candidates to be produced on-shell from a Higgs decay. Whereas the lower edge at 1 GeV is arbitrarily coming from different considerations.

The first consideration is about the theoretical or cosmological constraint on the WIMP mass. However, Particle Data Group 2019 review on DM shows the possibility of going to sub-GeV regime in many BSM models with WIMP paradigm [151]. Sections 26.6.2 and 26.6.3 of the PDG review discussed solid-state cryogenic detector experiment such as CRESST-III [107] which probes DM mass down to $\sim$ 160 MeV.

LHC Dark Matter Working Group (LHCDMWG) white paper [152] has recommendations for interpretation of simplified DM models which have s-channel spin-1 mediators decaying to fermions (invisible, aka DM candidates). To predict the relic density, the LHCDMWG recommends to work under the assumption that the DM annihilation cross section of the predicted models is fully responsible for the DM number density [152]. That leads to Figures 3 and 4 of Ref. [152] to have DM mass lower bound at few GeV. However, the mentioned benchmark models do not include Higgs portal scenario in which the scalar Higgs boson is the mediator.

The second consideration is about the uncertainty on the σ^{SI}(WIMP-N) calculation via a Higgs mediator for LHC interpretation in the WIMP sub-GeV mass regime. That calculation depends on the coupling of the Higgs boson to a single nucleon, first calculated in Ref. [153] and further improved in Ref. [112] whose f_{N} value of 0.308(18) is then used in Refs. [4, 93]. These calculations use lattice QCD formalisms which are valid continuously from negative momentum transfer to positive momentum transfer, thus valid for 0-momentum transfer (our case of WIMP-nucleon elastic scattering). Interactions with the main author of Ref. [112] resolves the consideration about f_{N} vs sub-GeVmass.

In conclusion, the aforementioned considerations are not relevant to limit the LHC Higgs portal interpretations above 1 GeV. Therefore, we propose to show in the LHC Higgs portal interpretation plot, WIMP masses down to 0.1 GeV—as shown in Figure 2 of Ref. [111].

7.4 Conclusion

Several approaches for the interpretation of σ^{SI}(V-N) in Higgs-portal DM scenarios are presented. EFT approach is reviewed and shown to be safe to be reinserted in the LHC Higgs portal interpretation plot. Three UV models are studied, their results all are shown in different parameter phase spaces. In the first two UV models [110, 111], EFT is recovered when getting limits in certain region of their parameter phase spaces. Whereas for the third UV model [145], the result in a simplified regime is better than the EFT approach limits. Therefore, our final proposal for the LHC Higgs portal interpretation plot is to reinsert the EFT VDM line, include the upper bound of the third UV model, and the worst-best lines of the first and second UV models. Additionally, WIMP masses in the sub-GeV regime are discussed and proposed to be extended to 0.1 GeV in the LHC Higgs portal interpretation plot.

Conclusion

The Standard Model of particle physics is a highly successful theory explaining most of the phenomena observed in nature. Nevertheless, it does not provide a hint for dark matter candidates. A variety of complementary measurements targets this question, amongst others the collider-based search program at the LHC, which addresses the search for a dark matter candidate. Dark matter can arise from the decay of the Higgs boson and manifest itself as missing energy in the final state, which is 'invisible' for the ATLAS detector. The analysis targets Higgs bosons produced in the vector boson fusion (VBF) mode, which allows for effective background rejection and therefore for a high BSM signal sensitivity. Hence, searching for invisibly decaying Higgs bosons is a powerful method to probe for dark matter. The event is thus tagged by requiring additional physical objects in the final state, such as a VBF-jet pair.

In this thesis, a search for invisibly decaying Higgs bosons produced in the VBF mode using the full run–2 datasets is described. The samples used correspond to a luminosity of 139 fb^{-1} collected with the ATLAS experiment at a center-of-mass energy of $\sqrt{s} = 13$ TeV at the LHC. The search is motivated by Higgs portal models which describe a coupling of dark matter particles, mostly assumed in the form of WIMPs, to the Higgs boson. The VBF mode has the second highest production cross section, but is the most sensitive channel for invisibly decaying Higgs boson searches. The observed upper limit is interpreted with Higgs portal models in terms of the WIMP-nucleon scattering cross section allowing for a comparison with direct detection experiments, which are complementary to this collider search in terms of the sensitivity as a function of the WIMP mass. This shows that for Higgs portal models, where the dark matter candidates are expected with masses $< m_H/2$, the LHC with the ATLAS and CMS detectors is at present one of the most sensitive dark matter detection experiments. Furthermore, upper limits on potential heavier or lighter mediators than the SM Higgs boson are set as a function of the mediator mass.

Combination of searches performed in other Higgs boson production channels is also presented. As a result, the combination of the full run–1 and run–2 data set results yields to an upper limit on the $\mathcal{B}_{H\to\text{inv}}$ of $0.09^{+0.04}_{-0.11}$ at 90% CL. The obtained combination is also translated into upper limits on the Spin-Independent WIMP-nucleon scattering cross section using Higgs portal models.

Finally, interpretations of invisibly decaying Higgs boson searches as limits on several BSM models, which include dark matter, were also shown, where several framework scenarios for the interpretation of σ^{SI}(V-N) in Higgs-portal DM are presented. This includes the review of the Effective Field Theory (FET) framework as well as three of the ultraviolet (UV) complete models. In addition, the results are explored in different parameter of the phase spaces, where in the first two UV models [110, 111], the EFT results is re-produced when the limits are considered in certain region of their parameter phase spaces. Whereas, for the third UV complete model [145], the result in a simplified regime is better than the limits

obtained based on the EFT approach. As a result, a proposal to include interpretation for vector DM in the EFT and UV completions theoretical framework is presented. Further, from the perspective of the resulting studies, an extension of the LHC DM interpretations to the sub-GeV regime is suggested as well.

Although numerous searches, including direct and indirect, dark matter still remains undetected through non-gravitational interactions. Missing energy searches are among the most interesting to probe the existence of dark matter in light of the next LHC upgrades, where many of the existing physics analyses have to be re-thought to exploit the potential of the LHC to the maximum. Moreover, these analyses typically cover complementary phase-space to the direct detection experiments. However, searches for invisibly decaying Higgs bosons are heavily driven by the selections at the trigger level and are particularly challenging, requiring the use of cutting-edge techniques to fully exploit the LHC data. Despite that for the moment the analysis does not benefit from the application of machine learning techniques, since the presented cut-based analysis seems to be well optimised for the given background modelling and analysis strategy, but the situation may be different in the future and must be evaluated again. Designing and implementing ad-hoc optimised machine learning techniques at the trigger level of ATLAS could minimise the thresholds, allowing the system to be more inclusive and flexible when triggering events. Lowered thresholds would also improve background modelling and all additional 'shape' information to be used. As a consequence, the missing energy searches would be the first to benefit from this approach, since an accurate modelling of the background is a key aspect to gain sensitivity. For the interpretation of the result under the scenario of presence of other massive mediators, the corresponding sensitivity ca be improved by optimizing event selection and revising the binning strategy for heavier mediators masses.

References

[1] M. Zaazoua, L. Truong, K. A. Assamagan, and F. Fassi, *Higgs portal vector dark matter interpretation: review of Effective Field Theory approach and ultraviolet complete models*, (2021), arXiv: 2107.01252 [hep-ph] (cit. on pp. vii, 85, 87).

[2] ATLAS Collaboration, *Search for invisible Higgs-boson decays in events with vector-boson fusion signatures using 139 fb^{-1} of proton-proton data recorded by the ATLAS experiment*, 2022, URL: https://arxiv.org/abs/2202.07953 (cit. on pp. vii, 61, 63, 66–70, 73, 75, 80, 85–88).

[3] *Search for new phenomena in events with two opposite-charge leptons, jets and missing transverse momentum in pp collisions at $\sqrt{s} = 13$ TeV with the ATLAS detector*, tech. rep., CERN, 2020, URL: https://cds.cern.ch/record/2728056 (cit. on pp. vii, 89–91).

[4] *Search for invisible Higgs boson decays with vector boson fusion signatures with the ATLAS detector using an integrated luminosity of 139 fb^{-1}*, tech. rep. ATLAS-CONF-2020-008, CERN, 2020, URL: http://cds.cern.ch/record/2715447 (cit. on pp. vii, 61, 89, 91, 95, 100, 106).

[5] M. e. a. Aaboud, *Search for invisible Higgs boson decays in vector boson fusion at s=13TeV with the ATLAS detector*, Physics Letters B **793** (2019) 499, ISSN: 0370-2693, URL: http://dx.doi.org/10.1016/j.physletb.2019.04.024 (cit. on pp. 1, 61, 70, 84).

[6] *Dirac, Majorana and Weyl fermions*, (), URL: https://arxiv.org/pdf/1006.1718.pdf (cit. on pp. 5, 6, 8).

[7] *LAGRANGIAN FORMULATION OF THE ELECTROMAGNETIC FIELD*, (), URL: https://math.uchicago.edu/~may/REU2012/REUPapers/Yu.pdf (cit. on p. 6).

[8] *THE STANDARD MODEL OF ELECTROWEAK INTERACTIONS*, (), URL: https://arxiv.org/pdf/hep-ph/0502010.pdf (cit. on pp. 6, 7).

[9] *A construction of the Glashow-Weinberg-Salam model on the lattice with exact gauge invariance*, (), URL: https://arxiv.org/abs/0709.3658 (cit. on p. 8).

[10] *THE STANDARD MODEL OF ELECTROWEAK INTERACTIONS*, (), URL: https://arxiv.org/pdf/hep-ph/0502010.pdf (cit. on pp. 8, 9, 12).

[11] *Does the Higgs Mechanism Exist?*, (), URL: https://arxiv.org/pdf/0806.1359.pdf (cit. on p. 10).

[12] *Gauge invariant accounts of the Higgs mechanism*, (), URL: https://arxiv.org/pdf/1102.0468.pdf (cit. on p. 10).

[13] M. E. Peskin and D. V. Schroeder, *An Introduction to quantum field theory*, Addison-Wesley, 1995, ISBN: 978-0-201-50397-5 (cit. on p. 11).

[14] G. Aad et al., *Observation of a new particle in the search for the Standard Model Higgs boson with the ATLAS detector at the LHC*, Physics Letters B **716** (2012) 1, ISSN: 0370-2693, URL: http://dx.doi.org/10.1016/j.physletb.2012.08.020 (cit. on p. 13).

[15] S. Chatrchyan and e. a. Khachatryan, *Observation of a new boson at a mass of 125 GeV with the CMS experiment at the LHC*, Physics Letters B **716** (2012) 30, ISSN: 0370-2693, URL: http://dx.doi.org/10.1016/j.physletb.2012.08.021 (cit. on p. 13).

[16] S. D. Bass, A. D. Roeck, and M. Kado, *The Higgs boson implications and prospects for future discoveries*, Nature Reviews Physics **3** (2021) 608, URL: https://doi.org/10.1038%2Fs42254-021-00341-2 (cit. on p. 13).

[17] *Dark Matter and Dark Energy: A Challenge for Modern Cosmology*, (), URL: https://ui.adsabs.harvard.edu/abs/2011ASSL..370.....M/abstract (cit. on p. 14).

[18] *The Effect of Retardation on Galactic Rotation Curves*, (), URL: https://www.researchgate.net/publication/333232727_The_Effect_of_Retardation_on_Galactic_Rotation_Curves (cit. on p. 15).

[19] *Rotation Curve of the Milky Way and the Dark Matter Density*, (), URL: https://www.mdpi.com/2075-4434/8/2/37 (cit. on p. 15).

[20] J. E. Carlstrom, G. P. Holder, and E. D. Reese, *Cosmology with the Sunyaev-Zel'dovich Effect*, Annual Review of Astronomy and Astrophysics **40** (2002) 643, eprint: https://doi.org/10.1146/annurev.astro.40.060401.093803, URL: https://doi.org/10.1146/annurev.astro.40.060401.093803 (cit. on p. 15).

[21] *Principles of Gravitational Lensing*, (), URL: https://www.springer.com/gp/book/9783030021214 (cit. on p. 16).

[22] *The dark matter of gravitational lensing*, (), URL: https://arxiv.org/abs/1001.1739 (cit. on p. 16).

[23] *Turning off the Lights: How Dark is Dark Matter?*, (), URL: https://arxiv.org/abs/1011.2907 (cit. on p. 16).

[24] *Dark Matter Self-interactions and Small Scale Structure*, (), URL: https://arxiv.org/abs/1705.02358 (cit. on p. 17).

[25] *The non-gravitational interactions of dark matter in colliding galaxy clusters*, (), URL: https://arxiv.org/abs/1503.07675 (cit. on p. 17).

[26] *Axinos as Cold Dark Matter*, (), URL: https://arxiv.org/abs/hep-ph/9905212 (cit. on p. 17).

[27] R. Holman, G. Lazarides, and Q. Shafi, *Axions and the dark matter of the Universe*, Phys. Rev. D **27** (4 1983) 995, URL: https://link.aps.org/doi/10.1103/PhysRevD.27.995 (cit. on p. 17).

[28] *Sterile Neutrinos as Dark Matter*, (), URL: https://arxiv.org/abs/hep-ph/9303287 (cit. on p. 17).

[29] S. Tremaine and J. E. Gunn, *Dynamical Role of Light Neutral Leptons in Cosmology*, Phys. Rev. Lett. **42** (6 1979) 407, URL: https://link.aps.org/doi/10.1103/PhysRevLett.42.407 (cit. on p. 17).

[30] *Cores in Dwarf Galaxies from Fermi Repulsion*, (), URL: https://arxiv.org/abs/1611.04590 (cit. on p. 17).

[31] *Strongest model-independent bound on the lifetime of Dark Matter*, (), URL: https://arxiv.org/abs/1407.2418 (cit. on p. 17).

[32] *DARK MATTER AXIONS*, (), URL: https://www.worldscientific.com/doi/abs/10.1142/S0217751X10048846 (cit. on pp. 17, 18).

[33] S. G. Dearborn DS Schramm DN, *Astrophysical constraints on the couplings of axions, majorons, and familons*, () (cit. on p. 18).

[34] G. Raffelt and D. Seckel, *Bounds on exotic-particle interactions from SN1987A*, Phys. Rev. Lett. **60** (18 1988) 1793, URL: https://link.aps.org/doi/10.1103/PhysRevLett.60.1793 (cit. on p. 18).

[35] *Dark Matter and Collider Phenomenology of Universal Extra Dimensions*, (), URL: https://arxiv.org/abs/hep-ph/0701197 (cit. on p. 18).

[36] J. L. Feng and J. Kumar, *The WIMPless Miracle: Dark-Matter Particles without Weak-Scale Masses or Weak Interactions*, Phys. Rev. Lett. **101** (2008) 231301, arXiv: 0803.4196 [hep-ph] (cit. on p. 18).

[37] E. Mobs, *The CERN accelerator complex - 2019. Complexe des accélérateurs du CERN - 2019*, (2019), General Photo, URL: https://cds.cern.ch/record/2684277 (cit. on p. 20).

[38] J. Wenninger, *Machine Protection and Operation for LHC*, (2016) (cit. on p. 21).

[39] *Pulling together: Superconducting electromagnets*, (), URL: https://home.cern/science/engineering/pulling-together-superconducting-electromagnets (cit. on p. 21).

[40] C. collaboration, *The CMS experiment at the CERN LHC. The Compact Muon Solenoid experiment*, JINST **3** (2008) S08004. 361 p, Also published by CERN Geneva in 2010, URL: https://cds.cern.ch/record/1129810 (cit. on p. 21).

[41] T. L. Collaboration, *Roadmap for selected key measurements of LHCb*, 2010, arXiv: 0912.4179 [hep-ex] (cit. on p. 21).

[42] C. Fabjan and J. Schukraft, *The story of ALICE: Building the dedicated heavy ion detector at LHC*, 2011, arXiv: 1101.1257 [physics.ins-det] (cit. on p. 21).

[43] G. Ruggiero et al., *The TOTEM Detector at LHC*, (2010), ed. by M. Deile, D. d'Enterria, and A. De Roeck (cit. on p. 22).

[44] T. L. Collaboration, **3** (2008) S08006, URL: https://doi.org/10.1088/1748-0221/3/08/s08006 (cit. on p. 22).

[45] A. Tricomi et al., *The LHCf experiment at the LHC: Physics Goals and Status*, Nuclear Physics B Proceedings Supplements **196** (2009) 30 (cit. on p. 22).

[46] J. L. Pinfold, *The MoEDAL Experiment at the LHC—A Progress Report*, Universe **5** (2019), ISSN: 2218-1997, URL: https://www.mdpi.com/2218-1997/5/2/47 (cit. on p. 22).

[47] J. W. Carter, *Luminosity measurement with the ATLAS experiment at the LHC*, tech. rep., CERN, 2020, URL: https://cds.cern.ch/record/2747042 (cit. on p. 22).

[48] W. Herr and B. Muratori, *Concept of luminosity*, (2006), URL: https://cds.cern.ch/record/941318 (cit. on p. 22).

[49] M. Giovannozzi and F. Van der Veken, *Description of the luminosity evolution for the CERN LHC including dynamic aperture effects. Part II: application to Run 1 data*, Nuclear Instruments and Methods in Physics Research Section A: Accelerators, Spectrometers, Detectors and Associated Equipment **908** (2018) 1, ISSN: 0168-9002, URL: https://www.sciencedirect.com/science/article/pii/S016890021830963X (cit. on p. 23).

[50] P. Grafström and W. Kozanecki, *Luminosity determination at proton colliders*, Progress in Particle and Nuclear Physics **81** (2015) 97, ISSN: 0146-6410, URL: https://www.sciencedirect.com/science/article/pii/S0146641014000878 (cit. on p. 23).

[51] *ATLAS: technical proposal for a general-purpose pp experiment at the Large Hadron Collider at CERN*, LHC technical proposal, CERN, 1994, URL: https://cds.cern.ch/record/290968 (cit. on pp. 26, 30).

[52] S. Murk, "Trigger Algorithms and Monte Carlo Event Generation for Dijet Searches in ATLAS and Beyond", 2017 (cit. on p. 27).

[53] *Performance of the muon spectrometer alignment in 2017 and 2018 data*, tech. rep., CERN, 2021, URL: https://cds.cern.ch/record/2753329 (cit. on p. 31).

[54] J. Pequenao, "Computer generated image of the ATLAS Muons subsystem", 2008, URL: https://cds.cern.ch/record/1095929 (cit. on p. 31).

[55] J. Montejo Berlingen, *Triggering in the ATLAS experiment*, tech. rep., CERN, 2020, URL: https://cds.cern.ch/record/2742661 (cit. on p. 32).

[56] P. Jenni, M. Nessi, M. Nordberg, and K. Smith, *ATLAS high-level trigger, data-acquisition and controls: Technical Design Report*, Technical design report. ATLAS, CERN, 2003, URL: https://cds.cern.ch/record/616089 (cit. on p. 32).

[57] A. et all, *ATLAS detector and physics performance: Technical Design Report, 1*, Technical design report. ATLAS, CERN, 1999, URL: https://cds.cern.ch/record/391176 (cit. on p. 32).

[58] T. Schörner-Sadenius, *The Trigger of the ATLAS Experiment*, URL: https://doi.org/10.1142/S0217732303011800 (cit. on p. 32).

[59] T. A. collaboration, *Operation of the ATLAS trigger system in Run 2*, Journal of Instrumentation **15** (2020) P10004, URL: https://doi.org/10.1088/1748-0221/15/10/p10004 (cit. on p. 32).

[60] T. A. collaboration, *Performance of the ATLAS trigger system in 2015*, The European Physical Journal C **77** (2017), URL: https://arxiv.org/abs/1611.09661 (cit. on p. 33).

[61] M. Aaboud et al., *Performance of the ATLAS track reconstruction algorithms in dense environments in LHC Run 2*, The European Physical Journal C **77** (2017), ISSN: 1434-6052, URL: http://dx.doi.org/10.1140/epjc/s10052-017-5225-7 (cit. on p. 35).

[62] T. Cornelissen et al., *The new ATLAS track reconstruction (NEWT)*, Journal of Physics: Conference Series **119** (2008) 032014, URL: https://doi.org/10.1088/1742-6596/119/3/032014 (cit. on pp. 35, 38).

[63] G. Borissov et al., *ATLAS strategy for primary vertex reconstruction during Run-2 of the LHC*, tech. rep., CERN, 2015, URL: https://cds.cern.ch/record/2015220 (cit. on p. 36).

[64] W. Lampl et al., *Calorimeter Clustering Algorithms: Description and Performance*, tech. rep., CERN, 2008, URL: https://cds.cern.ch/record/1099735 (cit. on pp. 36, 41).

[65] M. Aaboud et al., *Electron reconstruction and identification in the ATLAS experiment using the 2015 and 2016 LHC proton–proton collision data at*

$$\sqrt{s} = 13$$

$$TeV$$

, The European Physical Journal C **79** (2019), ISSN: 1434-6052, URL: http://dx.doi.org/10.1140/epjc/s10052-019-7140-6 (cit. on p. 37).

[66] G. Aad et al., *Electron and photon energy calibration with the ATLAS detector using LHC Run 1 data*, The European Physical Journal C **74** (2014), ISSN: 1434-6052, URL: http://dx.doi.org/10.1140/epjc/s10052-014-3071-4 (cit. on p. 38).

[67] G. Aad et al., *Electron and photon performance measurements with the ATLAS detector using the 2015–2017 LHC proton-proton collision data*, Journal of Instrumentation **14** (2019) P12006, ISSN: 1748-0221, URL: http://dx.doi.org/10.1088/1748-0221/14/12/P12006 (cit. on p. 39).

[68] M. Aaboud et al., *Electron and photon energy calibration with the ATLAS detector using 2015–2016 LHC proton-proton collision data*, Journal of Instrumentation **14** (2019) P03017, ISSN: 1748-0221, URL: http://dx.doi.org/10.1088/1748-0221/14/03/P03017 (cit. on p. 39).

[69] S. Rettie, *Muon identification and performance in the ATLAS experiment*, tech. rep., CERN, 2018, URL: https://cds.cern.ch/record/2626330 (cit. on p. 40).

[70] G. A. ATLAS Collaboration and et al., *Muon reconstruction and identification efficiency in ATLAS using the full Run 2 pp collision data set at $\sqrt{s}$=13 TeV*, (2021), URL: https://arxiv.org/abs/2012.00578 (cit. on p. 39).

[71] M. Cacciari, G. P. Salam, and G. Soyez, *The catchment area of jets*, Journal of High Energy Physics **2008** (2008) 005, URL: https://arxiv.org/abs/0802.1188 (cit. on p. 41).

[72] A. collaboration, *Topological cell clustering in the ATLAS calorimeters and its performance in LHC Run 1*, The European Physical Journal C **77** (2017), URL: https://arxiv.org/abs/1603.02934 (cit. on p. 41).

[73] A. collaboration, *Jet reconstruction and performance using particle flow with the ATLAS Detector*, The European Physical Journal C **77** (2017), URL: https://doi.org/10.1140/epjc/s10052-017-5031-2 (cit. on p. 41).

[74] ATLAS Collaboration, *Jet energy scale and resolution measured in proton-proton collisions at $\sqrt{s} = 13$ TeV with the ATLAS detector*, (2020), URL: https://arxiv.org/abs/2007.02645 (cit. on p. 41).

[75] A. Collaboration, *ATLAS b-jet identification performance and efficiency measurement with $t\bar{t}$ events in p-p collisions at $\sqrt{s} = 13$ TeV*, The European Physical Journal C **79** (2019), URL: https://arxiv.org/abs/1907.05120 (cit. on p. 41).

[76] *Tagging and suppression of pileup jets with the ATLAS detector*, tech. rep., CERN, 2014, URL: http://cds.cern.ch/record/1700870 (cit. on pp. 41–43).

[77] *Forward Jet Vertex Tagging: A new technique for the identification and rejection of forward pileup jets*, tech. rep., CERN, 2015, URL: https://cds.cern.ch/record/2042098 (cit. on pp. 41, 46).

[78] S. Lai and A. Kaczmarska, *Reconstruction and Identification of Hadronic Tau Decays with ATLAS*, 2008, arXiv: 0809.5144 [hep-ex] (cit. on p. 43).

[79] *Measurement of the tau lepton reconstruction and identification performance in the ATLAS experiment using pp collisions at $\sqrt{s} = 13$ TeV*, tech. rep., CERN, 2017, URL: https://cds.cern.ch/record/2261772 (cit. on p. 43).

[80] M. Aaboud et al., *Performance of missing transverse momentum reconstruction with the ATLAS detector using proton-proton collisions at $\sqrt{s} = 13$ TeV*, Eur. Phys. J. C **78** (2018) 903, arXiv: 1802.08168 [hep-ex] (cit. on pp. 44, 48–50).

[81] G. Aad et al., *Performance of missing transverse momentum reconstruction in proton-proton collisions at $\sqrt{s} = 7$ TeV with ATLAS*, The European Physical Journal C **72** (2012), ISSN: 1434-6052, URL: http://dx.doi.org/10.1140/epjc/s10052-011-1844-6 (cit. on p. 45).

[82] G. Aad et al., *Performance of algorithms that reconstruct missing transverse momentum in*

$$\sqrt{s}$$

s = 8 TeV proton–proton collisions in the ATLAS detector, The European Physical Journal C **77** (2017), ISSN: 1434-6052, URL: http://dx.doi.org/10.1140/epjc/s10052-017-4780-2 (cit. on p. 45).

[83] *E_T^{miss} performance in the ATLAS detector using 2015-2016 LHC p-p collisions*, tech. rep., CERN, 2018, URL: http://cds.cern.ch/record/2625233 (cit. on pp. 45–48, 51, 52).

[84] M. Cacciari, G. P. Salam, and G. Soyez, *The catchment area of jets*, Journal of High Energy Physics **2008** (2008) 005, ISSN: 1029-8479, URL: http://dx.doi.org/10.1088/1126-6708/2008/04/005 (cit. on p. 45).

[85] G. Aad et al., *Electron and photon energy calibration with the ATLAS detector using LHC Run 1 data*, Eur. Phys. J. C **74** (2014) 3071, arXiv: 1407.5063 [hep-ex] (cit. on p. 48).

[86] *Electron efficiency measurements with the ATLAS detector using the 2015 LHC proton-proton collision data*, (2016), ed. by E. Augé, J. Dumarchez, and J. Tran Thanh Van (cit. on p. 48).

[87] A. collaboration, *Measurement of the photon identification efficiencies with the ATLAS detector using LHC Run-1 data*, The European Physical Journal C **76** (2016), URL: https://link.springer.com/article/10.1140/epjc/s10052-016-4507-9#citeas (cit. on p. 48).

[88] A. collaboration, *Electron and photon energy calibration with the ATLAS detector using LHC Run 1 data*, The European Physical Journal C **74** (2014), URL: https://link.springer.com/article/10.1140/epjc/s10052-014-3071-4 (cit. on p. 48).

[89] G. Aad et al., *Identification and energy calibration of hadronically decaying tau leptons with the ATLAS experiment in pp collisions at $\sqrt{s}$=8 TeV*, Eur. Phys. J. C **75** (2015) 303, arXiv: 1412.7086 [hep-ex] (cit. on p. 48).

[90] B. Efron, *Bayesian inference and the parametric bootstrap*, The Annals of Applied Statistics **6** (2012), ISSN: 1932-6157, URL: http://dx.doi.org/10.1214/12-AOAS571 (cit. on p. 57).

[91] S. Dittmaier et al., *Handbook of LHC Higgs Cross Sections: 1. Inclusive Observables*, CERN Yellow Reports: Monographs, CERN, 2011, URL: http://cds.cern.ch/record/1318996 (cit. on p. 61).

[92] S. Dittmaier et al., *Handbook of LHC Higgs Cross Sections: 2. Differential Distributions*, CERN Yellow Reports: Monographs, CERN, 2012, URL: http://cds.cern.ch/record/1416519 (cit. on p. 61).

[93] ATLAS Collaboration, *Combination of searches for invisible Higgs boson decays with the ATLAS experiment*, Phys. Rev. Lett. **122** (2019) 231801, arXiv: 1904.05105 [hep-ex] (cit. on pp. 61, 106).

[94] A. Sirunyan and T. et al., *Search for invisible decays of a Higgs boson produced through vector boson fusion in proton-proton collisions at s=13TeV*, Physics Letters B **793** (2019) 520, ISSN: 0370-2693, URL: http://dx.doi.org/10.1016/j.physletb.2019.04.025 (cit. on p. 61).

[95] J. M. Lindert, S. Pozzorini, and M. Schönherr, *Precise predictions for V+2 jet backgrounds in searches for invisible Higgs decays*, 2022, URL: https://arxiv.org/abs/2204.07652 (cit. on pp. 68, 79).

[96] G. Aad et al., *Jet energy scale and resolution measured in proton–proton collisions at $\sqrt{s}$ = 13 TeV with the ATLAS detector*, Eur. Phys. J. C **81** (2021) 689, arXiv: 2007.02645 [hep-ex] (cit. on p. 73).

[97] CERN, *CERN Yellow Reports: Monographs, Vol 2 (2017): Handbook of LHC Higgs cross sections: 4. Deciphering the nature of the Higgs sector*, en, 2017, URL: https://e-publishing.cern.ch/index.php/CYRM/issue/view/32 (cit. on p. 79).

[98] I. W. Stewart and F. J. Tackmann, *Theory uncertainties for Higgs mass and other searches using jet bins*, Physical Review D **85** (2012), URL: https://arxiv.org/abs/1107.2117 (cit. on pp. 79, 80).

[99] *Luminosity determination in pp collisions at $\sqrt{s} = 13$ TeV using the ATLAS detector at the LHC*, tech. rep., CERN, 2019, URL: https://cds.cern.ch/record/2677054 (cit. on p. 82).

[100] T. Junk, *Confidence level computation for combining searches with small statistics*, Nuclear Instruments and Methods in Physics Research Section A: Accelerators, Spectrometers, Detectors and Associated Equipment **434** (1999) 435, URL: https://arxiv.org/abs/hep-ex/9902006 (cit. on p. 84).

[101] A. L. Read, *Presentation of search results: the CLs technique*, Journal of Physics G: Nuclear and Particle Physics **28** (2002) 2693, URL: https://doi.org/10.1088/0954-3899/28/10/313 (cit. on p. 84).

[102] G. Cowan, K. Cranmer, E. Gross, and O. Vitells, *Asymptotic formulae for likelihood-based tests of new physics*, The European Physical Journal C **71** (2011), URL: https://arxiv.org/abs/1007.1727 (cit. on p. 84).

[103] S. Kanemura, S. Matsumoto, T. Nabeshima, and N. Okada, *Can WIMP Dark Matter overcome the Nightmare Scenario?*, Phys. Rev. **D82** (2010) 055026, arXiv: 1005.5651 [hep-ph] (cit. on pp. 84, 92, 94).

[104] A. Djouadi, O. Lebedev, Y. Mambrini, and J. Quevillon, *Implications of LHC searches for Higgs–portal dark matter*, Phys. Lett. B **709** (2012) 65, arXiv: 1112.3299 [hep-ph] (cit. on pp. 84, 85, 92, 94, 95).

[105] P. J. Fox, R. Harnik, J. Kopp, and Y. Tsai, *Missing energy signatures of dark matter at the LHC*, Physical Review D **85** (2012), URL: https://arxiv.org/abs/1109.4398 (cit. on p. 84).

[106] A. D. Simone, G. F. Giudice, and A. Strumia, *Benchmarks for dark matter searches at the LHC*, Journal of High Energy Physics **2014** (2014), URL: https://arxiv.org/abs/1402.6287 (cit. on p. 84).

[107] A. Abdelhameed et al., *First results from the CRESST-III low-mass dark matter program*, Phys. Rev. D **100** (2019) 102002, arXiv: 1904.00498 [astro-ph.CO] (cit. on pp. 84, 87, 104–106).

[108] P. Agnes et al., *Low-Mass Dark Matter Search with the DarkSide-50 Experiment*, Phys. Rev. Lett. **121** (2018) 081307, arXiv: 1802.06994 [astro-ph.HE] (cit. on pp. 84, 87, 92–94).

[109] Y. M. et all, *Dark Matter Search Results from the PandaX-4T Commissioning Run*, 2021, arXiv: 2107.13438 [hep-ex] (cit. on pp. 84, 87, 104, 105).

[110] S. Baek, P. Ko, and W.-I. Park, *Invisible Higgs decay width vs. dark matter direct detection cross section in Higgs portal dark matter models*, Physics Letters B (2014), ISSN: 0370-2693, URL: http://www.sciencedirect.com/science/article/pii/S0370269314006984 (cit. on pp. 85, 94, 96, 106, 107).

[111] G. Arcadi, A. Djouadi, and M. Kado, *The Higgs-portal for vector Dark Matter and the Effective Field Theory approach: a reappraisal*, Phys. Lett. B **805** (2020) 135427, arXiv: 2001.10750 [hep-ph] (cit. on pp. 85, 94, 97, 98, 106, 107).

[112] M. Hoferichter, P. Klos, J. Menéndez, and A. Schwenk, *Improved limits for Higgs-portal dark matter from LHC searches*, Phys. Rev. Lett. **119** (2017) 181803, arXiv: 1708.02245 [hep-ph] (cit. on pp. 85, 92, 95, 106).

[113] J. Billard, E. Figueroa-Feliciano, and L. Strigari, *Implication of neutrino backgrounds on the reach of next generation dark matter direct detection experiments*, Physical Review D **89** (2014), URL: https://arxiv.org/abs/1307.5458 (cit. on p. 87).

[114] F. Ruppin, J. Billard, E. Figueroa-Feliciano, and L. Strigari, *Complementarity of dark matter detectors in light of the neutrino background*, Physical Review D **90** (2014), URL: https://arxiv.org/abs/1408.3581 (cit. on p. 87).

[115] A. collaboration, *Constraints on new phenomena via Higgs boson couplings and invisible decays with the ATLAS detector*, Journal of High Energy Physics **2015** (2015), URL: https://doi.org/10.1007%2Fjhep11%282015%29206 (cit. on pp. 89–91).

[116] ATLAS, *Search for a scalar partner of the top quark in the all-hadronic $t\bar{t}$ plus missing transverse momentum final state at $\sqrt{s}$=13 TeV with the ATLAS detector*, Eur. Phys. J. C **80** (2020) 737. 44 p, arXiv: 2004.14060, URL: https://cds.cern.ch/record/2716368 (cit. on pp. 89–91).

[117] W. Verkerke and D. Kirkby, *The RooFit toolkit for data modeling*, 2003, URL: https://arxiv.org/abs/physics/0306116 (cit. on p. 90).

[118] L. Moneta et al., *The RooStats Project*, 2010, URL: https://arxiv.org/abs/1009.1003 (cit. on p. 90).

[119] *Combination of searches for invisible Higgs boson decays with the ATLAS experiment*, (2020) (cit. on pp. 91–93).

[120] P. J. Fox, R. Harnik, J. Kopp, and Y. Tsai, *Missing energy signatures of dark matter at the LHC*, Physical Review D **85** (2012), ISSN: 1550-2368, URL: http://dx.doi.org/10.1103/PhysRevD.85.056011 (cit. on p. 92).

[121] A. De Simone, G. F. Giudice, and A. Strumia, *Benchmarks for dark matter searches at the LHC*, Journal of High Energy Physics **2014** (2014), ISSN: 1029-8479, URL: http://dx.doi.org/10.1007/JHEP06(2014)081 (cit. on p. 92).

[122] ATLAS, *Search for invisible decays of a Higgs boson using vector-boson fusion in pp collisions at $\sqrt{s} = 8$ TeV with the ATLAS detector*, Journal of High Energy Physics **2016** (2016), URL: https://doi.org/10.1007%2Fjhep01%282016%29172 (cit. on p. 92).

[123] S. Baek, P. Ko, and W.-I. Park, *Invisible Higgs decay width versus dark matter direct detection cross section in Higgs portal dark matter models*, Physical Review D **90** (2014), ISSN: 1550-2368, URL: http://dx.doi.org/10.1103/PhysRevD.90.055014 (cit. on p. 92).

[124] D. S. Akerib et al., *Results from a search for dark matter in the complete LUX exposure*, Phys. Rev. Lett. **118** (2017) 021303, arXiv: 1608.07648 [astro-ph.CO] (cit. on pp. 92–94).

[125] X. Cui et al., *Dark Matter Results From 54-Ton-Day Exposure of PandaX-II Experiment*, Phys. Rev. Lett. **119** (2017) 181302, arXiv: 1708.06917 [astro-ph.CO] (cit. on pp. 92–94).

[126] E. Aprile et al., *Dark Matter Search Results from a One Ton-Year Exposure of XENON1T*, Phys. Rev. Lett. **121** (2018) 111302, arXiv: 1805.12562 [astro-ph.CO] (cit. on pp. 92–94).

[127] E. Aprile et al., *Constraining the spin-dependent WIMP-nucleon cross sections with XENON1T*, Phys. Rev. Lett. **122** (2019) 141301, arXiv: 1902.03234 [astro-ph.CO] (cit. on p. 92).

[128] R. A. et all, *Search for dark matter with a 231-day exposure of liquid argon using DEAP-3600 at SNOLAB*, Phys. Rev. D **90** (2019), ISSN: 1550-2368, URL: https://arxiv.org/abs/1902.04048 (cit. on pp. 92, 93).

[129] A. Djouadi, A. Falkowski, Y. Mambrini, and J. Quevillon, *Direct Detection of Higgs-Portal Dark Matter at the LHC*, Eur. Phys. J. **C73** (2013) 2455, arXiv: 1205.3169 [hep-ph] (cit. on pp. 92, 94).

[130] I. Antoniadis, M. Tuckmantel, and F. Zwirner, *Phenomenology of a leptonic goldstino and invisible Higgs boson decays*, Nucl. Phys. **B707** (2005) 215, arXiv: hep-ph/0410165 [hep-ph] (cit. on p. 94).

[131] N. Arkani-Hamed, S. Dimopoulos, G. R. Dvali, and J. March-Russell, *Neutrino masses from large extra dimensions*, Phys. Rev. **D65** (2001) 024032, arXiv: hep-ph/9811448 [hep-ph] (cit. on p. 94).

[132] A. Datta, K. Huitu, J. Laamanen, and B. Mukhopadhyaya, *Invisible Higgs in theories of large extra dimensions*, Phys. Rev. **D70** (2004) 075003, arXiv: hep-ph/0404056 [hep-ph] (cit. on p. 94).

[133] R. E. Shrock and M. Suzuki, *Invisible decays of Higgs bosons*, Physics Letters B **110** (1982) 250, ISSN: 0370-2693, URL: http://www.sciencedirect.com/science/article/pii/0370269382912473 (cit. on p. 94).

[134] D. Choudhury and D. P. Roy, *Signatures of an invisibly decaying Higgs particle at LHC*, Phys. Lett. **B322** (1994) 368, arXiv: hep-ph/9312347 [hep-ph] (cit. on p. 94).

[135] O. J. P. Eboli and D. Zeppenfeld, *Observing an invisible Higgs boson*, Phys. Lett. **B495** (2000) 147, arXiv: hep-ph/0009158 [hep-ph] (cit. on p. 94).

[136] H. Davoudiasl, T. Han, and H. E. Logan, *Discovering an invisibly decaying Higgs at hadron colliders*, Phys. Rev. **D71** (2005) 115007, arXiv: hep-ph/0412269 [hep-ph] (cit. on p. 94).

[137] R. M. Godbole, M. Guchait, K. Mazumdar, S. Moretti, and D. P. Roy, *Search for 'invisible' Higgs signals at LHC via associated production with gauge bosons*, Phys. Lett. **B571** (2003) 184, arXiv: hep-ph/0304137 [hep-ph] (cit. on p. 94).

[138] D. Ghosh, R. Godbole, M. Guchait, K. Mohan, and D. Sengupta, *Looking for an Invisible Higgs Signal at the LHC*, Phys. Lett. **B725** (2013) 344, arXiv: 1211.7015 [hep-ph] (cit. on p. 94).

[139] G. Belanger, B. Dumont, U. Ellwanger, J. F. Gunion, and S. Kraml, *Status of invisible Higgs decays*, Phys. Lett. **B723** (2013) 340, arXiv: 1302.5694 [hep-ph] (cit. on p. 94).

[140] D. Curtin et al., *Exotic decays of the 125 GeV Higgs boson*, Phys. Rev. **D90** (2014) 075004, arXiv: 1312.4992 [hep-ph] (cit. on p. 94).

[141] F. Petricca et al., "First results on low-mass dark matter from the CRESST-III experiment", *15th International Conference on Topics in Astroparticle and Underground Physics (TAUP 2017) Sudbury, Ontario, Canada, July 24-28, 2017*, 2017, arXiv: 1711.07692 [astro-ph.CO] (cit. on p. 94).

[142] E. Behnke et al., *Final Results of the PICASSO Dark Matter Search Experiment*, Astropart. Phys. **90** (2017) 85, arXiv: 1611.01499 [hep-ex] (cit. on p. 94).

[143] G. Aad et al., *Constraints on new phenomena via Higgs boson couplings and invisible decays with the ATLAS detector*, JHEP **11** (2015) 206, arXiv: 1509.00672 [hep-ex] (cit. on pp. 94–97).

[144] P. Calfayan, *Searches for invisible Higgs boson decays with ATLAS and CMS*, tech. rep., CERN, 2015, URL: https://cds.cern.ch/record/2058131 (cit. on pp. 94, 95).

[145] A. DiFranzo, P. J. Fox, and T. M. P. Tait, *Vector Dark Matter through a Radiative Higgs Portal*, JHEP **04** (2016) 135, arXiv: 1512.06853 [hep-ph] (cit. on pp. 94, 99–103, 106, 107).

[146] M. Zaazoua, L. Truong, K. A. Assamagan, and F. Fassi, *Higgs portal vector dark matter interpretation: review of Effective Field Theory approach and ultraviolet complete models*, 2021, arXiv: 2107.01252 [hep-ph] (cit. on p. 98).

[147] A. et all, *Low-Mass Dark Matter Search with the DarkSide-50 Experiment*, Physical Review Letters **121** (2018), ISSN: 1079-7114, URL: http://dx.doi.org/10.1103/PhysRevLett.121.081307 (cit. on pp. 104, 105).

[148] J. Billard, E. Figueroa-Feliciano, and L. Strigari, *Implication of neutrino backgrounds on the reach of next generation dark matter direct detection experiments*, Physical Review D **89** (2014), ISSN: 1550-2368, URL: http://dx.doi.org/10.1103/PhysRevD.89.023524 (cit. on p. 104).

[149] F. Ruppin, J. Billard, E. Figueroa-Feliciano, and L. Strigari, *Complementarity of dark matter detectors in light of the neutrino background*, Physical Review D **90** (2014), ISSN: 1550-2368, URL: http://dx.doi.org/10.1103/PhysRevD.90.083510 (cit. on p. 104).

[150] J. Billard, "Searching for Dark Matter and New Physics in the Neutrino sector with Cryogenic detectors", Habilitation à diriger des recherches: Université Claude Bernard Lyon 1, 2021, URL: https://tel.archives-ouvertes.fr/tel-03259707 (cit. on pp. 104, 105).

[151] 2. PdG, *M. Tanabashi et al. (Particle Data Group), Phys. Rev. D 98, 030001 (2018) and 2019 update.*, tech. rep., 2019, URL: https://pdg.lbl.gov/2019/reviews/rpp2019-rev-dark-matter.pdf (cit. on p. 106).

[152] A. Albert et al., *Recommendations of the LHC Dark Matter Working Group: Comparing LHC searches for dark matter mediators in visible and invisible decay channels and calculations of the thermal relic density*, Physics of the Dark Universe **26** (2019) 100377, ISSN: 2212-6864, URL: http://www.sciencedirect.com/science/article/pii/S2212686419301682 (cit. on p. 106).

[153] M. Shifman, A. Vainshtein, and V. Zakharov, *Remarks on Higgs-boson interactions with nucleons*, Physics Letters B **78** (1978) 443, ISSN: 0370-2693, URL: http://www.sciencedirect.com/science/article/pii/0370269378904811 (cit. on p. 106).

Résumé

Cette thèse présente une recherche de bosons de Higgs à désintégration invisible à l'aide des données de collision proton-proton de 13 TeV enregistrées par le détecteur ATLAS au Grand collisionneur des hadrons. La recherche est effectuée à l'aide de l'ensemble de données collectées pendant la phase Run2, ce qui correspond à une luminosité totale de 139/fb. L'analyse visée est le boson de Higgs invisible produit par la fusion de bosons vectoriels, où la sensitivité est améliorée. L'estimation du bruit de fond, la sélection des événements et la fixation des limites ainsi que l'interprétation des résultats sont décrites en détail. Aucune déviation par rapport au modèle standard n'a été observée. Interprété en termes de recherche de matière noire à l'aide des modèles de bosons de Higgs, ce résultat peut être utilisé pour fixer des limites à la section efficace WIMP-nucléon diffusion. Cette thèse présente également une combinaison des études axées sur la recherche de bosons de Higgs invisibles, où le boson est produit, soit en mode VBF, soit en association avec une paire de quarks top. Ces résultats sont également interprétés dans le contexte de modèles où le boson de Higgs de 125 GeV agit comme un portail vers la matière noire. Enfin, une discussion de l'interprétation de la section efficace des nucléons et de WIMPs dans le cas du vecteur Higgs portail de la matière noire, sont mis en œuvre, où la largeur de désintégration du Higgs invisible mesurée au LHC est utilisée.

Mots- clés: *matière noir, WIMPs, Higgs, désintégration invisible, Higgs-portal, Modèle Standard*

Abstract

In this dissertation, a search for invisibly decaying Higgs bosons using 13 TeV proton-proton collision data recorded by the ATLAS detector at the LHC is presented. The search is performed using datasets collected during the Run2 phase of operation, corresponding to an integrated luminosity of 139/fb. The targeted analysis is the invisible Higgs boson produced via the Vector Boson Fusion, where the sensitivity is enhanced by allowing for new phase spaces. Background estimation, consideration of pileup tagging in the forward region, events selection categorisation, and limit setting as well as the interpretation are described in details. No deviations from the Standard Model have been observed, and the final result is reported in the form of a 95% Confidence Level upper limit on the branching fraction. The overall result of the measurement using full Run2 data yields an observed limit of 0.145. When interpreted in terms of Dark Matter searches using Higgs portal models, this result can be used to set upper limits on spin-independent WIMP-nucleon cross section. A combination of studies focusing on searches for invisible Higgs bosons, where the SM Higgs is produced, either, through VBF mode or in association with a pair of top quarks is presented in this thesis as well. Last but not least, a review and discussion of the Higgs portal-vector Dark Matter interpretation of the spin-independent Dark Matter nucleon elastic scattering cross section is implemented, where the invisible Higgs decay width measured at the LHC is used.

Key Words: *Dark Matter, WIMPs, Higgs, invisible decay, Higgs-portal, Standard Model.*